

**SUSTAINABLE ROUTES TO POROUS SILICON NANOSTRUCTURES  
AS DRUG AND GENE DELIVERY VEHICLES**

by

**JHANSI RANI KALLURI**

Bachelor of Pharmacy, 2006  
Andhra University  
Visakhapatnam, AP, India

Master of Science, 2009  
Jackson State University  
Jackson, MS, USA

Submitted to the Graduate Faculty of  
College of Science and Engineering  
Texas Christian University  
in partial fulfillment of the requirements  
for the degree of

**Doctor of Philosophy**

May 2018

**SUSTAINABLE ROUTES TO POROUS SILICON  
NANOSTRUCTURES AS DRUG AND GENE DELIVERY  
VEHICLES**

by


JHANSI RANI KALLURI

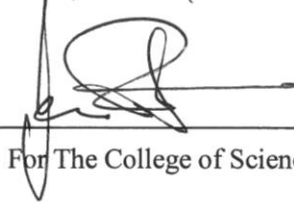
Dissertation approved:

  
Major Professor







  
For The College of Science and Engineering



## ACKNOWLEDGEMENTS

In the words of David “I will praise thee; for I am fearfully and wonderfully made: marvellous are thy works; and that my soul knoweth right well” (Psalms 139:14). With all my heart, mind and soul, I sincerely thank God for his word that kept me encouraged and motivated during the trying times.

I thank my advisor, Dr. Jeffery L. Coffey, for his constant guidance, support and help throughout my graduate research at Texas Christian University. He never failed to show his good spirit during the good and hard times. I greatly appreciate him for his invaluable time and knowledge that he shared with me. Besides my advisor, I would like to thank Dr. Phil Hartman, Dr. Onofrio Annunziata, and Dr. Kayla Green, for their valuable time and comments as members of my dissertation committee. I would also like to thank to our collaborators Dr. Leigh Canham from University of Birmingham, Dr. Giri Akkaraju, from TCU Biology for the insightful discussions. Thanks to my group members Nelli Bodiford, Anne D’Achille, Roberto Gonzalez, Nguyen Le, and Joakim Riikonen for sharing their knowledge and experience. The Robert A. Welch Foundation is gratefully acknowledged for financial support.

Finally, I thank my family for their support and encouragement. I am grateful to my brother for always been there for me as a friend. I am forever indebted to my parents for giving me the opportunities and experiences that have made me who I am. Heartfelt thanks to my husband Manik, for his unconditional love, patience and support.

## TABLE OF CONTENTS

Acknowledgments.....	iii
Table of Contents.....	iv
List of Figures.....	vii
List of Tables.....	xii
I. Literature Review .....	1
1.1. General pore classification of solids.....	2
1.2. Pore size classification of porous solids.....	3
1.3. Fabrication methods of porous silicon (pSi).....	3
1.3.1. Anodization.....	3
1.3.2. Stain Etching.....	7
1.3.3. Reducing silica to silicon reduction .....	10
1.3.3.1. General concepts.....	10
1.3.3.2. pSi derived from biogenic sources.....	10
1.3.3.3. Details of magnesiothermic reduction process.....	11
1.4. Porous silicon as a biomaterial.....	12
1.4.1. Porous silicon for drug delivery .....	14
1.4.2. Porous silicon based biosensors.....	19
1.4.3. Porous silicon in tissue engineering.....	21
1.4.4. Summary.....	23
II. Fabrication of Plant Derived Porous Silicon Powders from Silicon Accumulator Plants <i>Bambuseae</i> and <i>Equisetum telmateia</i> .....	24
2.1. Introduction .....	25
2.2. Experimental.....	26
2.2.1. Purification of Raw Ground Plant .....	26
2.2.2. Extracting silica from silicon accumulator plants .....	27
2.2.3. Magnesiothermic Reduction.....	27
2.2.4. Purification of magnesiothermic reaction products.....	27
2.2.5. Measuring oxide content.....	27
2.2.6. Silica Dissolution Assay.....	28
2.2.7. Instrumentation.....	29
2.3. Results and Discussion .....	30
2.3.1. Fabrication Method.....	30
2.3.2. Characterization of pSi Powders.....	31
2.3.3. <i>In Vitro</i> Dissolution Studies of pSi Powders .....	38
2.4. Summary .....	41

III.	Loading and Release of <i>Bambuseae Arundinacea</i> Leaf Extract (Antibacterial) from Tabasheer derived pSi.....	42
3.1.	Introduction.....	43
3.2.	Experimental .....	44
3.2.1.	Collection of plant material .....	44
3.2.2.	Soxhlet extraction.....	44
3.2.3.	Extraction at room temperature.....	44
3.2.4.	Evaluation of antibacterial activity of the leaf extracts.....	45
3.2.4.1.	Test microorganisms.....	45
3.2.4.2.	Disc diffusion assay.....	45
3.2.4.3.	Micro broth dilution assay.....	45
3.2.5.	Loading of antibacterial leaf extracts into pSi.....	46
3.2.6.	Release of antibacterial agents from pSi loaded with crude extract.....	46
3.2.7.	Isolation of known antibacterial compounds.....	46
3.2.8.	Instrumentation.....	48
3.3.	Results and Discussion.....	48
3.3.1.	Antibacterial activity of the extract.....	48
3.3.2.	Loading and release of antibacterial leaf extract from pSi particles.....	49
3.3.3.	Isolation of known antibacterials from <i>Bambuseae arundinacea</i> .....	51
3.4.	Summary .....	59
IV.	Vitamin D3 (Cholecalciferol) Loading and Release from Tabasheer Derived Porous Silicon Powders.....	60
4.1.	Introduction.....	61
4.2.	Experimental.....	63
4.2.1.	Loading Vitamin D3 (VD).....	63
4.2.1.1.	Melt loading.....	63
4.2.2.	Preparation of vitamin D3 standard curve.....	64
4.2.3.	Measuring encapsulation efficiencies (EE).....	64
4.2.4.	<i>In vitro</i> release studies of vitamin D3 .....	65
4.2.5.	Instrumentation.....	65
4.3.	Results and Discussion .....	66
4.3.1.	Loading of vitamin D3 into pSi particles.....	66
4.3.2.	Evaluation of loading capacities of VD into pSi.....	70
4.3.3.	Differential scanning calorimetry (DSC) analysis.....	71
4.3.4.	X-ray diffraction (XRD) analysis.....	72
4.3.5.	<i>In vitro</i> release of the VD from pSi.....	73
4.4.	Summary.....	74

V.	Loading and Release of <i>Equisetum Arvense</i> Leaf Extract (Anti-inflammatory & Anti-Oxidant) From Porous Silicon Powders.....	75
5.1.	Introduction.....	76
5.2.	Experimental.....	78
5.2.1.	Soxhlet extraction of <i>Equisetum arvense</i> leaves.....	78
5.2.2.	Loading of <i>Equisetum arvense</i> leaf extract into pSi.....	78
5.2.3.	Luciferase assay.....	79
5.2.4.	Preparing a standard curve for the <i>E. arvense</i> extract (anti-oxidant activity).....	80
5.2.5.	Preparing a standard curve for the <i>E. arvense</i> extract (anti-inflammatory activity).....	81
5.2.6.	In vitro release of <i>E. arvense</i> extract from pSi microparticles.....	81
5.2.6.1.	Release of anti-inflammatory compounds.....	82
5.2.6.2.	Release of anti-oxidant compounds.....	82
5.2.7.	Instrumentation.....	83
5.3.	Results and Discussion .....	83
5.3.1.	Loading of <i>E. arvense</i> ethanol leaf extract into pSi.....	83
5.3.2.	Differential scanning calorimetry (DSC) analysis.....	84
5.3.3.	X-ray diffraction (XRD) analysis.....	85
5.3.4.	Release of anti-inflammatory compounds form pSi particles.....	86
5.3.5.	Release of anti-oxidant compounds form pSi particles.....	89
5.4.	Summary.....	89
VI.	Plant Derived Porous Silicon Nanoparticles for Gene Delivery.....	91
6.1.	Introduction .....	92
6.2.	Experimental .....	96
6.2.1.	Size reduction of porous silicon nanoparticles (pSiNPs).....	96
6.2.2.	Aminosilanization of porous silicon particles.....	97
6.2.3.	PEG functionalization of pSiNPs.....	97
6.2.4.	Complexation of DNA with pSiNPs and LyoVec.....	97
6.2.5.	Quantifying number of amine groups.....	99
6.2.6.	DNA encapsulation studies.....	100
6.2.7.	Transfection of HEK 293 cells.....	100
6.2.8.	Instrumentation.....	101
6.3.	Results and Discussion .....	101
6.3.1.	TEM analysis of pSiNPs.....	103
6.3.2.	Surface modification and DNA binding studies.....	103
6.3.3.	Transfection experiments.....	105
6.4.	Summary .....	109
VII.	Concluding Remarks.....	110
VIII.	References .....	114

Vita and abstract

## LIST OF FIGURES

1. Pore classification scheme: interconnected pores (a), passing/ through pore (b), dead-end pore (c) closed pores (d).....	3
2. Schematic diagram of Si anodic etching.....	4
3. a) SEM images of porous wafers etched at different current densities. b) Graph of the variation in the porosity versus the current density.....	5
4. Comparison of porosity values of layers formed on heavily doped p-silicon and on heavily doped n-silicon, as a function of forming current density.....	6
5. Mechanism of electrochemical etching of silicon in hydrofluoric acid (HF).....	7
6. Schematic diagram of metal assisted etching shows metal deposition and pore formation.....	9
7. a) Au particles deposited on the silicon wafer after etching for 1 hr, and b) Pt particles deposited on the silicon wafer after etching for 5 min.....	9
8. SEM images of pSi pore morphologies obtained by magnesiothermic reduction of a) rice husk, b) silica spheres and c) diatoms at a temperature of ~650 °C using NaCl as thermal moderator.....	12
9. Dissolution kinetics of porous silicon at simulated physiological conditions. Medium (62%) porosity film; high (83%) porosity film; and very high (88%) porosity film.....	13
10. Degradation kinetics of PEG functionalized pSi microparticles: Graph shows total Si contents released to the degradation medium vs time (in PBS pH 7.2).....	14
11. a) Loading of the peptide (LACT-dKK) into the pSi, b) release of peptide from pSi matrix, c) 24 h survival rate of mice (treated with PBS, pSiNPs, and peptide- pSi particles), d) Bacterial count per lung after treating with PBS and peptide-pSiNPs.....	18
12. a) pSi immobilization with <i>E. coli</i> antibody b) antibody -antigen interactions upon adding water samples c) decreased amplitude (intensity) of the FFT peak of the porous film d) optical microscopy images of cells captured onto the biosensor.....	21



13. a) Osteoblast adhesion on macroporous Si, b) formation of collagen 1 fibrous matrix on macroporous silicon, c) formation of bone apatite like material .....	22
14. Eco-friendly fabrication route for deriving pSi from silicon accumulator plants. a) Optical image of ground tabasheer and horsetail powders, b) calcination of ground powders in a tube furnace, c) magnesiothermic reaction of calcinated powders, and pure pSi powder obtained after washing with 36% HCl.....	26
15. Standard curve developed by ammonium molybdate assay using standard silica samples, absorbance measured at $\lambda_{\max}$ 725 nm.....	29
16. SEM-EDX analysis on <i>E. telmateia</i> before HCl wash, inset shows the SEM image of a particle from ground powder.....	30
17. SEM-EDX analysis on <i>E. telmateia</i> after HCl wash; inset shows the SEM image of a particle from ground powder.....	31
18. SEM images of: a) pSiO <sub>2</sub> derived from tabasheer powder, b) pSi derived from tabasheer powder, c) pSiO <sub>2</sub> extracted from horsetail ( <i>E. telmateia</i> ) powder, d) pSi derived from <i>E. telmateia</i> fronds.....	32
19. SEM images of: a) Free standing pSi particle derived from tabasheer, b) individual nanopores along the pSi particle surface (tabasheer), c) image of pSi particle derived from horsetail, d) individual nanopores along the pSi particle surface ( <i>E. telmateia</i> ).....	33
20. SEM-EDX analysis on pSi derived from tabasheer.....	33
21. SEM-EDX analysis on pSi derived from horsetail.....	34
22. TEM images of tabasheer derived pSi a) low magnification image of free standing pSi microparticle, b) high resolution TEM image with a small silicon crystalline domains, inset shows FFT diffraction pattern, c) high resolution TEM lattice imaging , inset shows diffraction pattern on of silicon nanocrystallite.....	35
23. TEM images of pSi derived fronds of <i>Equisetum telmateia</i> . a) Low magnification image of free standing pSi particle and b) high resolution TEM images, inset shows FFT diffraction pattern. c) TEM lattice imaging, inset shows diffraction pattern on of silicon nanocrystallite.....	35
24. X-ray diffraction pattern of porous silicon derived from tabasheer.....	36
25. X-ray diffraction pattern of porous silicon derived from horsetail.....	36

26. Raman spectrum of porous silicon derived from a) tabasheer, b) <i>E. telmateia</i> fronds.....	37
27. FTIR spectrum of porous silicon derived from tabasheer.....	37
28. Brunauer–Emmett–Teller (BET) analysis on pSi derived from tabasheer.....	38
29. Dissolution studies (up to 8 weeks) on pSi samples in 0.9% NaCl solution.....	40
30. Flow chart diagram of initial fractionation of <i>Bambuseae arundinacea</i> ethanol leaf extract.....	47
31. Flow chart diagram of separation of phytochemicals from combined fractions of chloroform and ethyl acetate.....	48
32. Thermogravimetric analysis (TGA) of the extract loaded into pSi.....	50
33. The release of antibacterial components from <i>Bambuseae</i> leaf extract loaded pSi (tabasheer derived) and their associated activity against <i>S. aureus</i> .....	51
34. <sup>1</sup> H NMR spectrum of compound (1) in CDCl <sub>3</sub> (400 MHz).....	53
35. <sup>13</sup> C NMR spectrum of compound (1) in CDCl <sub>3</sub> (400 MHz).....	54
36. HRMS (ESI-TOF) data for compound 1.....	55
37. <sup>1</sup> H NMR spectrum of compound (2) in CDCl <sub>3</sub> (400 MHz).....	56
38. <sup>13</sup> C Compound (2) in CDCl <sub>3</sub> (400 MHz).....	57
39. HRMS (ESI-TOF) data for compound 2.....	58
40. Loading pSi powders with vitamin D3.....	63
41. Calibration curve for vitamin D3 prepared in 65% ethanol (in water containing 7 mM tween 80).....	64
42. Calibration curve for vitamin D3 prepared in 95% ethanol.....	65
43. Heat induced oxidation of Vitamin D3.....	66

44. Mass spectrum of melted vitamin D3 .....	67
45. Mass spectrum of melted vitamin D3 at 95°C for 20 min.....	68
46. Mass spectrum of vitamin D loaded into pSi by melt loading method.....	69
47. Thermogravimetric analysis of a) VD loaded into pSi by melt loading, b) VD loaded into pSi by incipient wetness impregnation.....	70
48. Differential scanning calorimetry of pSi loaded with vitamin D3.....	72
49. Over lay of XRD pattern of vitamin D3, pSi loaded with vitamin D3 by melt load and incipient load methods.....	73
50. Release of soluble vitamin D3 from VD-loaded pSi.....	74
51. Mechanism of NF- $\kappa$ B activation through TNF $\alpha$ .....	77
52. Schematic representation of the DPPH assay.....	78
53. Schematic representation of luciferase assay.....	80
54. Standard curve developed by <i>E. arvense</i> ethanolic leaf extract by DPPH assay.....	81
55. Standard curved developed by measuring the anti-inflammatory activity of known conc. of <i>E. arvense</i> ethanol extract by luciferase assay.....	82
56. TGA analysis of <i>E. arvense</i> extract loaded pSi particles by solution load method.....	84
57. Overlay of DSC thermograms of <i>E. arvense</i> extract and extract loaded into pSi.....	85
58. XRD analysis of <i>E. arvense</i> , before and after loading into pSi microparticles.....	86
59. <i>In vitro</i> release of the anti-inflammatory components from pSi loaded with <i>E. arvense</i> extract.....	87
60. Anti-inflammatory activity of the <i>E. arvense</i> extract and extract loaded pSi powders. All the samples were spiked with (50 $\mu$ g/mL) of <i>E. arvense</i> extract.....	88
61. <i>In vitro</i> release of anti-oxidant components from <i>E. arvense</i> extract loaded pSi microparticles.....	89

62. Mechanisms of endosomal escape. (a) Flip-flop. (b) Proton sponge.....	92
63. Size separation of porous silicon particles by fractional centrifugation.....	97
64. a) APTES functionalization of pSiNPs, b) PEG functionalization of pSiNPs c) DNA complexation of pSiNPs (pSiNP-APTES and pSiNP-PEG).....	98
65. Standard curve obtained from ninhydrin-glycine colored complex at 565 nm.....	99
66. a) TEM image and corresponding size distribution of tabasheer powder after milling b)TEM image and corresponding size distribution of pSiNPs derived from the milled tabasheer.....	102
67. a) EDX analysis of pSiNPs derived from milled tabasheer. b) HRTEM images of pSiNPs .....	102
68. Zeta potentials of the pSiNPs, pSiNP-APTES, and pSiNP-APTES-DNA complexes....	103
69. Internalization of a) pSiNPs, b) pSiNP-APTES and c) pSiNP-APTES-DNA complexes into HEK 293 cells after 48 h transfection.....	106
70. HEK 293 cells treated with pSiNP-APTES-DNA complex expressed eGFP after 48 h transfection.....	107
71. HEK 293 cells treated with LyoVec-DNA complex, expressed eGFP after 48 h transfection.....	107

## LIST OF TABLES

1. BET analysis on pSi samples (tabasheer derived) used for dissolution studies.....	40
2. Antibacterial activity of four fractions Fr.1, Fr.2, Fr.3, and Fr.4 obtained from disc diffusion assay (against <i>S. aureus</i> ).....	47
3. Antibacterial activity of leaf extracts from <i>Bambuseae arundinacea</i> against <i>S. aureus</i> ...	49
4. Antibacterial activity (against <i>S. aureus</i> ) of bamboo extract and extract loaded pSi after 24 h incubation period.....	50
5. Vitamin D3 loading capacities into tabasheer derived pSi using different methods.....	71
6. Plasmid DNA loading capacities at various weight ratios of pSiNP-APTES/DNA, and incubation times.....	104

**Chapter I**  
**Literature Review**

## **1. Introduction**

Porous Si (pSi) was discovered by Uhlir in 1956 at Bell Laboratories, USA. He discovered it accidentally while electrochemically polishing silicon wafers in hydrofluoric acid (HF) to use them in microelectronic circuits.<sup>1</sup> Under the conditions used, the silicon wafer did not dissolve uniformly, and a porous morphology was not noticed at that time. Later, this material gained interest because of its high surface area, as a substitute for crystalline Si surface for spectroscopic studies.<sup>2</sup> In 1971, Watanabe and Sakai reported the porous nature of Si etched in HF.<sup>3</sup> In 1990, Ulrich Gosele and Volker Lehmann identified quantum confinement effects in the absorption spectrum of pSi.<sup>4</sup> During the same time period Leigh Canham discovered a bright visible photoluminescence attributed to quantum confinement effects associated with nanocrystalline Si domains within the pore walls.<sup>5</sup> After these discoveries, pSi has gained extensive interest because of its potential optoelectronic properties.<sup>6</sup> pSi has flourished in several other fields: biomedicine,<sup>7</sup> diagnostics,<sup>8</sup> cosmetics,<sup>9</sup> food & nutrition,<sup>10</sup> because of high surface to volume ratios, tunable porosities, ease of surface modification and biodegradability.

Both bottom up and top down fabrication methods are available to make pSi structures. ‘Top down’ methods involve chemical etching of solid silicon feedstock and ‘bottom up’ methods involve chemical conversion of silica to silicon.<sup>11</sup> Conventional top down methods along with alternative bottom up methods will be discussed in this chapter.

### **1.1. General pore classification of solids**

Porous solids are classified according to the accessibility of pores to the surrounding medium.<sup>12</sup> The following is a list of common pore types: interconnected open pores, open pores at two ends (passing/ through pores), open pores at one end (dead-end pores), and pores that do not have access to surrounding medium (closed pores).<sup>13</sup>

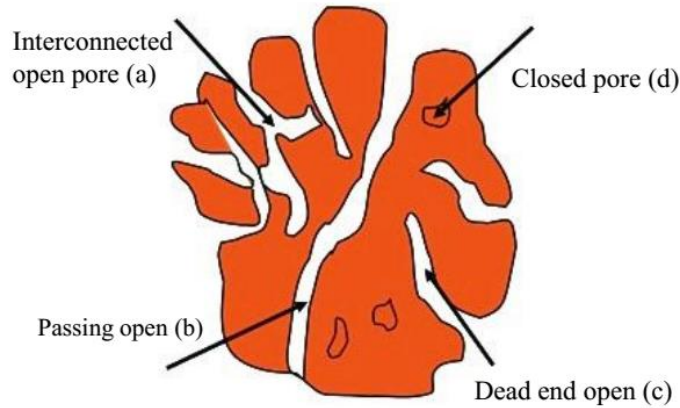


**Figure1.** Pore classification scheme: interconnected pores a), passing/ through pore b), dead-end pore c) closed pores d). Adapted from ref 12.

Open pores are accessible to the surrounding medium, some are open only at one end (a &c), and some are open at two ends (b). Of these, dead end (c), and interconnected open pores are common in porous solids. Closed pores (d) are typically formed when collapsing open pore walls are exposed to high temperatures.

## 1.2. Pore size classification in porous solids

Based on IUPAC recommendations for characterization of porous solids, porous materials are classified based on their pore size diameter. Pore diameter is defined as the average distance between pore walls. This classification does not contain any information of pore morphology e.g. geometry, orientation, interconnectivity of pores, etc. Porous materials classification, according to IUPAC, is as follows: microporous (< 2 nm), mesoporous (2-50 nm), and macroporous (> 50 nm).<sup>14</sup>

## 1.3. Fabrication methods of pSi

### 1.3.1. Anodic etching

Anodic etching of silicon refers to the formation of pores in crystalline Si (typically in wafer form) under an anodic bias in a fluoride-based electrolyte solution. Anodization conditions play a major role in determining the porosity, pore size and morphology of a given porous Si



film. These conditions include: current density, type of dopant, doping concentration, crystal orientation, electrolyte composition, and duration of the etching process etc.<sup>15</sup> A typical anodization setup is shown in Fig.2. An electrochemical cell comprised of an inert cathodic counter electrode (usually platinum) and silicon working electrode (anode). Addition of a wetting agent to the electrolyte solution (methanol or ethanol) improves the dissolution process by removal of H<sub>2</sub> gas produced during the etching process. In general, porosity values between 10-80% with a wide range of pore sizes (micro, meso and macro) can be obtained by varying the electrochemical parameters.<sup>16,17</sup>

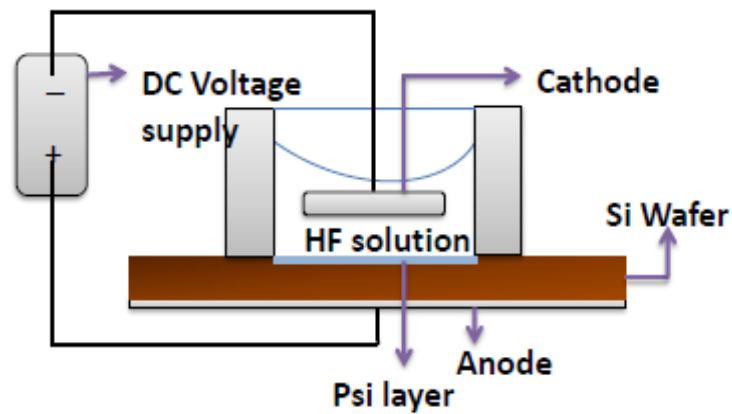


**Figure 2.** Schematic diagram of Si anodic etching.

Earlier studies have focused on optimizing the Si porosities by changing the current density during the anodization. Fig. 3 shows change in porosity of Si wafer with current density. These Si wafers were boron doped (p++) with a resistivity of 0.00055–0.001  $\Omega$ .cm, with 100 crystallographic orientation and the etchant was aqueous hydrofluoric acid (HF, 48%)/ethanol solution. Fig 3a-(i), 3a-(ii), and 3a-(iii) shows SEM images of silicon wafer etched at current densities of 5.7 mA cm<sup>2</sup>, 28.4 mA cm<sup>2</sup> and 56.8 mA cm<sup>2</sup> resulted in pore sizes ranging from 22-

33 nm, 27-42 nm, and 34-58 nm respectively. Fig. 3(b) shows change in porosity with increased current densities.<sup>16</sup>

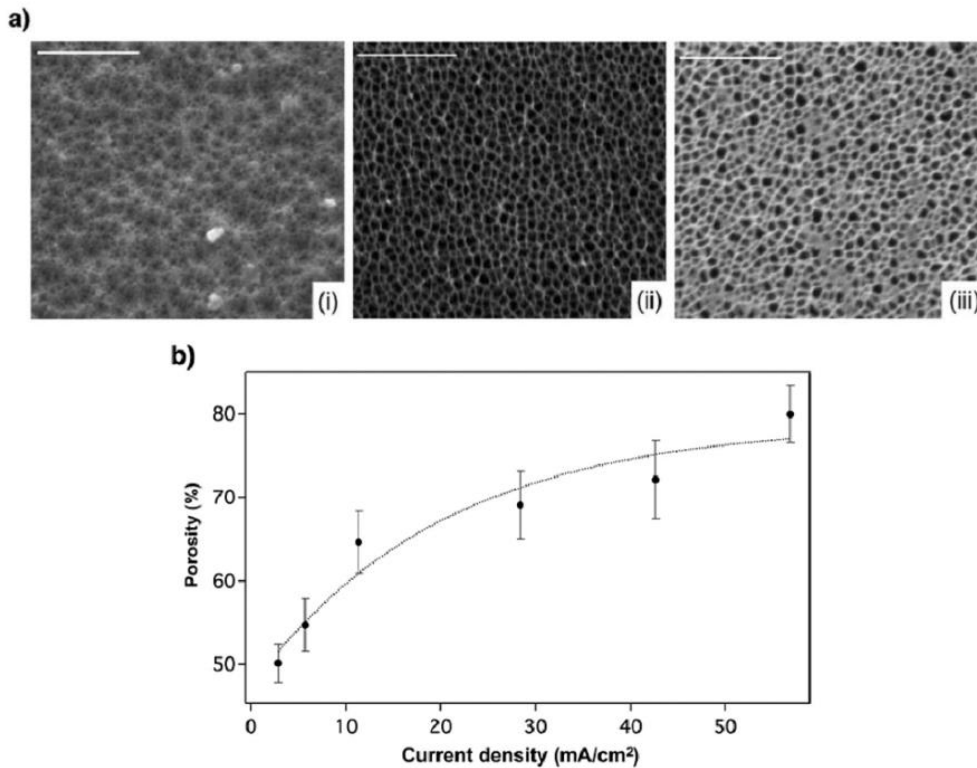


**Figure3.** a) SEM images of porous wafers etched at different current densities. Scale bars are 500 nm. b) Graph of the variation in the porosity versus the current density. Adapted from ref 16.

Other important parameters to optimize the porosity are dopant type and dopant concentration. Lehmann *et al.* studied the dependency of pore size and porosity on dopant type and doping concentration.<sup>17</sup> Micro pSi is produced by electrochemical etching of n-type wafers at a low dopant concentration of  $10^{16} \text{ cm}^{-3}$ . Etching p-type Si wafers at moderate to high doping levels ( $10^{17} \text{ cm}^{-3}$  -  $10^{20} \text{ cm}^{-3}$ ) showed formation of meso pSi structures. In the case of n-type silicon wafers it is found that with increased doping density there is an increase in porosity within the Si films. This phenomenon was also observed by Herino *et al.* where they found that porosity obtained for n-type substrates are highly sensitive to doping level compared to the p-type substrates.<sup>18</sup> In this study Herino *et al.* reported different porosities of Si films prepared

under the same conditions (15% HF, at a current density of  $30 \text{ mA/cm}^2$ ) on n-type substrates with different resistivities. For a  $1 \mu\text{m}$  thick Si wafer with varied resistivities the following porosities were reported: 50% for  $0.007 \Omega\cdot\text{cm}$ , 25% for  $0.015 \Omega\cdot\text{cm}$ , and only 15% for  $0.030 \Omega\cdot\text{cm}$ . The observed porosity differences were large, for a low decrease in doping level, when compared with p-substrates; the difference in porosity is 10% with change in dopant concentration by factor of 10. Fig. 4 shows the porosity dependence of dopant type at different current densities. p-type and n-type silicon wafers with resistivities of  $0.01 \Omega\cdot\text{cm}$  were etched with HF (25% V/V). p-type showed larger porosities compared to n-type layers.

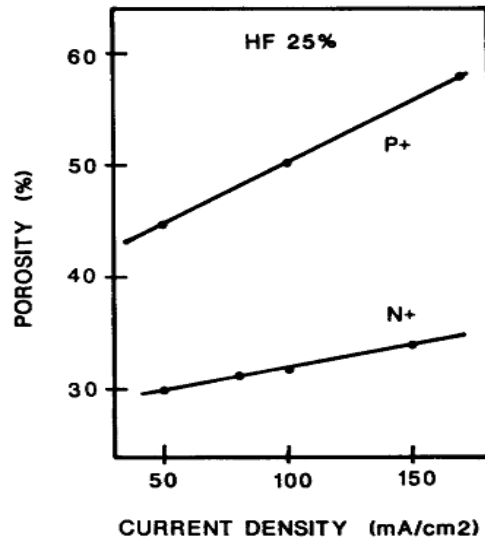


**Figure4.** Comparison of porosity values of layers formed on heavily doped p-silicon and on heavily doped n-silicon, as a function of forming current density. Adapted from ref 18.

Chemical dissolution of silicon under anodic bias takes place by the following mechanism. When a positive current is passed through the silicon electrode, chemical dissolution of silicon takes place by diffusion of the holes to the surface. During this process, fluoride ions ( $\text{F}^-$ ) from the electrolyte solution, replace the superficial H atoms to create neutralized Si-F bond. Following this process, a new  $\text{F}^-$  atom binds to the Si atom at a different position and

produces hydrogen gas. As this reaction progresses Si–Si bond weakens by the strong electronegativity of  $F^-$  atoms through nucleophilic attack. Pores are generated as a consequence of dissolution of Si (in the form of  $SiF_6^{-2}$ ) from the surface.<sup>19</sup>

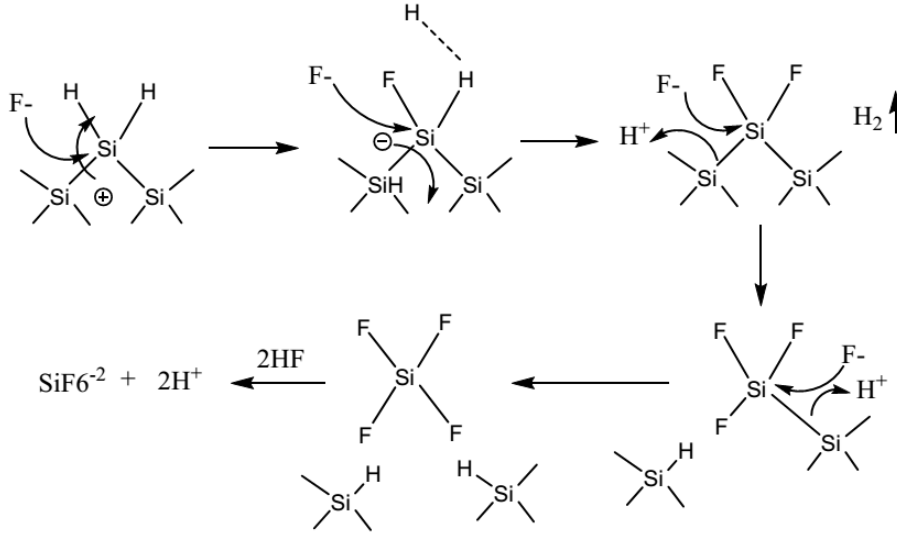
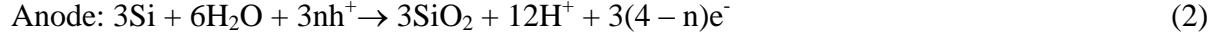
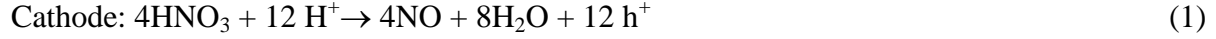


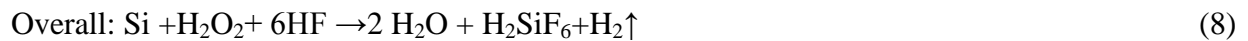
**Figure 5.** Mechanism of electrochemical etching of silicon in hydrofluoric acid (HF). Redrawn from ref 19.

### 1.3.2. Stain Etching

Stain etching refers to the etching of silicon in absence of power supply where a chemical oxidant acts as a hole ( $h^+$ ) injector.<sup>20</sup> As in the case of anodization, fluoride ion is needed as an etchant which can be supplied by HF. By far the most commonly used oxidant is  $HNO_3$ . The rate of the etching is optimized by changing several parameters: etchant composition, time of etch, intrinsic properties of silicon (dopant type and dopant density) and temperature.<sup>21</sup> The most commonly-used etchant composition is  $HF/HNO_3/H_2O$ .<sup>22</sup> The mechanism of etching process is defined in two steps. The first step is injection of the holes into the valence band of the silicon by reduction of nitric acid (with oxidation of silicon to silica) at the cathode (eq 1); the second step is dissolution of formed silica at anode (eq 2 and 3). The overall reaction is written in eq 4, where  $n$  is the average number of holes required to dissociate one Si atom.<sup>23</sup>



Metal assisted chemical etching (MACE) is based on the dissolution of the silicon by HF in presence of a metal oxidant. Usually a noble metal is used in this process that catalyzes the reduction of oxidant. This process dissolves the silicon underneath the metal much faster than the silicon without metal coverage.<sup>24</sup> Metal particles are deposited on the silicon substrate as nanoparticles, or thin films by using chemical vapor deposition, or by sputtering.<sup>25</sup> After deposition of the metal on the silicon substrate, it is placed in the etchant solution (typically HF/H<sub>2</sub>O<sub>2</sub>). The metal particles reduce the oxidant and produce the holes at cathode (eq 5). The holes are then injected into the valence band of Si at the interface between metal and silicon substrate. Various mechanisms were proposed for dissolution process of silicon (anode reaction). Of which, most widely accepted Si dissolution mechanisms are given in eq 6, and eq 7 respectively.<sup>26</sup> The overall reaction shows dissolution of silicon in the form of H<sub>2</sub>SiF<sub>6</sub> along with hydrogen evolution (eq8). As the reaction proceeds, pores are formed while metal particles sink into the Si pores.<sup>27</sup> Fig. 6 shows a schematic diagram of metal assisted etching.



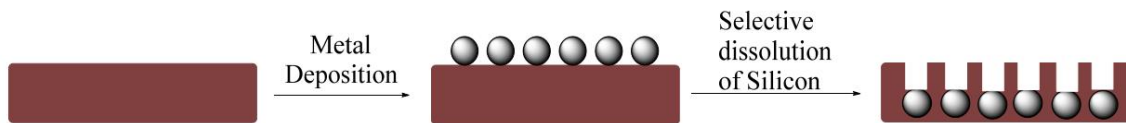


**Figure 6.** Schematic diagram of metal assisted etching shows metal deposition and pore formation

As in case of stain etching, etch rate and morphologies created after the MACE depends on etchant composition, metal type and its shape, distance between the metal particles, intrinsic properties of silicon substrate, and temperature etc.<sup>28</sup> Fig.7 shows pore morphologies created with different noble metals. p-type Si wafer with (100) crystallographic orientation was used in these studies with an etchant composition of HF/H<sub>2</sub>O<sub>2</sub>/H<sub>2</sub>O. Fig. 6a shows Au particles deposited on a silicon wafer after etching and Fig. 6b shows Pt particles deposited silicon wafer after etching.<sup>29, 30</sup>

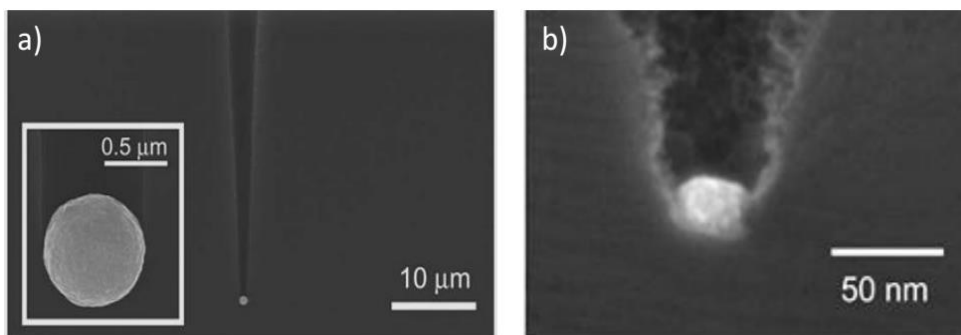


**Figure 7.** a) Au particles deposited on the silicon wafer after etching for 1 hr, and b) Pt particles deposited on the silicon wafer after etching for 5 min. Adapted from ref 29, 30.

In these two individual studies the following results were reported. The pores on Si substrates etched in the presence of Pt were surrounded by a porous layer, whereas there is no observable porous layer found around the etched Au-coated substrates. Also the etch rates were faster with platinum over gold. There is no solid explanation on how these metals creates the

differences in the etch morphologies and rates but this can be attributed to the catalytic activity of the noble metal for the H<sub>2</sub>O<sub>2</sub> reduction.<sup>30</sup>

### **1.3.3. Reducing silica to silicon**

#### **1.3.3.1. General concepts**

The primary means of producing metallurgic silicon from silica is carbothermal reduction at >2000 °C.<sup>31</sup> Silicon liquefies at these high temperatures, and associated morphologies with silica will be destroyed.<sup>32</sup> In order to preserve any porous morphologies of silica, fabrication methods that involve low operating temperatures are needed. As an alternative route to electrochemical etching methods, the chemical conversion of porous silica to silicon by using a metal reducing agent at low reaction temperatures is gaining more attention.<sup>33</sup> Magnesium is a commonly used reducing agent to reduce silica to silicon, other alternative agents are calcium and lithium.<sup>34</sup> Nohira *et al.* showed conversion of silica to silicon at temperatures lower than ≤850 °C via electrochemical reduction using calcium in a molten salt bath electrolyte.<sup>35</sup> Yasuda *et al.* were able to produce sponge like silicon structures at molten temperatures of 500 °C using lithium as a reducing agent. However, the silicon products formed by these electrochemical reduction methods did not retain their nanoscale morphology.<sup>36</sup>

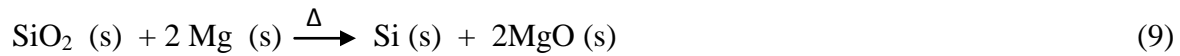
#### **1.3.3.2. pSi derived from biogenic sources**

Magesiothermic reduction from the rice husks was first introduced in 1980 by two groups, Banerjee *et al.* and Bose *et al.*<sup>37,38</sup> They were trying to fabricate solar grade solid silicon from rice husks and they found that the purity of their final product was inadequate to build a solar cell. Unlike electrochemical reduction methods, use of magnesium as a reducing agent can lower the reaction temperature to the range of 550-650 °C. By using low reduction temperatures, pore morphologies from silica can be retained while silicon is formed.<sup>32</sup>

Later, in 2007 Bao *et al.* converted *Aulacoseira* silica diatom frustules to microporous silicon diatoms using magnesium as a reducing agent.<sup>33</sup> Various forms of biogenic silica feedstocks (diatoms, rice husk ash, *Equisetum arvense* etc.) have been used so far to reduce silica to silicon by magnesiothermic reduction.<sup>39-43</sup>

### 1.3.3.3. Details of magnesiothermic reduction process

Magnesiothermic reduction is highly exothermic in nature ( $\Delta H = -546.42$  kJ/ mol).<sup>47</sup> The magnesiothermic reduction reaction occurs as written below:



During the reaction, temperature of the reaction is raised up to 800 °C, which might lead to collapse of porous morphologies and agglomeration. To overcome this problem a thermal moderator can be used to scavenge the heat produced by reduction. When sodium chloride ( $\Delta H_{\text{fusion}} = 28.8$  kJ/mol),<sup>48</sup> is used as thermal moderator, the heat produced is used to melt NaCl rather than fuse of Si.<sup>49,50</sup>

The completion of the reduction process (Silica to silicon conversion) depends on the homogeneity of the reactant mixture. In a typical vapor-transport reaction, silica precursors are located at a distance (1-2.54 cm)<sup>44,45</sup> from magnesium in the oven, as ‘Mg’ vapor diffuses to react with silica, the reaction proceeds by forming three inhomogeneous phases  $\text{Mg}_2\text{Si}$  (magnesium silicide), Si and unreacted  $\text{SiO}_2$ .<sup>46</sup> Products near the Mg source convert to  $\text{Mg}_2\text{Si}$  (eq 10), while the  $\text{SiO}_2$  far from Mg source will not be reduced. The following reaction shows the formation of unwanted  $\text{Mg}_2\text{Si}$  impurities. This can be avoided by premixing of all the reactants.<sup>46</sup>





Micro and mesoporous silicon structures have been fabricated using magnesiothermic reduction with high surface areas up to  $500 \text{ m}^2/\text{g}$  in the presence of a thermal moderator.<sup>49-51</sup> Fig. 8 shows SEM images of pSi structures derived from rice husk, silica spheres and diatoms.

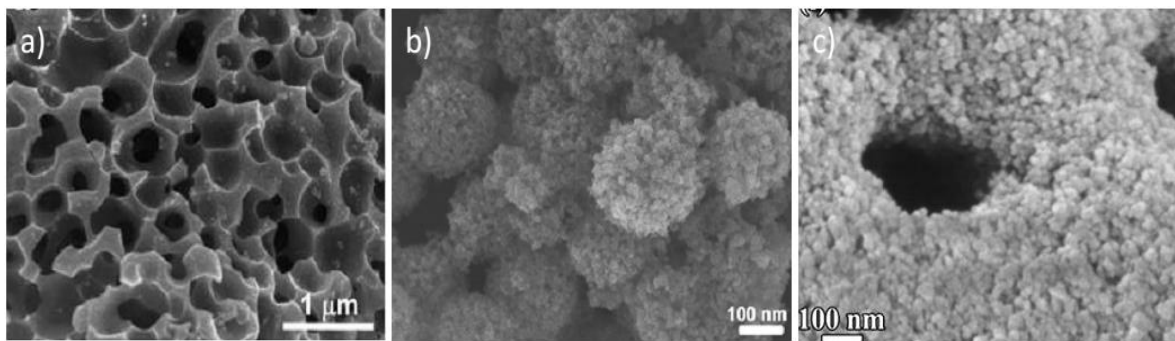


**Figure 8.** SEM images of pSi pore morphologies obtained by magnesiothermic reduction of a) rice husk, b) silica spheres and c) diatoms at a temperature of  $\sim 650 \text{ }^\circ\text{C}$  using NaCl as thermal moderator. Adapted from references 39, 41 and 42.

#### 1.4. pSi as a Biomaterial

Porous silicon is a promising biomaterial for a broad variety of applications: *in vivo* biosensors, tissue engineering, and drug delivery.<sup>51-53</sup> Biocompatibility and biodegradability of the pSi is attributed to its unique physicochemical properties. These properties include porosity, pore size, Si feature size, and surface chemistry.<sup>54</sup>

*In vitro* biodegradability of pSi was first identified by Canham *et al.* in 1995,<sup>55</sup> Later Anderson *et al.* showed anodized porous Si films release orthosilicic acid  $\text{Si}(\text{OH})_4$  upon dissolution at physiological conditions.

Their studies showed complete degradation of mesoporous Si films ( $1 \text{ } \mu\text{m}$  thickness) with high porosity (70 %) in simulated body fluid (SBF) within a day (Fig. 9).<sup>56</sup> Reffitt *et al.* showed orthosilicic acid ( $\text{Si}(\text{OH})_4$ ) was readily absorbed in the gastrointestinal tract and non-toxicly eliminated via urine from the kidneys.<sup>57</sup>

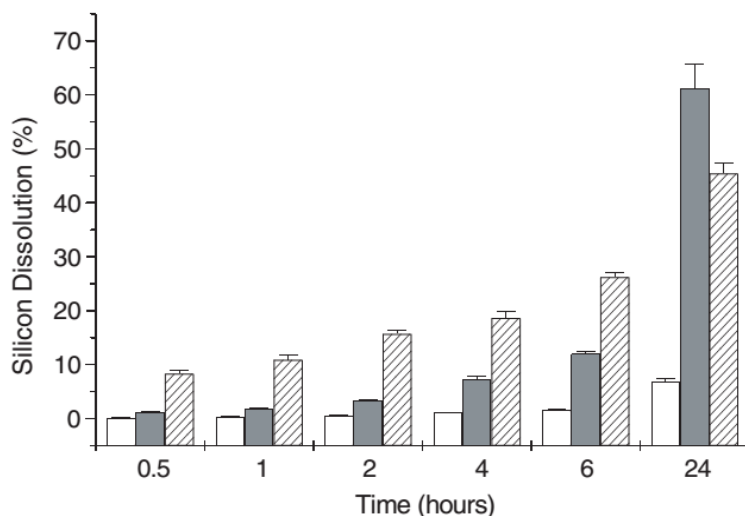


**Figure 9.** Dissolution kinetics of porous silicon at simulated physiological conditions. Medium (62%) porosity film (white); high (83%) porosity film (grey); and very high (88%) porosity film (hatched). Adapted from ref 57.

Along with porosity and surface chemistry, pore size also alters the degradation kinetics of the pSi matrix. Degradation profiles of pSi modified with commonly used surface linkers were studied by Godin *et al.*<sup>58</sup> This study shows that the degradation of pSi particles is faster in case of large pore size particles (30-50 nm) compared to 10 nm size pores. Degradation kinetics of pSi particles (pore size 30-50 nm) conjugated with polyethylene glycol (PEG) with varying molecular weights (245, 333, 509, 686, 1214, 3400, and 5000 Da) showed slow degradation rates with increasing molecular weight and that half-life of the matrix can be prolonged up to 3 days in case of PEG 5000 linker (Fig.10).

In the same study Godin *et al.* also showed *in vitro* biocompatibility of polyethylene glycol (PEG) and (3-aminopropyl)triethoxysilane (APTES) functionalized pSi particles. Mesoporous Si particles of this type showed good biocompatibility with no induced release of pro-inflammatory cytokines in THP1 human macrophages.<sup>58</sup>

*In vivo* biocompatibility of pSi subcutaneous implants were assessed by Bowditch *et al.*<sup>59</sup> After a 26 week evaluation they found that these implants were biocompatible with no observable inflammation, fibrosis, and necrosis in the vicinity of implant. Park *et al.* also showed that *in vivo* degradation of the anodized pSi nanoparticles (120 nm) renally cleared in the form of silicic acid within 24 h, with no evidence of toxicity in a mouse model.<sup>60</sup>

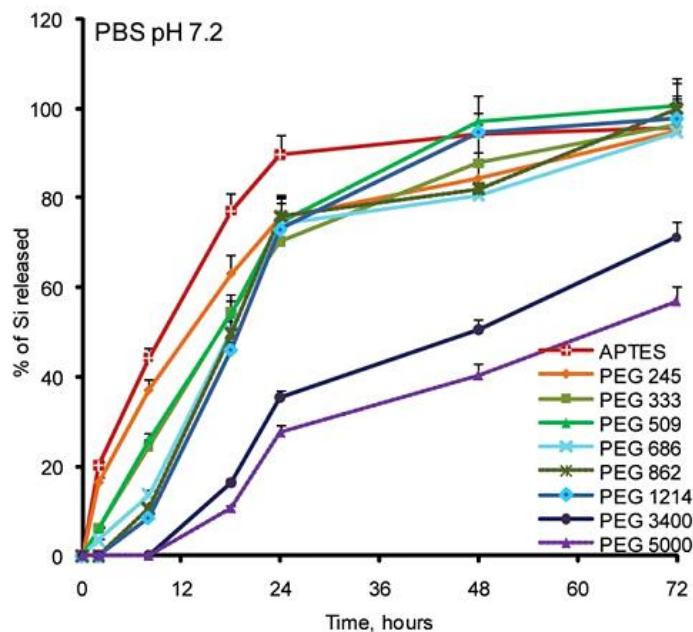


**Figure 10.** Degradation kinetics of PEG functionalized pSi microparticles: Graph shows total Si contents released to the degradation medium vs time (in PBS pH 7.2). Adapted from ref 58.

#### 1.4.1. Porous silicon as drug delivery carrier

The fabrication routes of pSi provide construction of nanostructured materials with high surface area to volume ratios, controllable pore sizes, along with different pore morphologies. These features offer loading of high drug payloads within the porous matrix. A wide variety of convenient surface modification techniques allows delivery of the drugs to specific areas, co-delivery of drugs.<sup>61,62</sup> By tuning the surface chemistry the release rate of the drugs can be controlled along with the resorption rate of the pSi matrix.<sup>63</sup>

A number of critical review articles have been published regarding the reactivity of pSi with drugs, drug loading methods, and range of payload molecules (antimicrobials, anticancer, proteins etc) loaded into pSi.<sup>64-67</sup> This section highlights some of the studies on the reactivity of pSi, brief discussion on commonly-used loading methods, and recently published literature reports on pSi as drug delivery carrier.

One of the main challenges of loading drugs into pSi is its highly reactive hydride  $\text{Si}_y\text{SiH}_x$  ( $x + y = 4$ ) species. These surface functionalities shown to have undesirable reactions with some drugs and bioassays leading to degradation of drugs or false positive results. Wu *et al.* showed degradation of daunorubicin, an anticancer drug by pSi reactivity (reducing ability).<sup>68</sup> Laaksonen *et al.* showed that the MTT reagent (3-(4,5-dimethylthiazol-2-yl)-2,5-diphenyltetrazolium bromide) was reduced by pSi instead of cellular reductase enzymes (NAD(P)H-dependent cellular oxidoreductase enzymes), lead to false positive results for the MTT assay.<sup>69</sup>

The unwanted reactivity of pSi can be overcome by surface passivation methods. The most commonly used methods for surface passivation are oxidation, hydrosilylation, and thermal carbonization.<sup>70</sup> Oxidation of the pSi is achieved by liquid phase oxidation by using chemical oxidants and thermal oxidation. Thermal oxidation ( $> 700$  °C) has dominated in the literature for drug delivery applications because of its simplicity and ability to produce relatively stable oxide with better stability in aqueous media.<sup>71</sup>

The common approaches to load an active therapeutic into pSi is by confining the active payload into the pores by physical entrapment, immobilizing them by covalent attachment, and by spontaneous adsorption.<sup>72</sup> In case of the physical entrapment the drug is forced to remain in the pores where it physically blocks the pore openings. On the other hand covalent attachment

onto the pSi surface provides stronger chemical interactions between the payload and the surface, and this method provides a means of attaching cleavable linkers for site specific drug delivery. In the case of adsorption the surface charge and hydrophobic or hydrophilic nature of the surface were taken into account to spontaneously adsorb same polarity molecules and oppositely charged payloads onto the surface of pSi (eg. proteins).<sup>73</sup> Covalent attachment and physical entrapment methods showed prolonged release of payload molecules for days to weeks (eg. daunorubicin, cobinamide, rhodamine B).<sup>74-75</sup> Whereas spontaneous adsorption method due to its weak interactions between the pSi surface and the payload, showed rapid release (few hrs) of payloads (ibuprofen).<sup>77</sup>

pSi based drug delivery systems have been used for various applications: to increase the stability and bioavailability, sustained release, targeted release, and in some cases for multistage drug release.<sup>78</sup> Some representative studies are listed here.

pSi for the improved bioavailability of drugs was studied by various groups. Salonen *et al.* studied dissolution behavior and subsequent release of drugs before and after loading into pSi.<sup>79</sup> They have loaded five model drugs (antipyrine, ibuprofen, griseofulvin, ranitidine and furosemide) with varied solubility profiles into the thermally carbonized pSi microparticles and their subsequent release behavior. They found that with poorly dissolving drugs (ibuprofen, griseofulvin and furosemide), loading into the mesoporous microparticles clearly improved dissolution. When the dissolution rate of the unloaded drug was high (antipyrine, and ranitidine), the microparticles caused a slightly delayed release.

Along with drug molecules, various vitamins and nutrients were also loaded into pSi to increase their stability and bioavailability. Some of the examples reported include, vitamin B9, lycopene and coenzyme Q10.<sup>80</sup>

pSi for sustained release of active therapeutics was studied on various disease models and one of the most extensively studied classes of agents are anticancer drugs. The following are selected examples of studies in this category. Coffey *et al.* studied the *in vitro* release of cisplatin, carboplatin, and ethylenediaminedichloro platinum within porous Si layers capped by calcium phosphate.<sup>81</sup> Vaccari *et al.* studied the *in vitro* release of doxorubicin-loaded porous silicon for the controlled release of the drug for killing adenocarcinoma cancer cells.<sup>82</sup> Gu *et al.* developed luminescent pSi particles loaded with superparamagnetic iron oxide nanoparticles and doxorubicin to magnetically guide the luminescent particles for *in vitro* delivery of this drug to treat cervical cancer.<sup>83</sup> Another drug release model is based on antibody modified pSi-camptothecin to target neuroblastoma, glioblastoma and B lymphoma cells developed by Secret *et al.*<sup>84</sup>

Another area that is extensively studied for pSi based sustained drug delivery is to treat microbial infections. *In vitro* model system for pH-triggered release of the antibiotic vancomycin from porous Si films were studied by Perelman *et al.*<sup>85</sup> pH-responsive delivery devices composed of pSi drug reservoirs capped with dual polymer layers composed of poly(1,7-octadiene) (POct) and PAAc were used to release levofloxacin (LVX), a broad spectrum antibiotic for *Pseudomonas aeruginosa* infections.<sup>86</sup> Sustained delivery of antibacterial agent triclosan to inhibit the bacterial growth was investigated by Wang *et al.*<sup>88</sup> Sustained antifungal activity from a ketoconazole loaded nanostructured mesoporous silicon was studied by Tang *et al.*<sup>87</sup>

Another area of interest is using pSi as a protective agent to minimize the toxicity of loaded drug or molecule of interest. Here is a detailed study that describes the use of pSi as a protective agent to load the toxic bacterial proteins to treat the bacterial infections. Recently Kwon *et al.* developed pSi based delivery of an anti-infective peptide for *Pseudomonas*

*aeruginosa* lung infections.<sup>88</sup> They synthesized a bifunctional peptide called lactoferrin-dKK (LACT-dKK), where LACT (lactoferrin) peptide (KCFQWQRNMRKVRGPPVSCIKR) can interact with the bacterial membrane and dKK, (D(KLAKLAK)) acts as a bacteriotoxin that can kill bacteria upon physical interaction with bacteria.<sup>88</sup> In order to minimize the toxic effects of this peptide they localized the peptide cargo (LACT-dKK) into pSi nanoparticles. Peptide was loaded into pSi particles by infiltration where cationic peptide is bound to the anionic phosphonates on the pSi particles (Fig 11a). Fig 11b shows *in vitro* release of the peptide from pSi matrix within 24 h (PBS, pH 7.2).

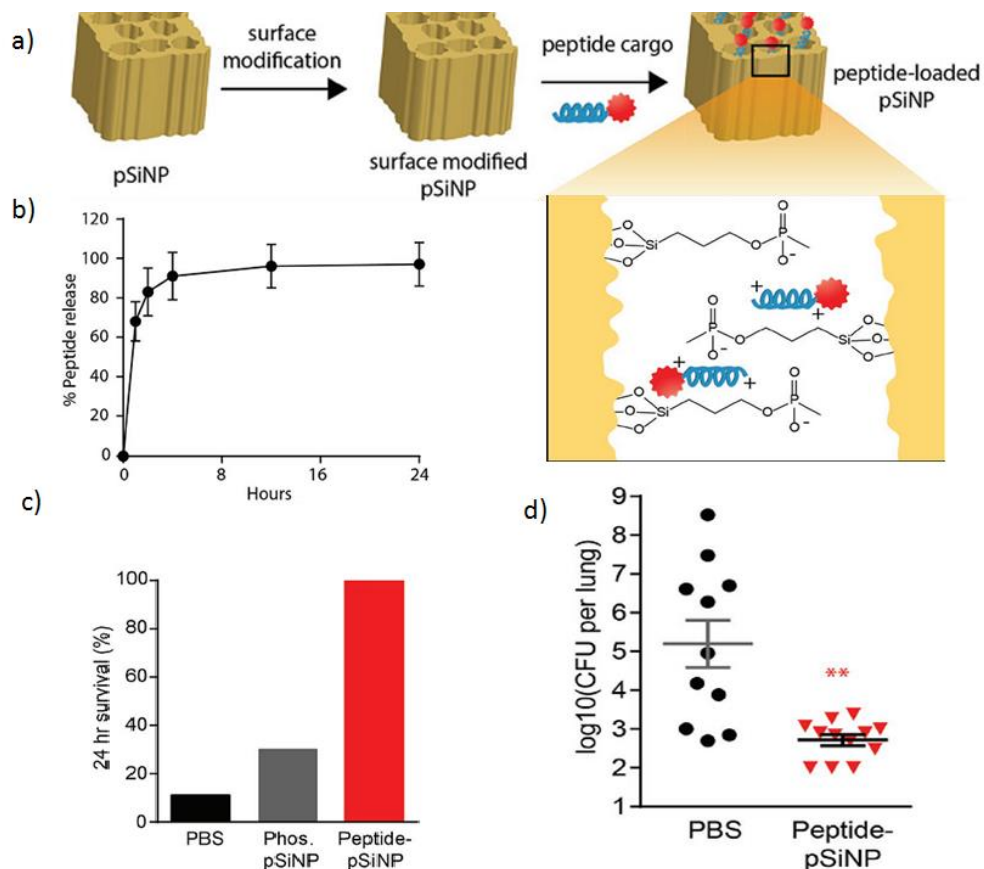


**Figure 11.** a) Loading of the peptide (LACT-dKK) into the pSi, b) release of peptide from pSi matrix, c) 24 h survival rate of mice (treated with PBS, pSiNPs, and peptide- pSi particles), d) Bacterial count per lung after treating with PBS and peptide-pSiNPs. Adapted from ref 88.

The release trend matches with the degradation behavior of pSi nanoparticles. Mice were infected with  $1 \times 10^3$  CFU *P. aeruginosa* / mouse to establish lung infection. Sample solutions were injected via a catheter into the trachea of the mice. They showed high survival rate of mice within 24 h in case of pSiNP-peptide treated mice (Fig. 11c). By contrast, they observed increased cytokinine production and evidence of damage in the lungs at 4 h after administration of free peptide. Fig. 11d shows the utility of this peptide–pSiNP platform *in vivo*, the untreated mice had high titer count per lung, whereas mice treated with peptide–pSiNP had lower count per lung.<sup>88</sup>

In this study the authors have developed an anti-infective nanomaterial with two functions: biodegradable pSi that localizes the toxic payload within the porous matrix to minimize the toxic effects and a novel tandem peptide cargo to localize the toxic payload to bacterial membranes. They have also shown that clinical isolates from human lung infections were susceptible to this peptide, which supports that this agent could be applied to other strains of *P. aeruginosa*.

#### **1.4.2. pSi as a biosensor**

pSi with its large surface area, adjustable pore size, tunable degradation, ease of surface modification, and biocompatibility makes it a versatile material for chemical and biosensing applications. Various biosensors were developed for detection of proteins, enzymes, and DNA.<sup>89-</sup>

<sup>91</sup> Most of these pSi based signal transduction methods were optical, electrochemical, and electrical. Some of the applications related to biosensing are detailed here.

Lugo *et al.* fabricated a pSi based electrochemical device that senses hybridization of DNA.<sup>92</sup> Nucleic acid (probe DNA) modified pSi electrodes were used to signal the hybridization



process by voltammetry using  $\text{Ru}(\text{bpy})_3^{+2}$  as an electrochemical redox indicator. The assay was developed based on the following principle. Under an applied potential,  $\text{Ru}(\text{bpy})_3^{2+}$  is oxidized to  $\text{Ru}(\text{bpy})_3^{3+}$  on the pSi electrode (eq 11). Hybridization happens after addition of complimentary DNA, and the guanine residues on the complimentary DNA then reduces  $\text{Ru}(\text{bpy})_3^{3+}$  to regenerate  $\text{Ru}(\text{bpy})_3^{2+}$  (eq 12). At a given  $\text{Ru}(\text{bpy})_3^{2+}$  concentration, the increase in the current is thus proportional to the concentration of guanine residues (and thus the concentration of target DNA). Oxidized pSi (p-type, 0.008-0.01 $\Omega$ ) was modified with 3-glycidoxypropyltrimethoxysilane to covalently immobilize DNA onto the pSi surface. In order to prevent the reaction of  $\text{Ru}(\text{bpy})_3^{+2}$  with the guanine residues of probe DNA, guanine is replaced from the probe DNA with a sequence of inosine. DNA (probe)modified pSi electrode was used as a working electrode, Ag/AgCl as the reference electrode, platinum wire as the counter electrode and  $\text{Ru}(\text{bpy})_3^{+2}$  was mixed into the electrolyte solution. When a known concentration of complimentary DNA sequence was exposed to the working electrode, DNA on the working electrode undergoes hybridization with complementary DNA. As a result increased current is observed because of electron transfer from guanines of hybridized DNA strand to  $\text{Ru}(\text{bpy})_3^{+2}$ .



Massad-Ivanir *et al.* developed a label free biosensor for rapid and selective detection of *E. coli* from the food industry process water.<sup>93</sup> The biosensor is based on a nanostructured, pSi Fabry-Pérot thin film. When white light is shined on pSi films, an optical interference pattern arises from the constructive and destructive interference of light from the porous layer. They used this property of oxidized porous silicon (pSi) thin films to detect bacteria of interest. pSi

was functionalized with specific antibodies against *E. coli*. Fig.12 shows the IgG-modified pSi scheme. When the biosensor (IgG-modified pSi film) was exposed to a water sample (Fig. 12 b) the change in spectral reflectivity was collected. When *E. coli* binds to the pSi biosensor films they observed a decrease in the amplitude (intensity) of the reflected light (Fig. 12c) due to the change in optical interference. The biosensor demonstrated a measured LOD of  $10^3$  cells/mL with a total assay time of 45 minutes.

The authors showed use of this optical biosensor for sensing *E. coli* in real time processed food industry water without any pre enrichment or prior treatments with a low detection limits. The lack of onsite and real time detection of currently available biochemical kits, ELISA (enzyme linked immunosorbent assay) and PCR (polymerase chain reaction) can be achieved by rapid and selective detection of these portable biosensors.

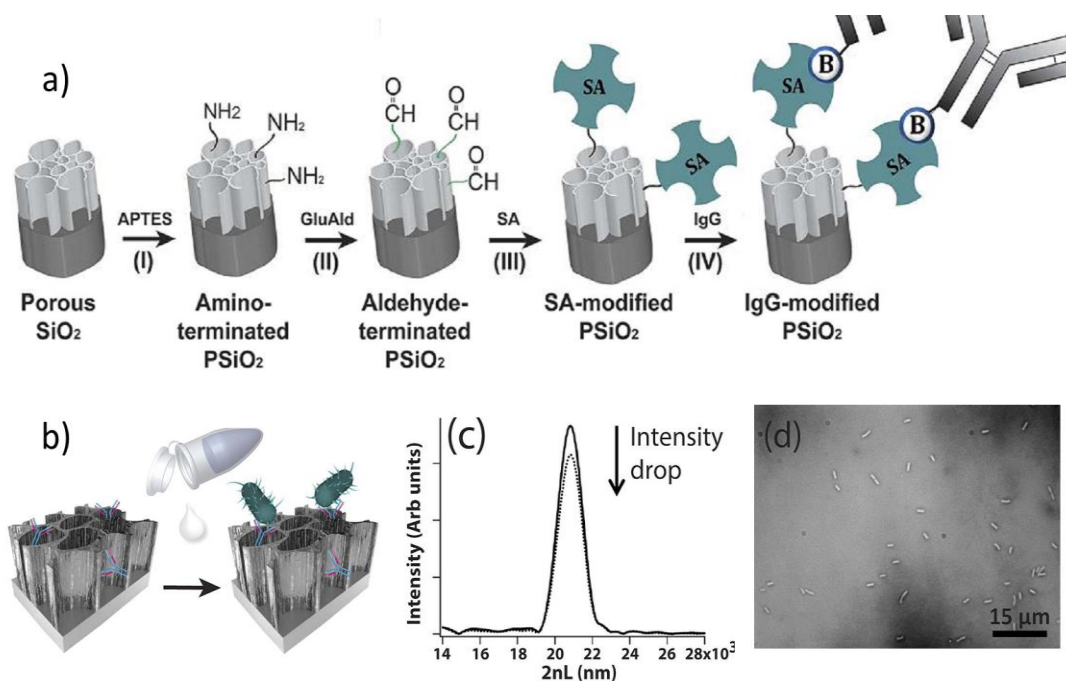


**Figure 12.** a) pSi immobilization with *E. coli* antibody on streptavidin functionalized pSiO<sub>2</sub> b) antibody -antigen interactions upon adding water samples c) decreased amplitude (intensity) of the FFT peak of the porous film d) optical microscopy images of cells captured onto the biosensor. Adapted from ref 93.

### 1.4.3. pSi in tissue engineering

Over the past few years substantial studies have been reported on pure pSi scaffolds and pSi/ polymer composites as cell growth supporting materials,<sup>94</sup> transplantable scaffolds (eg: bone and eye),<sup>95,96</sup> and drugs reservoirs.<sup>97</sup> Some of the early studies on bone tissue engineering were presented here.

The bioactivity of microporous silicon was first studied by Canham *et al.*<sup>55</sup> They showed that porous films were shown to induce hydroxyapatite ( $\text{Ca}_{10}(\text{PO}_4)_6(\text{OH})_2$ , Ca/P ~1.67) growth for days to weeks. The slow degradation of pSi films to  $\text{Si}(\text{OH})_4$  has been shown to stimulate calcification with a negligible inflammatory response *in vivo*.<sup>55</sup> Also silicic acid has been shown to promote the differentiation in human osteoblastic cells *in vitro*.<sup>98</sup> These investigations led pSi to be investigated as a promising biomaterial for bone tissue engineering.

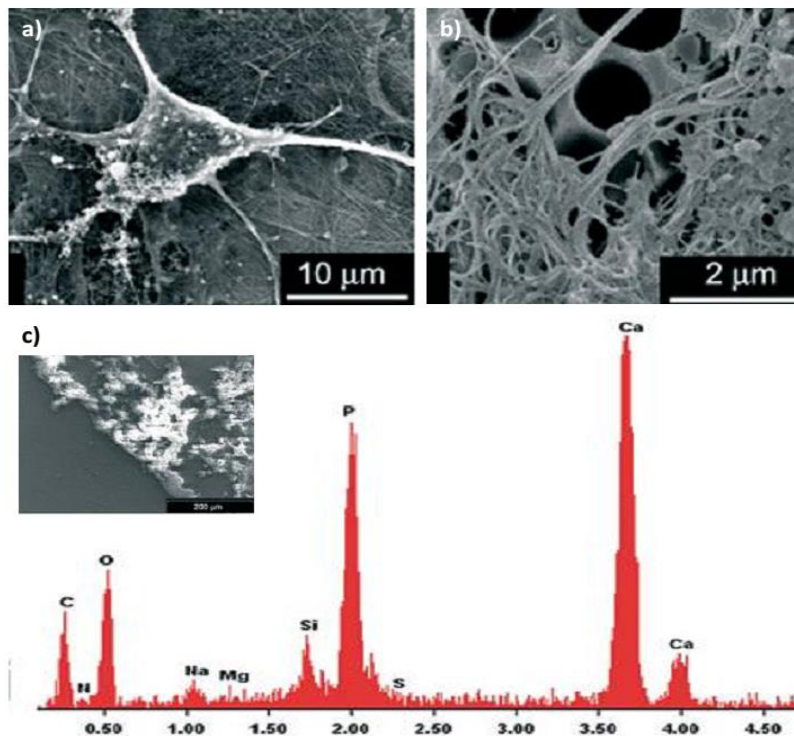


**Figure 13.** a) Osteoblast adhesion on macroporous Si, b) formation of collagen 1 fibrous matrix on macroporous silicon, c) formation of bone apatite like material confirmed by EDX. Adapted from ref 99.

Several groups targeted the use of pure pSi and pSi/polymer scaffolds for bone tissue engineering. Sun *et al.* studied osteoconductivity of pSi samples with three different pore sizes < 15 nm, 50 nm, and 1  $\mu\text{m}$ .<sup>99</sup> They observed macroporous Si (pore size > 1  $\mu\text{m}$ ) displays promising osteoconductivity with better osteoblast adhesion, metabolic activity, protein synthesis, and mineralization compared to mesoporous Si. In this study the authors observed that the degradation of macroporous Si chips were very slow compared to mesoporous Si chips.

High resolution SEM images (Fig 13a, 13b) show the presence of a fibrous mesh, attributed to collagen type 1, which is a major bone protein matrix. The extra cellular matrix (ECM) layer deposited by the osteoblasts on macro pSi shows formation of apatite like material with a Ca/P of 1.72 (Fig.13c, EDX).

A few early studies on pSi/PCL composites as bone tissue engineering materials were based on orthopaedic implant materials and devices comprising porous and or polycrystalline silicon by Anston *et al.*<sup>99</sup> and *in vitro* calcification behavior, and fibroblast viability, proliferation in the presence of pSi (1-5% by mass) and porous PCL sponge composites by Coffey *et al.*<sup>100</sup>

## 1.5. Summary

An overview of fabrication methods to create pSi structures, preliminary studies on biodegradable and biocompatible nature of pSi, along with some of the key advances on pSi as biomaterial for variety of applications (drug delivery, biosensing and tissue engineering) were discussed in this chapter. Subsequent chapters will focus on a new alternative eco-friendly route to the fabrication of pSi nanostructures from silicon accumulator plants for drug delivery applications.

## **Chapter II**

### **Fabrication of Plant Derived Porous Silicon Powders from *Bambuseae* and *Equisetum telmateia***

## 2.1. Introduction

In Chapter I, an overview of currently-available methods for pSi fabrication was presented. Among those methods, the most conventional for preparing mesoporous silicon particles are anodization of silicon wafers, followed by metal-assisted etching. These established techniques require elemental crystalline silicon feedstocks, and the use of corrosive hydrofluoric acid (HF) and organic solvents. Rather than employing these methods that use corrosive reagents and expensive Si starting materials, we are investigating the eco-friendly alternative of producing pSi from silicon accumulator plants/agriculture waste. Multiple plants typically absorb bio-available silicon in the form of organic silicates such as orthosilicic acid ( $\text{Si}(\text{OH})_4$ ) which helps the growth and stability of skeletal structure of these plants along with increased resistance to disease.<sup>101,102</sup> Some of the well-known classes of silicon accumulator plants are horsetail (*Equisetum*), rice (*Oryza*), and bamboo (*Bambuseae*). Among these plants tabasheer, a component of the nodal joints of the bamboo plant, has a relatively high content of silica (90% ash content) compared to other two silicon accumulator plants which contain about 25% silica (ash content).<sup>103,104</sup>

In this Chapter, the use of tabasheer as a cost effective feedstock to create high surface area pSi powders by using magnesiothermic reduction is described. Using this eco-friendly and cost-effective method, we have compared the structure and composition of pSi particles derived from the bamboo component tabasheer, along with the wild grass horsetail. The preparation of porous silicon from silicon accumulator plants includes the following steps: purification of raw material, extraction of silica, reducing silica to silicon and final purification method to remove soluble impurities. The purified product was characterized by a combination of scanning electron microscopy (SEM), energy dispersive X-ray analysis (EDX), transmission electron microscopy (TEM) X-ray diffraction (XRD), Raman spectroscopy, Fourier-transform infrared spectroscopy

(FT-IR) and low temperature nitrogen gas adsorption measurements. In addition to fabrication and characterization of pSi powders, *in vitro* dissolution behavior of these biogenic pSi powders was studied.

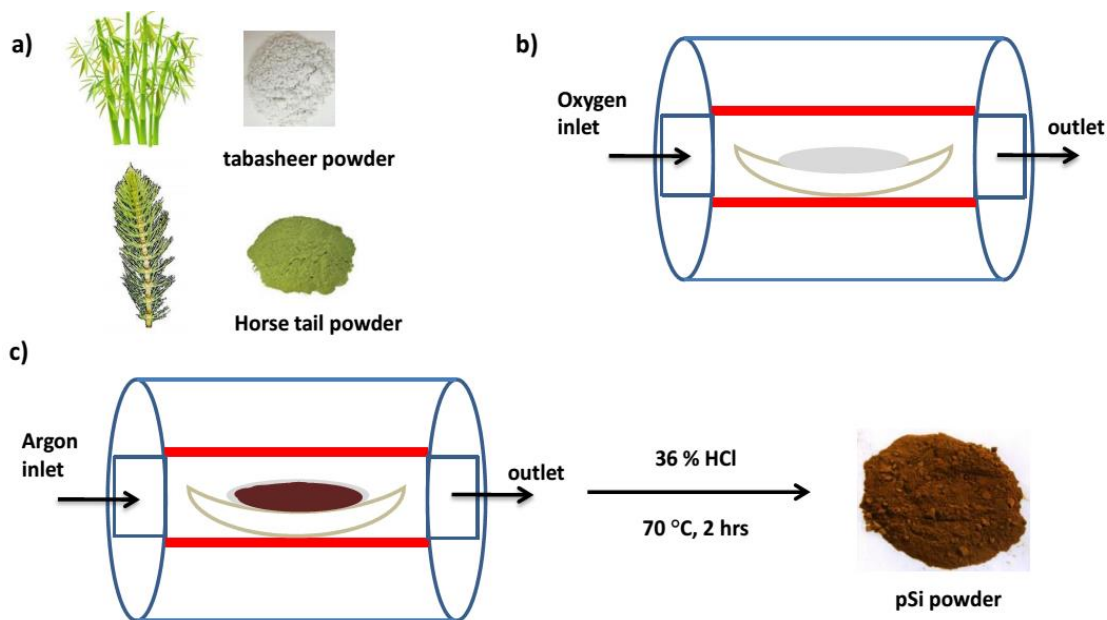


**Figure 14.** Eco-friendly fabrication route for deriving pSi from silicon accumulator plants. a) Optical image of ground tabasheer and horsetail powders, b) calcination of ground powders in a tube furnace, c) magnesiothermic reaction of calcinated powders, and pure pSi powder obtained after washing with 36% HCl.

## 2.2. Experimental

### 2.2.1. Purification of raw ground powders

Tabasheer powder was obtained from Bristol Botanicals Ltd. (ground commercially-available pieces using a ball mill). *Equisetum telmateia* branches were harvested in 2012, Malvern, England. Dried plant fronds of *Equisetum telmateia* (2 g) were coarsely ground to reduce the size to  $\sim 100 \mu\text{m}$ . In atypical experiment 0.5 g of raw ground powder was suspended in 30 mL of 10% hydrochloric acid. The solution was stirred constantly at 100 °C for 2 h,

replenishing the hydrochloric acid every 30 min. After 2h of heating, the product was washed with D.I water, filtered and vacuum dried overnight.

### **2.2.2. Extracting silica from silicon accumulator plants**

The above HCl washed powder (0.5 g) was loaded in a quartz boat (1.5x10 cm) and calcinated at 500°C in the presence of O<sub>2</sub> for 2 h in a tube furnace.

### **2.2.3. Magnesiothermic reduction**

Silica (0.5 g) extracted from a given plant was subsequently converted to elemental silicon by simple reduction using magnesium powder (purchased from General Chemical Division) in the molar ratio of 1:2 (SiO<sub>2</sub>: Mg). Sodium chloride (purchased from Sigma Aldrich) was added to the above reaction mixture in the ratio of 1:1 by weight. Then this mixture was transferred to a quartz boat and heated at a set point of 600 °C for 2 h in the presence of argon in a tube furnace.

### **2.2.4. Purification of magnesiothermic reduction reaction products**

After reduction, the residual magnesium phases were removed by heating the reduced sample with 37 % HCl at 70 °C for 1 h. The final product was washed with D.I water and dried in a vacuum oven.

### **2.2.5. Measuring the oxide content**

The silicon oxide content of Mg reduced pSi powders was estimated by etching pSi powders (500 mg) at room temperature for 10 min with 40% HF. After etching, pSi powders were washed with ethanol (2x50 mL) and dried in a vacuum oven at 50 °C for 1 h, followed by vacuum drying overnight at room temperature. The percent silicon oxide content was calculated by a simple gravimetric analysis of pSi samples after etching.



### 2.2.6. Silicon dissolution assay

To measure the extent of pSi powder (tabasheer derived,  $25 \pm 15 \mu\text{m}$  size) dissolution, a silicomolybdic acid spectrophotometric method was utilized. Three kinds of samples were measured for a total of 8 weeks. The dissolution profiles of as prepared pSi were compared with that of thermally-oxidized pSi and potassium hydroxide (KOH) etched pSi powders. pSi powders were thermally oxidized at  $700 \text{ }^\circ\text{C}$  for 15 min in oxygen. Before etching with KOH (10%) for 40 min all the pSi samples were oxidized at  $700 \text{ }^\circ\text{C}$  for 15 min in oxygen. All samples (3 mg each) were suspended in 0.9% NaCl, placed in an incubator ( $37 \text{ }^\circ\text{C}$ ), with continuous agitation, by replacing NaCl for every week.<sup>105</sup>

In a typical assay, 1 mL of the sample from a given time point is mixed with 4 ml of D.I water, followed by addition of 1 ml of HCl (aq.) (0.25 M) and 1 ml of ammonium molybdate (5%). The solution mixture was stirred for one minute and 10 minutes later a yellow color complex developed. Then 2 ml of sodium sulfite (17% w/v) was added to this mixture followed by vigorous stirring for 1 min. Finally the solution was allowed to stand for 1 hr. Before measuring the absorbance 1 mL reagent grade EDTA (1%) was added. The concentration of silicic acid bound to the molybdate species is monitored by the value of its absorbance at 725 nm using a UV-Vis spectrophotometer. A standard curve was generated from a series of silica standards. The stock solution was prepared by dissolving 17.65g of the stable  $\text{Na}_2\text{SiO}_3 \cdot 5\text{H}_2\text{O}$  compound in 1 L of water and further diluted to give final concentration of  $0.05 \text{ mg/mL SiO}_2$ .

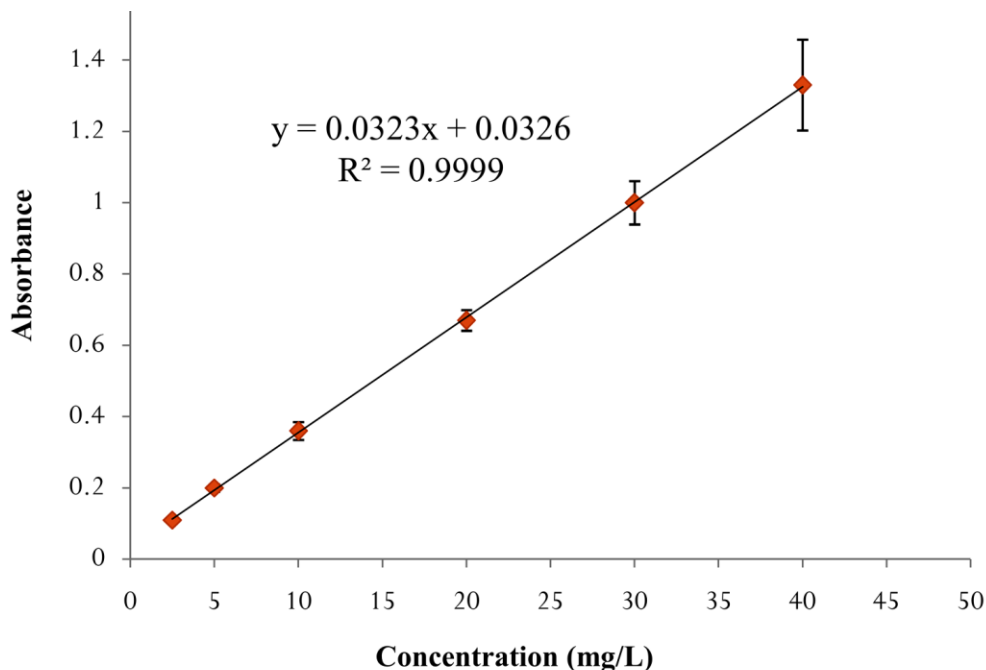


**Figure 15.** Standard curve developed by ammonium molybdate assay using standard silica samples, absorbance measured at  $\lambda_{\max}$  725 nm.

### 2.2.7. Instrumentation

The size and morphology of the pSi nanoparticles were investigated by field emission scanning electron microscopy (FE-SEM) using a JEOL JSM 7100. Elemental analysis was done by using pSi micro particles by electron dispersive X-ray analysis (EDX). TEM analysis was conducted with a JEOL TEM 2100 operating at 200 kV. X-ray diffraction was carried out using a Phillips 3100 X-ray powder diffractometer with Cu K $\alpha$  radiation operating at 35 kV. Raman spectrometric analysis was performed using a DeltaNu System with a 785 nm laser source. For FT-IR studies samples were prepared in the form of KBr pellets (1% w/w sample concentration) and analyzed using a MIDAC M4000 series spectrometer. Gas adsorption/desorption analysis was carried out by Dr. Armando Loni of pSiMedica Ltd. A Beckman DU-64 spectrophotometer was used for measuring absorbance for dissoluble silica assays.

## 2.3. Results and Discussion

### 2.3.1. Fabrication method

The individual steps of this eco-friendly fabrication route are summarized in Fig 14. An initial washing process of the ground plant powder with dilute hydrochloric acid (10%) allowed the removal of any metallic residues possibly deposited during the plant grinding process. EDX analysis of ground horsetail powder before and after HCl wash is shown in Fig.16 and Fig. 17. This data suggests that this acidic wash readily removes a trace amount of KCl deposited on the plant material. The dried powder was then calcinated in the presence of oxygen to extract biogenic silica from the purified raw plant powder. This process is essential in conversion of all the organic silicates into the form of pure silica. Silica extracted from a given plant is subsequently converted to elemental silicon by simple reduction with magnesium at a temperature of 600 °C in Ar. Magnesiothermic reduction was done using silica and Mg powder in a molar ratio of 1:2 (SiO<sub>2</sub>: Mg).

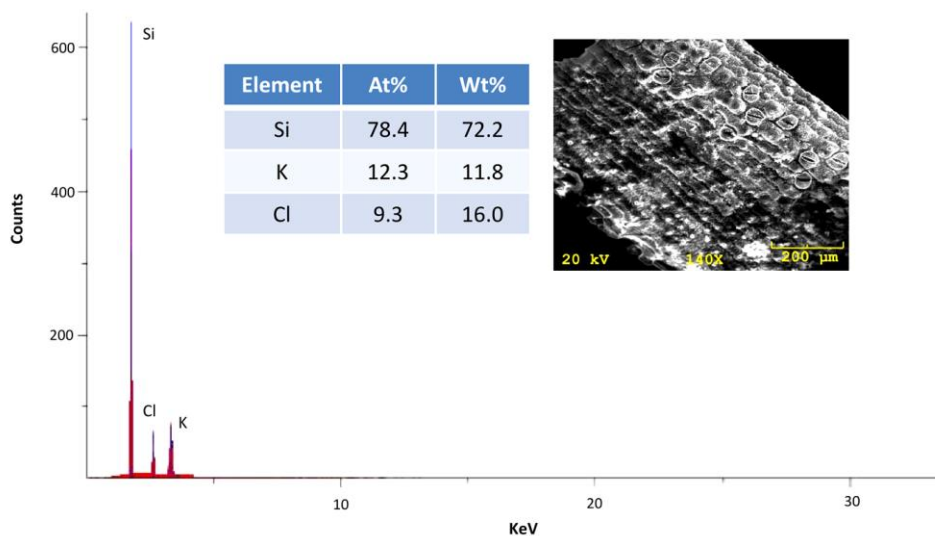


**Figure 16.** SEM-EDX analysis on *E. telmateia* before HCl wash, inset shows the SEM image of a particle from ground powder.

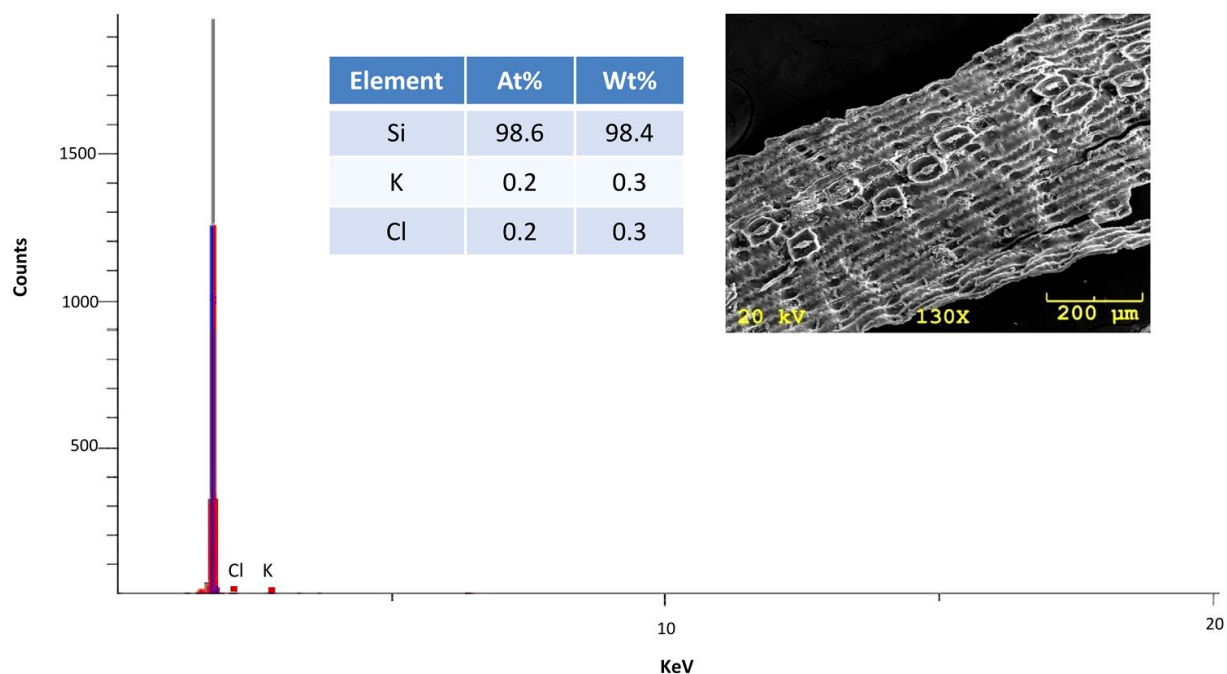


**Figure 17.** SEM-EDX analysis on *E. telmateia* after HCl wash; inset shows the SEM image of a particle from ground powder.

As discussed in Chapter 1, the highly exothermic nature of this reaction between silica and magnesium was controlled by adding sodium chloride as a thermal moderator, as well as to maintain porosity.<sup>49,50</sup> The soluble magnesium oxide phases were washed with hydrochloric acid (37%) at 70°C for 2h.

### 2.3.2. Characterization of pSi powders

Scanning electron microscopic analysis of a typical reaction product from magnesiothermic reduction shows a wide distribution of particle sizes in case of tabasheer and horsetail (*E. telmateia*) with a mean particle diameter of  $24 \pm 15 \mu\text{m}$  and  $76 \pm 32 \mu\text{m}$  respectively. Size of the silica particles before the reduction is tabasheer is  $22 \pm 18 \mu\text{m}$  and horsetail is  $85 \pm 35 \mu\text{m}$ . The biogenic silica from tabasheer and *E. telmateia* fronds retained their shape and size during the reduction process. This was confirmed by SEM analysis of porous silica before and after magnesiothermic reduction (Fig. 18). Some of the SEM images shown here were pSi

powders (derived from *E. telmateia* fronds) prepared by an undergraduate student working in our lab, Sabrie Howell.

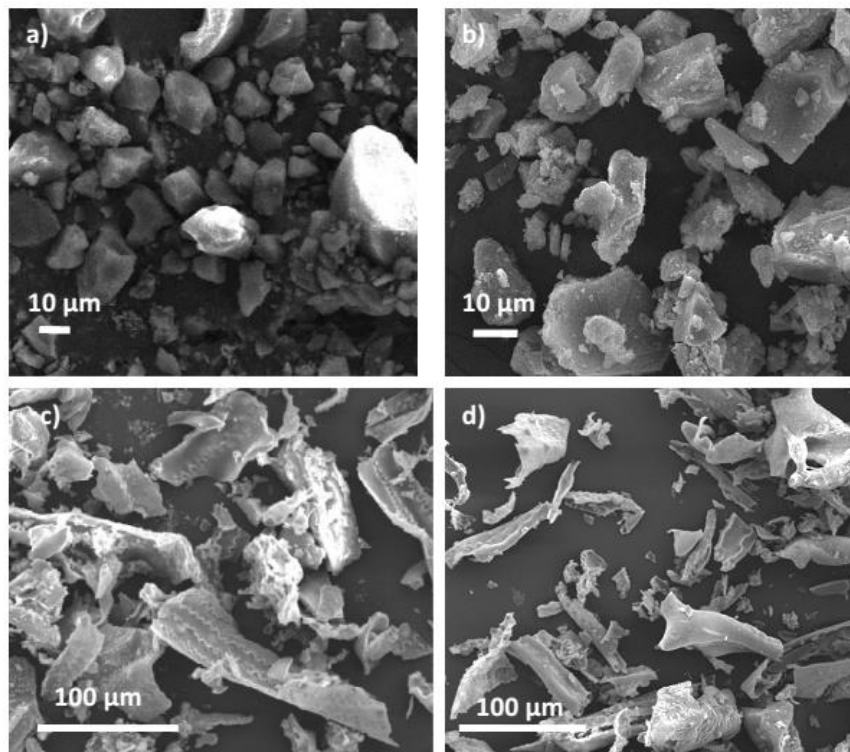


**Figure 18.** SEM images of a) pSiO<sub>2</sub> derived from tabasheer powder, b) pSi derived from tabasheer powder, c) pSiO<sub>2</sub> extracted from horsetail (*E. telmateia*) powder, d) pSi derived from *E. telmateia* fronds.

Individual pores observed in the high resolution SEM image (Fig. 19) confirm the presence of pores in the range of 50-100 nm in diameter in case of both tabasheer and horsetail derived pSi powders. Pore morphology derived from these individual plants was distinct and associated pore morphology was influenced by sub organelles of the leaf and nodes/joints.<sup>106</sup> From the EDX analysis shown in Fig. 20 and 21, it is evident that the final product obtained from magnesiothermic reduction reaction is ~99% pure with no measurable traces of magnesium. The eco-friendly magnesiothermic reduction reaction yielded ~70% conversion of silica/silicon derived from tabasheer and in case of horsetail, ~60%.

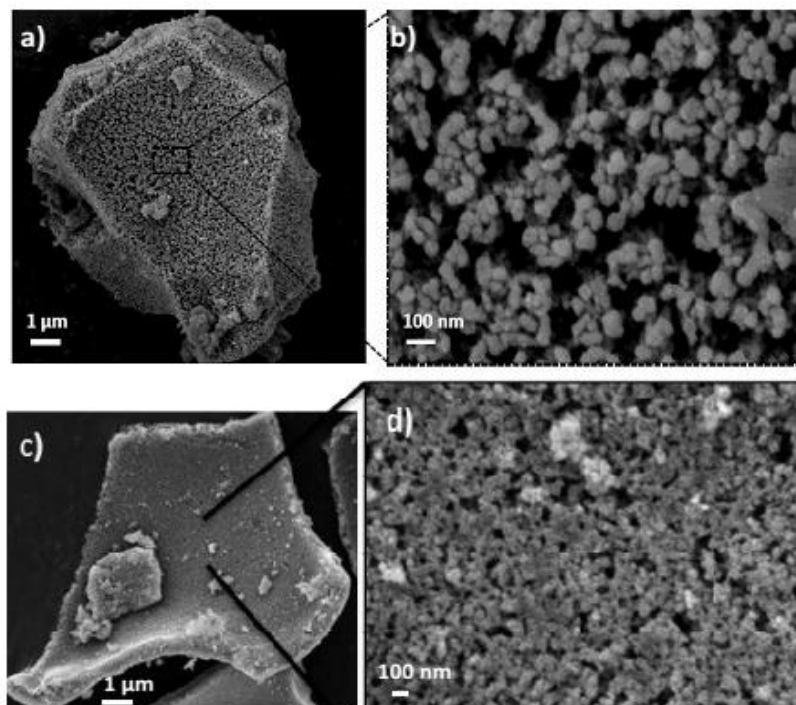


**Figure 19.** SEM images of: a) Free standing pSi particle derived from tabasheer, b) individual nanopores along the pSi particle surface (tabasheer), c) image of pSi particle derived from horsetail, d) individual nanopores along the pSi particle surface (*E. telmateia*).

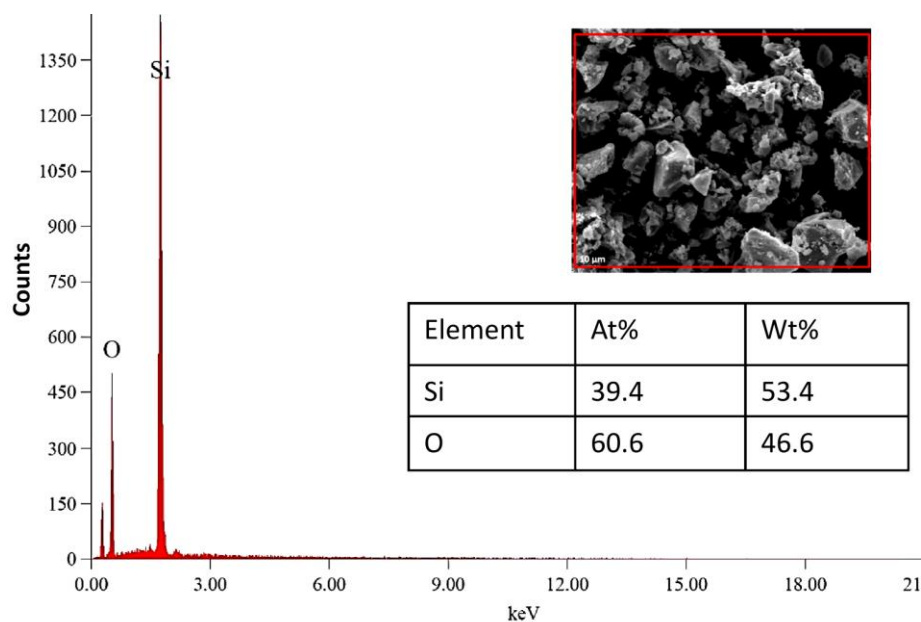


**Figure 20.** SEM-EDX analysis on pSi derived from tabasheer.

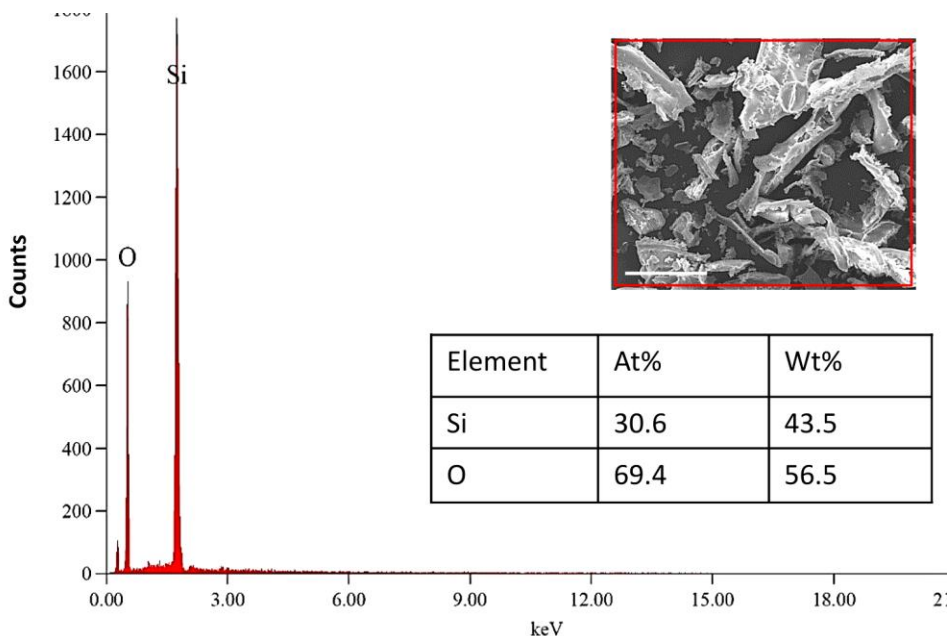


**Figure 21.** SEM-EDX analysis on pSi derived from horsetail.

pSi microparticle morphology from tabasheer and horsetail was further observed by transmission electron microscopy (TEM). The following details are observed in both cases of pSi samples. These particles are comprised of an aggregate of small nanoparticles, as gauged by the transmission electron microscopy images (Fig. 22a and Fig 23a). High resolution transmission electron microscopy (HRTEM) analysis reflected the nanostructure features of pSi, where small crystalline domains of silicon (4-8 nm) are embedded within the amorphous oxide matrix (Fig. 22b and Fig. 23b). A lattice spacing distance of 0.310 nm associated with the Si (111) plane is clearly evident from Fig. 22c and Fig. 23c. Inset 22c and 23 c, shows FFT (fast fourier transform) diffraction pattern and it is consistent with a polycrystalline orientation.

Along with the HRTEM analysis, the presence of crystalline silicon is evident from X-ray diffraction (XRD) and Raman spectroscopy. The XRD spectra shown in Fig. 24 and 25 correspond to tabasheer derived and horsetail derived pSi powders, respectively. This pattern

confirms the formation of highly crystalline porous silicon, with peaks at  $2\theta = 28^\circ$ ,  $47^\circ$ , and  $56^\circ$  ascribed to reflections of (111), (220), and (311) respectively.<sup>107</sup> Raman spectroscopy displayed the presence of characteristic crystalline Si phonon at  $521\text{ cm}^{-1}$  in both cases (Fig. 26).<sup>108</sup>

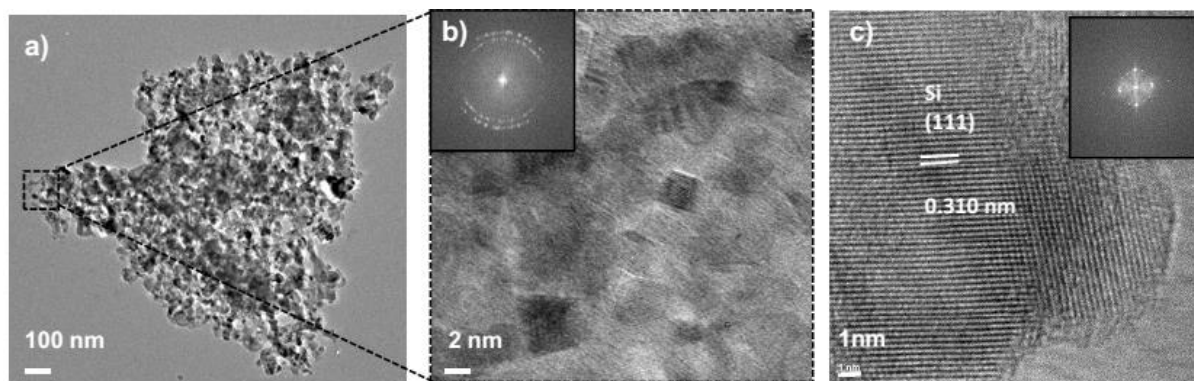


**Figure 22.** TEM images of tabasheer derived pSi a) low magnification image of free standing pSi microparticle, b) high resolution TEM image with a small silicon crystalline domains, inset shows FFT diffraction pattern, c) high resolution TEM lattice imaging, inset shows diffraction pattern on of silicon nanocrystallite.

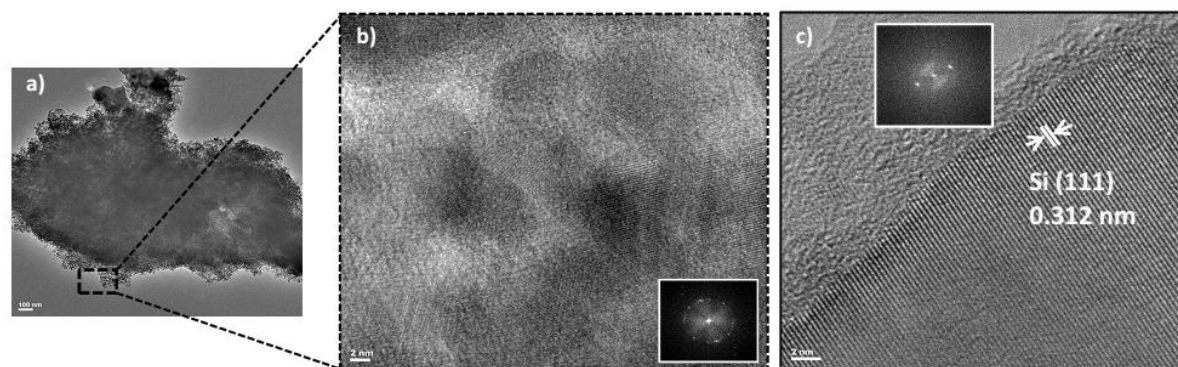


**Figure 23.** TEM images of pSi derived fronds of *Equisetum telmateia*. a) Low magnification image of free standing pSi particle and b) high resolution TEM images (scale bar of (a) = 100 nm; (b) = 2 nm), inset shows FFT diffraction pattern. c) TEM lattice imaging, inset shows diffraction pattern on of silicon nanocrystallite.



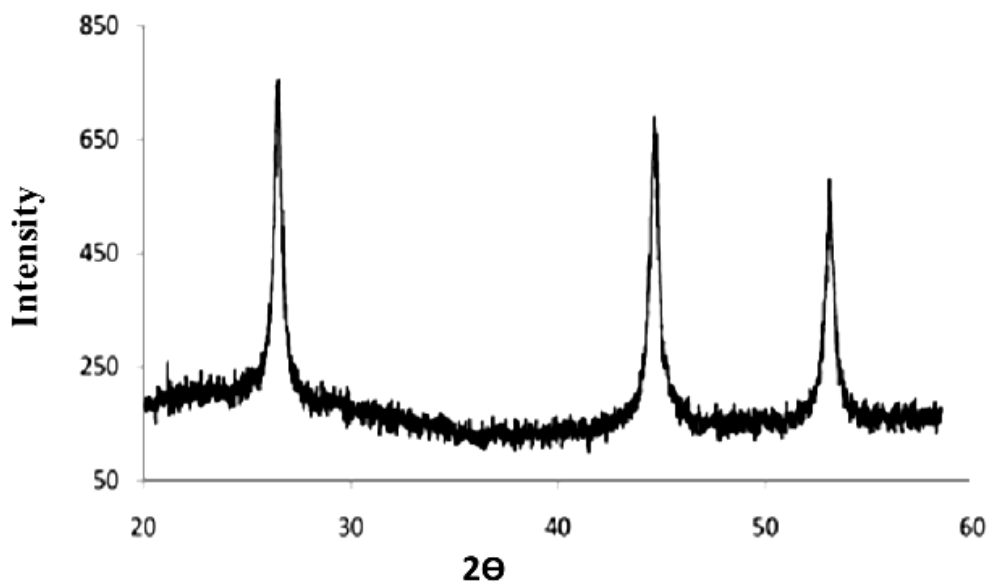


**Figure 24.** X-ray diffraction pattern of porous silicon derived from tabasheer.

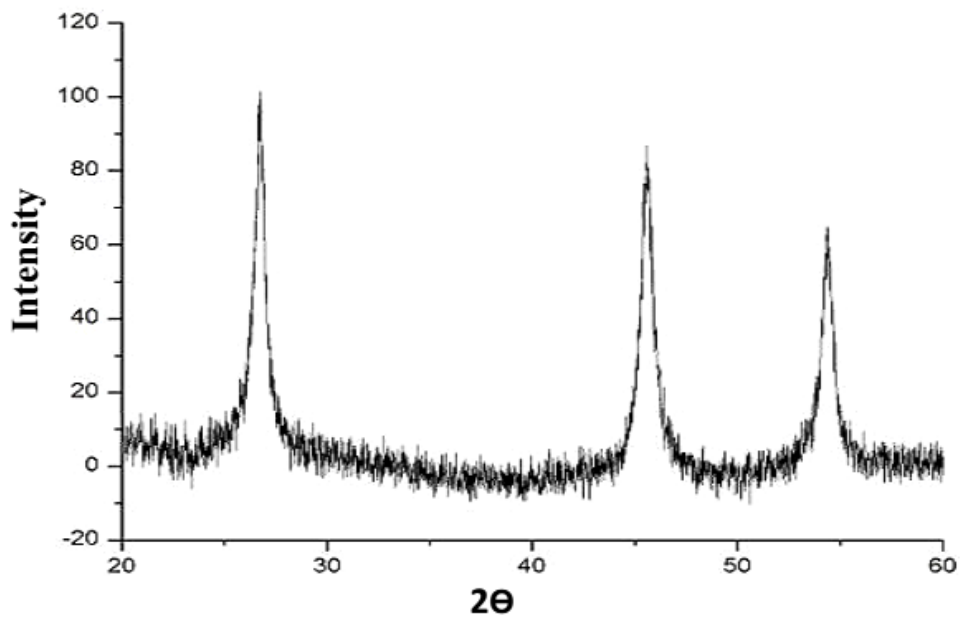


**Figure 25.** X-ray diffraction pattern of porous silicon derived from horsetail.

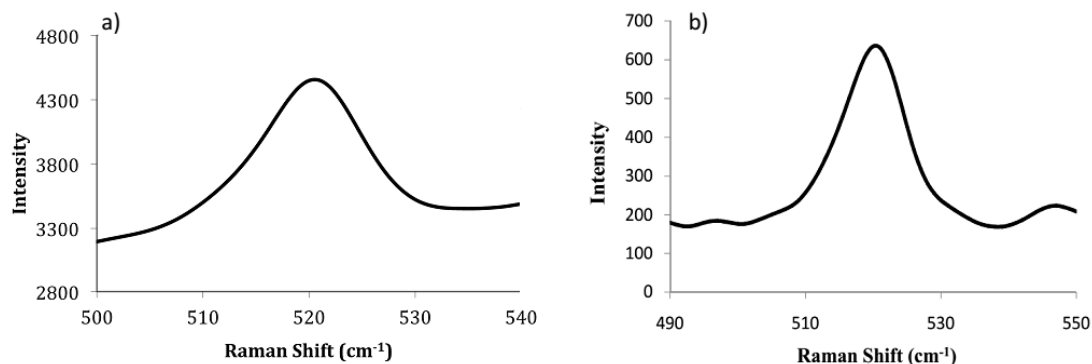


**Figure 26.** Raman spectrum of porous silicon derived from a) tabasheer, b) *E. telmateia* fronds.

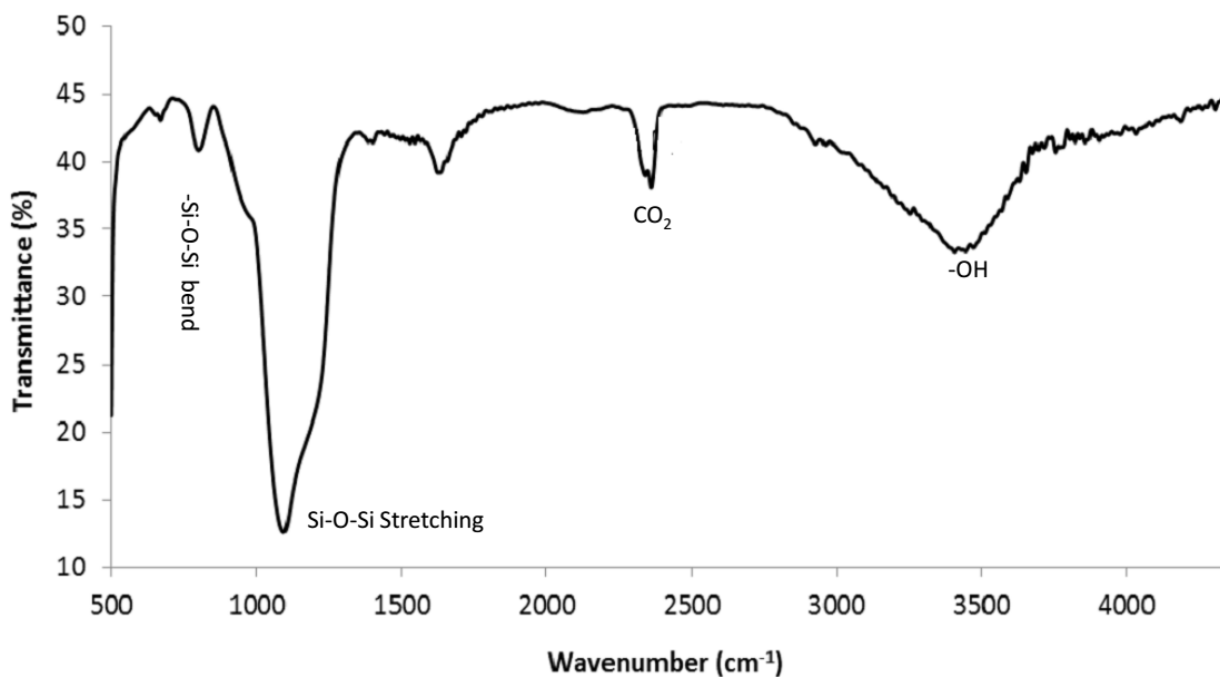


**Figure 27.** FTIR spectrum of porous silicon derived from tabasheer.

The oxide content estimated by etching with hydrofluoric acid (which dissolves the  $\text{SiO}_2$  and yields Si), and the gravimetric analysis suggested that there is ~75% of silicon oxide content in case of tabasheer. The presence of a  $\nu(\text{Si-O-Si})$  stretching vibration at  $1087 \text{ cm}^{-1}$  (FT IR, Fig. 27) is consistent with significant oxide content in the matrix. Based on the assumption of

uniform cylindrical mesopores are present within the porous structure, specific surface area and pore size of the mesoporous silicon were determined by employing nitrogen-sorption analysis (Brunauer–Emmett–Teller (BET) at 77 K. BET measurements were carried out by a collaborator, Dr. Armando Loni of pSiMedica Ltd., UK. pSi derived from magnesium reduced tabasheer has a surface area of 178 m<sup>2</sup>/g, a pore volume of ~ 0.5 ml/g, and pore diameter of 11 nm. Fig. 28 shows the average pore diameter of tabasheer powder before calcination and after reduction. The decrease in the pore volume accompanied by increase in the pore size distribution was observed after magnesiothermic reduction. This behavior is attributed to slight pore collapse during the magnesiothermic reduction. Because of the exothermic nature of the reduction, heat produced by this reaction partially collapsed the pores which resulted in reduced pore volume.

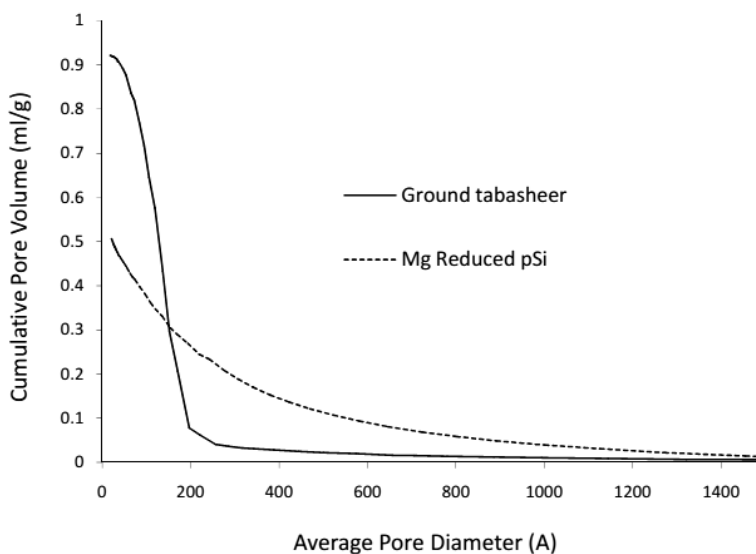


**Figure 28.** Brunauer–Emmett–Teller (BET) analysis on pSi derived from tabasheer.

### 2.3.3. *In vitro* dissolution studies of pSi particles

One of the important requirements of drug delivery carrier is its efficient clearance from body or biodegradation into benign compounds. Dissolution of porous silicon can be described by the following two step process. The first step is oxidation of porous silicon followed by

complete hydrolysis of the oxide that generates orthosilicic acid, biologically benign compound that can be excreted by kidneys.



Kinetics of the dissolution of pSi into orthosilicic acid depends on various physicochemical parameters: degree of crystallinity, size of crystalline domains, porosity, surface area, pore wall surface chemistry and pore size etc.<sup>109</sup> Some examples of dissolution profiles of anodized pSi and change in dissolution with porosity, pore size and surface chemistry were discussed in Chapter 1. Shabir *et al.* reported complete degradation of amorphous hydrogenated silicon colloids of low surface area (<5 m<sup>2</sup>/g) within 10–15 days at 37°C. Solubility was dramatically reduced after conversion of amorphous hydrogenated silicon colloids to polycrystalline silicon (grain size 30 nm).<sup>110</sup> Depending upon the biomedical application the biodegradability profiles of pSi can be tuned from hours to months.<sup>111-113</sup>

In order to understand the biodegradation behavior of plant derived pSi powders, *in vitro* dissolution behavior of as prepared, thermally oxidized, and thermally oxidized followed by KOH etched pSi powders were quantified by molybdenum blue-based assay. KOH is a well known anisotropic etchant that preferentially attacks Si (100) plane and the plane is etched at a 54.7° angle relative to the Si (111) plane.<sup>114</sup> To prevent the KOH from etching the porous features of Si powders, pSi powders were thermally oxidized to form a thin oxide passive layer around the pore walls. Degradation behavior of thermally oxidized and chemically oxidized (KOH etch) samples were compared to as prepared pSi to see whether the deliberate oxidation of pSi skeleton slows down the degradation behavior. The degradation behavior (8 weeks) of these

plant-derived pSi samples is shown in Fig. 29. The cumulative dissolution profile shows that as-prepared pSi dissolves faster than the thermally-oxidized and KOH-etched samples. After 8 weeks, 50% of the as prepared pSi was dissolved, whereas thermally oxidized and KOH etched samples have similar dissolution profiles with 28%, and 33% dissolution, respectively. In the case of thermally oxidized (700 °C) porous silicon, the passive oxide layer formed on the pore walls minimizes the exposure of silicon present on pore walls to the surrounding medium, which reduces the dissolution behavior of porous silicon. In the case of KOH-etched pSi samples, Si oxidizes in presence of hydroxide ions and oxidation further reduces dissolution of silicon.

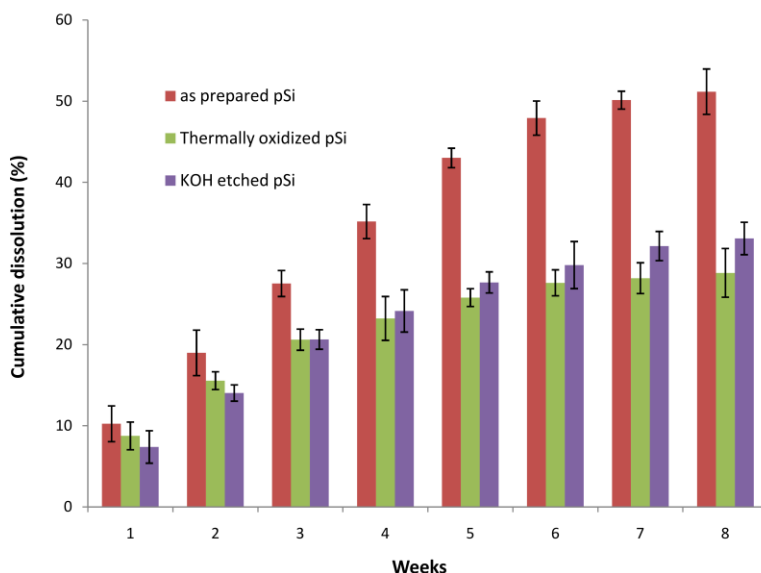


**Figure 29.** Dissolution studies (up to 8 weeks) on pSi samples in 0.9% NaCl solution.

**Table 1.** BET analysis on pSi samples (tabasheer derived) used for dissolution studies.

Sample	Surface area m <sup>2</sup> /g	Pore Volume ml/g	Pore Diameter Å
Tabasheer derived pSi	180	0.56	123
Thermally oxidized pSi(tabasheer)	99	0.39	155
Thermally oxidized followed by KOH(10%) etched pSi	36	0.26	290

According to BET analysis, as-prepared tabasheer-derived pSi has a relatively higher surface area compared to thermally oxidized and KOH etched pSi samples. In case of thermally oxidized and chemically oxidized pSi, this decrease in surface area and pore volume can be attributed to partial sintering and oxidation of silicon during these processing steps.<sup>77,115</sup>

#### **2.4. Summary**

We have shown that *Bambuseae* (tabasheer) and *E. telmateia* are excellent sources for cost effective eco-friendly magnesiothermic reduction of silica to silicon. The reduction process resulted in 70% conversion of silica to silicon in case of tabasheer, and 60% in case of horsetail with a purity of ~99% (no measurable magnesium silicate phases). Careful characterization of the material showed that the silicon derived from these plants was highly crystalline, with relatively high surface areas. By taking advantage of its nanopore morphology, and high surface areas we have studied the application of these pSi powders in delivery applications (discussed in next chapters). Preliminary studies on biodegradation of tabasheer derived pSi showed 50% degradation within 8 weeks. Additional studies are likely required using a more sensitive analytical method (eg. inductively coupled plasma atomic emission spectroscopy (ICP-AES) to determine the dissolution profiles more accurately. Ideally, the dissolution rate of these oxidized pSi powders can be tuned by different etching chemistries to provide a broader range of degradation rates *in vitro/in vivo*. For example, etching with HF (aq.) reduces the oxide content, thereby increasing the dissolution rate of these oxidized pSi powders.

## **CHAPTER III**

### **Loading and Release of *Bambuseae Arundinacea* Leaf Extract from Tabasheer Derived pSi**

### 3.1. Introduction

In Chapter 2, silicon accumulator plants *Bambusae* and *Equisetum* were shown to be an excellent source of silica for preparing pSi particles of high purity in competitive yields, along with relatively high surface areas. Apart from being an excellent source of silica, the other important feature of silicon accumulator plants (*Bambusae arundinacea* and *Equisetum telmateia*) is that it has been widely reported that the leaves, root, bark or other constituent parts possess therapeutic activities used to alleviate medical ailments because of its phytochemical constituents.<sup>116,117</sup> One example is the tabasheer component of *Bambuseae*, used primarily in herbal treatments as an antipyretic, antispasmodic, and antiparalytic.<sup>118</sup> Pharmacological studies on the different parts of the plants *Bambusae arundinacea* and *Equisetum telmateia* showed that these plants possess a variety of biological activities including antibacterial activity.<sup>119,120</sup> In the case of bamboo (*Bambusae bambose L.*) preliminary studies showed that the ethanolic leaf extracts are active against multi drug resistant (MDR) bacteria.<sup>121</sup>

The use of phytomedicines (drugs extracted from plants) has become an alternative to conventional therapeutics for treatment of infectious diseases.<sup>122</sup> The use of plant derived extracts for antibacterial activity is gaining more interest because of the combination of more than one antibacterial agent present in a single crude extract can provide an intrinsic combination therapy.<sup>123</sup> Taking advantage of these two features (1) excellent source of silica, (2) the presence of the bioactive compounds such as antimicrobial agents, our aim is to develop an eco-friendly drug delivery carrier matrix where the carrier and the drug derives from a single plant source.

This goal is accomplished by fabricating pSi from tabasheer (*Bambuseae*) and horsetail (*Equisetum*) powders (discussed in Chapter 2) and loading with an extract originating from leaves of the same plant. Antibacterial activity of the extract from the *Bambuseae* plant was first



evaluated before loading the extract into the pSi carrier. Extraction of antibacterial agents from the leaf and subsequent loading of antibacterial extracts into plant-derived pSi, evaluation of sustained release of antibacterials from the drug carrier, and identification process of some of the compounds responsible for antibacterial activity are reported herein.

## **3.2. Experimental**

### **3.2.1. Collection of plant material**

The fresh leaves of the plant *Bambusae arundinacea* were collected in June 2013 from Eluru, Andhra Pradesh, India, and examined by Barney L. Lipscomb, systematic botanist from Botanical Research Institute of Texas, Fort Worth, TX, USA. *Equisetum telmateia* stems and fronds were harvested from Malvern, Worcestershire, UK in 2012.

### **3.2.2. Soxhlet extraction**

*Bambusae arundinacea* and *Equisetum telmateia* leaves were shade dried for two days. In the case of *Bambusae arundinacea*, ground powder (10 g) was extracted with ethanol (100 mL) at a temperature of 85-90 °C in a soxhlet extractor. *Equisetum telmateia* ground leaf powder (5 g) was extracted with different solvents, petroleum ether, chloroform, ethanol, and water at a temperature slightly above (5°C) their boiling point for 3 h. After 3 h the extracts were concentrated through the use of a rotary evaporator, and the dry extracts were stored at 4°C for further analysis.

### **3.2.3. Extraction at room temperature**

*Bambusae arundinacea* and *Equisetum telmateia* ground leaf powders (5 g each) were placed in a flask and stirred in 50 mL solvent (chloroform, ethanol, and hexane). After 24 h, the stirred leaf powders were filtered and stirred in the presence of equal volumes of solvent. The process was repeated every 24 h for a period of 72 h. After 3 successive days of extraction all the

extracts were combined and evaporated to dryness in a rotary vacuum and stored at 4 °C until further analysis.

### **3.2.4. Evaluation of antibacterial activity of the leaf extracts**

#### **3.2.4.1. Test microorganisms**

The antimicrobial activity of the plant extracts were tested against bacterial strains purchased from American Type Culture Collection, Maryland, USA: Gram-positive: *Staphylococcus aureus* (ATCC 25923), gram-negative *Escherichia coli* (ATCC 25922), and fungal strain *Candida albicans* (ATCC 10231).

#### **3.2.4.2. Disc diffusion assay**

Antibacterial activities of the extracts were tested using a disc diffusion assay. The test solutions were prepared by dissolving known amount of dry plant extract dissolved in 10 % DMSO. Then 60 µL of dry plant extract was placed aseptically on a sterile filter paper disc (diameter 6mm) and transferred to an agar plate already seeded with the bacterial culture ( $10^7$  CFU/ml, 24 h). Discs injected with 60 µL of 10% DMSO were used as a negative control. Then the plates were incubated at 37 °C for 18 h. After the allotted period, the inhibition zones formed were measured with a ruler. All experiments were run in triplicate.

#### **3.2.4.3. Micro broth dilution assay**

In a 15 mL sterile centrifuge tube 0.5 mL of LB medium (2X concentration) was added to 0.5 mL of known amount of the antibacterial compounds (compound **1** and **2**) dissolved in 10% DMSO. To the above mixture 10 µL of overnight microbial culture was added. After 18 h of incubation the optical density of the samples was measured at 600 nm. The blank solution was prepared by adding 0.5 mL of sterile water to 0.5 mL LB medium (2X).

### **3.2.5. Loading of antibacterial leaf extracts into pSi**

Leaf extracts that showed antibacterial activity were loaded into pSi powders. In a typical loading method pSi powder (~10 mg), was soaked with 0.120 g of dried leaf extract dissolved in 1 mL of ethanol for 2 h. Then this mixture was heated at ~65- 70°C for 30 min. The above mixture was centrifuged; supernatant was removed, and washed with sterile water twice and dried under vacuum overnight.

### **3.2.6. Release of antibacterial agents from pSi loaded with crude extract**

pSi powder loaded with leaf extract (20 mg) was suspended in 0.6 mL of sterile D.I water in a 8 mL vial. The vial was continuously rotated (10 rpm) using an agitating apparatus at 37°C. After 24 h of agitation the vial was centrifuged and the supernatant was drawn carefully into a sterile vial. This procedure was repeated after replenishing 0.6 mL sterile D.I water into the vial. A 60 µL fraction of the supernatant was tested for antibacterial activity using disc diffusion assay.

### **3.2.7. Isolation of known antibacterial compounds from *Bambuseae arundinacea***

Dried leaf powder (100 g) was extracted using a soxhlet extractor (described in the previous section) using ethanol as a solvent. Dry extract (3 g) was initially fractionated (Fig. 30) with four following solvents based on their polarity ranging from low to high: petroleum ether (3x10 mL), chloroform (CHCl<sub>3</sub>, 3x10 mL), ethyl acetate (EtOAc, 3x10 mL) and methanol (MeOH, 3x10 mL). These four dried fractions were tested for antibacterial activity by plate diffusion assay (Table 2). All four fractions were monitored with thin layer chromatography (TLC) using a solvent system composed of ethyl acetate and hexane (3:7). Fractions with similar R<sub>f</sub> values (CHCl<sub>3</sub> and EtOAc) were tested for their antibacterial activity and compared to petroleum ether and methanol fractions. The dried combined fractions of CHCl<sub>3</sub> and EtOAc were

subjected to preparative TLC using petroleum ether and chloroform (2:3) as a solvent system, which yielded in five sub fractions (Fig. 31).

Among these five sub fractions, two sub fractions fraction 5, fraction 8, were active against *S. aureus* with inhibition zones of 21 mm, and 22 mm and fraction 9 with an inhibition zone of 11 mm. Highly active Fraction 5 and fraction 8 were further purified by preparative TLC using the solvent systems chloroform: ethyl acetate: acetic acid (4.5:4.5:1) and hexane: ethyl acetate (3:2) respectively. The sub fraction 5 yielded fraction 10 and pure compound **1** and sub fraction 8 to afford fraction 11 and compound **2**.

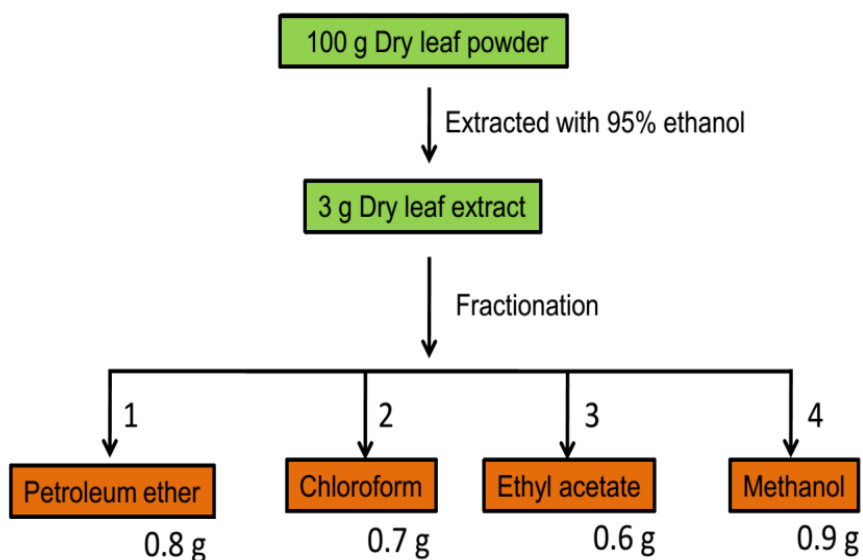


**Figure 30.** Flow chart diagram of initial fractionation of *Babuseae arundinacea* ethanol leaf extract. Fractionation of the leaf extract into solvents (petroleum ether, chloroform, ethyl acetate, and methanol) yielded 0.8, 0.7, 0.6, and 0.9 g of Fr.1, Fr.2, Fr.3, and Fr.4 respectively.

**Table 2.** Antibacterial activity (average inhibition zones) of four fractions Fr.1, Fr.2, Fr.3, and Fr.4 obtained from disc diffusion assay (against *S. aureus*).

Fraction No.	1	2	3	4
Inhibition Zone (mm)	9 ± 2	16 ± 2	17 ± 1	-

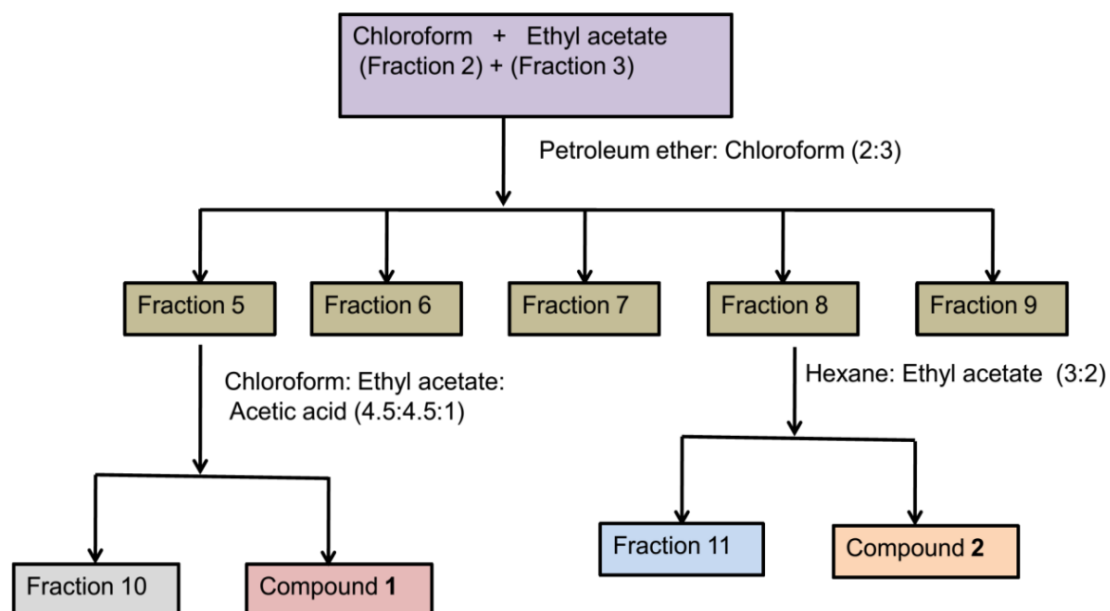


**Figure 31.** Flow chart diagram of separation of phytochemicals from combined fractions of chloroform and ethyl acetate. Chloroform and ethyl acetate fractions were further purified by preparative TLC to give five sub fractions. Active sub fractions (Fr5, and Fr. 8) were purified by TLC to afford pure compounds 1&2.

### 3.2.8. Instrumentation

Thermo-gravimetric analysis (TGA) was performed using a Seiko SII model SSC/5200TGA at a heating rate of 10 °C/min (up to 400 °C) under nitrogen. Mass spectrometry (MS) was performed using an Agilent Technologies 6224 TOF LC/MS system.  $^1\text{H}$  NMR and  $^{13}\text{C}$  NMR were recorded on Bruker Ascend 400, at 400MHz.

## 3.3. Results and Discussion

### 3.3.1. Antibacterial activity of the extract

Soxhlet extraction and room temperature extraction methods were used to extract active components from leaves of *Equisetum telmateia* and *Bambuseae arundinacea*. These extracts were tested for their antibacterial activity against *staphylococcus aureus* (*S. aureus*), *escherichia*

*coli* (*E. coli*) and *candida albicans* (*C. albicans*) using a disc diffusion assay. Leaf extracts of *Equisetum telmateia* (in petroleum ether, chloroform, ethanol, and water) were not active against any of the bacterial and fungal strains evaluated. *Bambuseae arundinacea* leaf extracts prepared by room temperature extraction and soxhlet extraction showed antibacterial activity against *S. aureus* (Table 3).

**Table 3.** Antibacterial activity of leaf extracts from *Bambuseae arundinacea* against *S.aureus*.

<b>Bamboo Leaf Extract</b>	<b>Inhibition Zone (mm)</b>
Chloroform, Soxhlet	14.0 ± 0.8
Ethanol (r.t)	12.0 ± 2.0
Ethanol, Soxhlet	18.0 ± 2.0
Hexane, Soxhlet	16.0 ± 0.8

### 3.3.2. Loading and release of antibacterial leaf extract from pSi particles

Among the extracts listed in Table 3, soxhlet extraction of *Bambuseae* leaves by ethanol showed the highest antibacterial activity. This highly active antibacterial leaf extract of *Bambuseae arundinacea* was loaded into pSi derived from tabasheer by the solution loading method discussed in the experimental section. The dried extract-loaded pSi sample was analyzed by thermo-gravimetric analysis (TGA) to quantify the extent of loading. A typical TGA trace (Fig. 32) showed significant mass loss in the range of 150-400 °C along with a steady weight loss in the temperature range of 0-100 °C due to volatile components and moisture loss (<5%). Between 150-400 °C any weight loss is assumed to be degradation/elimination of active phytochemicals. Total loading capacity measured by TGA analysis is 25% by weight.

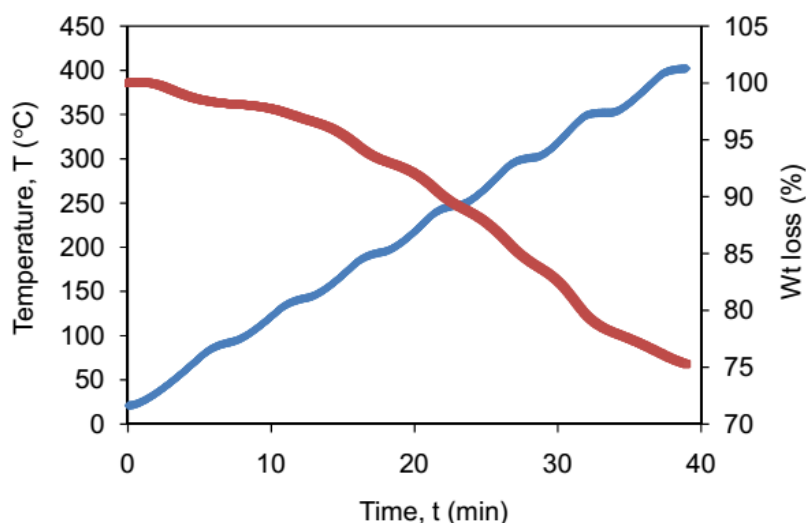


**Figure 32.** Thermogravimetric analysis (TGA) of the extract loaded into pSi. Weight loss curve (in red), heating curve (in blue).

Comparable levels of antibacterial activity (Table 4, mass normalized antibacterial activity) are observed in the case of extract and extract loaded pSi (in dry powder form). Inhibition zones against *S. aureus* are listed in Table 4.

**Table 4.** Antibacterial activity (against *S. aureus*) of bamboo extract and extract loaded pSi after 24 h incubation period.

Material Tested	Avg Inhibition Zone	Mass normalized Inhibition Zone (mm)
Bamboo leaf extract (0.78 mg)	18±1	18
Extract loaded tabasheer-derived pSi (2.5 mg pSi with 25% wt loading)	13±1	15

Sustained release of antibacterial components from crude extract loaded pSi was monitored by disc diffusion assay according to the procedure outlined in the experimental section. Antibacterial activity against *S. aureus* was measured every 24 h until no measureable antibacterial activity was observed. Results were plotted as time (days) versus zone of inhibition. According to the plot shown in Fig.33, antibacterial activity was observed for a period of 16

days. Significant antibacterial activity, with a zone of inhibition above 15 mm, was observed for a period of 7 days, with measurable activity for 16 days.

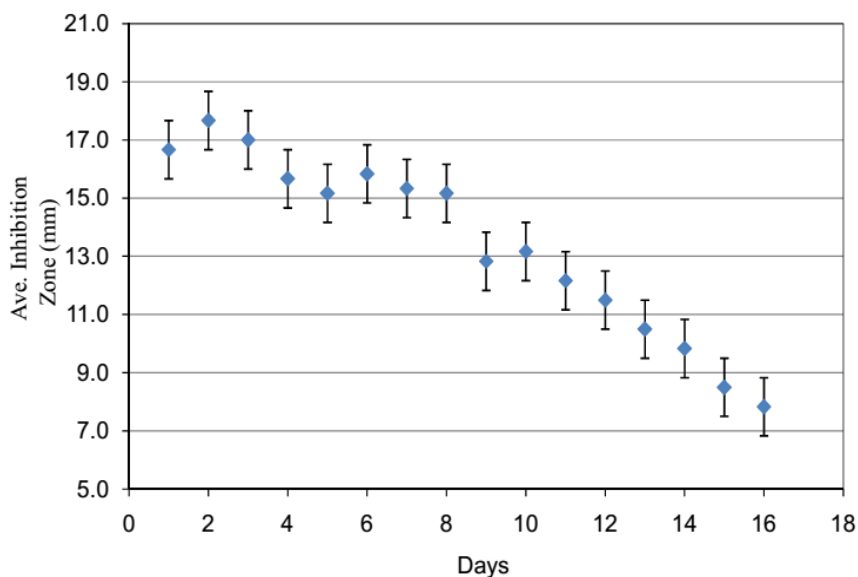


**Figure 33.** The release of antibacterial components from *Bambuseae* leaf extract loaded pSi (tabasheer derived) and their associated activity against *S. aureus*.

### 3.3.3. Isolation of some of the known antibacterials from *Bambuseae arundinacea*

We have identified two known antibacterial compounds present in the *Bambuseae* leaf extract (ethanol) by preparative thin layer chromatography (TLC). The method developed for the isolation of individual components is based on a modification of a previous literature method (discussed in the experimental section).<sup>124</sup> Compound **1** (yellow powder, ~1 mg) was identified as 2,6-dimethoxycyclohexa-2,5-diene-1,4-dione (2,6 dimethoxy-p-benzoquinone) and compound **2** (white powder, ~2 mg) identified as 3S,8S,9S,10R,13R,14S,17R)-17-[(E,2R,5S)-5-ethyl-6 methylhept-3-en-2-yl]-10,13-dimethyl-2,3,4,7,8,9,11,12,14,15,16,17 dodecahydro-1H-cyclopentaphenanthren-3-ol (stigmasterol) by comparing their spectral data (<sup>1</sup>H NMR, <sup>13</sup>C NMR, and ESI-MS) to that reported in the literature.<sup>125-127</sup> Compound **1** and compound **2** showed activity against *S. aureus* with individual minimum inhibitory concentrations (MIC) of 35



$\mu\text{g/mL}$ , and  $30 \mu\text{g/mL}$  respectively. These results falls within the range of MIC values (against *S. aureus*) reported for compound **1** ( $8\text{-}200 \mu\text{g/mL}$ ) and compound **2** ( $12.5\text{-}200 \mu\text{g/mL}$ ) in the literature.<sup>127-130</sup> The recorded  $^1\text{H}$  NMR,  $^{13}\text{C}$  NMR, and HRMS spectra for 2,6 dimethoxy-p-benzoquinone are presented in Fig.34, Fig.35, and Fig.36 respectively. For stigmasterol  $^1\text{H}$  NMR,  $^{13}\text{C}$  NMR, and HRMS spectra are presented in Fig. 37, Fig. 38, and Fig. 39.

**Compound 1:** TLC (Chloroform: Ethyl acetate: Acetic acid), 45:45:10 v/v):  $R_f = 0.7$ ;

$^1\text{H}$  NMR (400 MHz,  $\text{CDCl}_3$ ):  $\delta$  5.88 (s, 1H), 3.84 (s, 3H);

$^{13}\text{C}$  NMR (400 MHz,  $\text{CDCl}_3$ ):  $\delta$  186.84, 176.67, 157.33, 107.42, and 56.48;

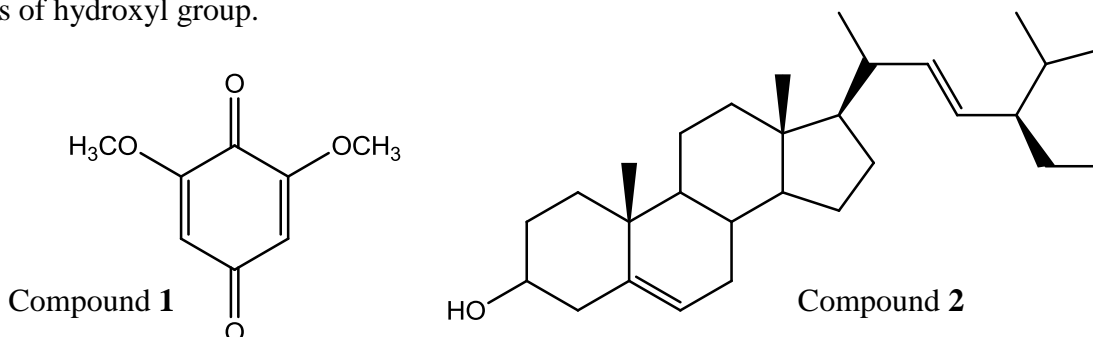
HRMS (ESI-TOF)  $m/z$  calcd. for  $\text{C}_8\text{H}_8\text{O}_4$ , 168.0823; found 169.1132 (M+H).

**Compound 2:** TLC (Hexane : Ethyl acetate , 60:40 v/v):  $R_f = 0.3$ ;

$^1\text{H}$  NMR (400 MHz,  $\text{CDCl}_3$ ):  $\delta$  5.38 (d, 1H,  $J = 5.2$  Hz), 5.16 (dd, 1H,  $J = 8.8, 8.8$  Hz), 5.06 (dd, 1H,  $J = 8.8, 8.8$  Hz), 3.54 (m, 1H), 2.29 (m, 2H), 2.03 (m, 3H), 1.85 (m, 2H), 1.72-1.41 (m, 10H), 1.27-1.18 (m, 14H), 1.15-1.03 (m, 6H), 0.90-0.82 (m, 13 H), 0.72 (s, 2H);

$^{13}\text{C}$  NMR (400 MHz,  $\text{CDCl}_3$ ):  $\delta$  140.76, 138.32, 129.29, 122.71, 71.81, 56.88, 55.97, 51.25, 50.17, 42.30, 42.22, 40.50, 39.69, 37.27, 36.52, 31.91, 31.89, 31.66, 28.93, 25.42, 24.37, 21.23, 21.09, 19.41, 18.99, 12.26, 12.06;

HRMS (ESI-TOF)  $m/z$  calcd. for  $\text{C}_{29}\text{H}_{48}\text{O}$ , 412.3705; found 395.4788 (M-17), corresponds to loss of hydroxyl group.



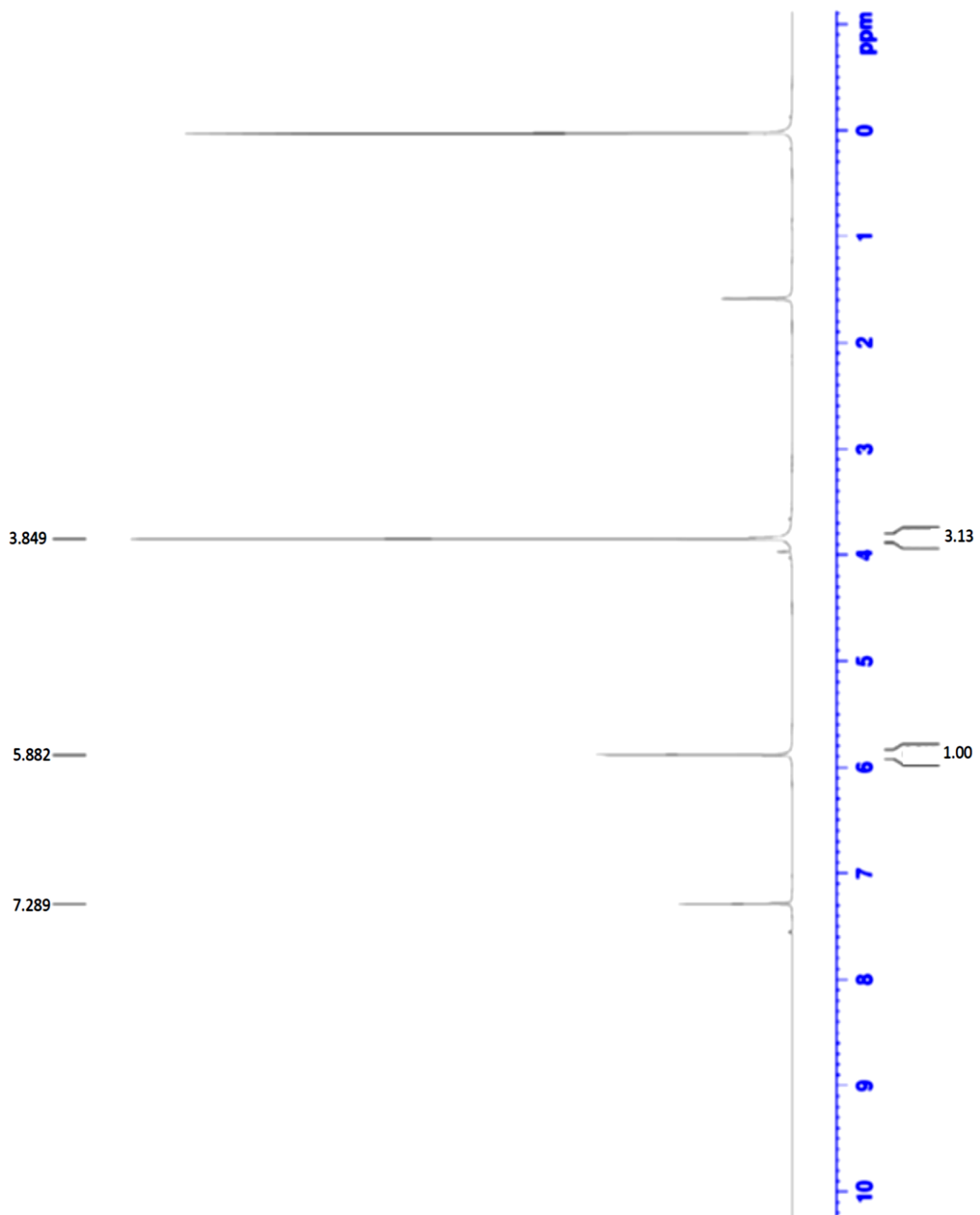


**Figure 34.**  $^1\text{H}$  NMR spectrum of compound (1) in  $\text{CDCl}_3$  (400 MHz).

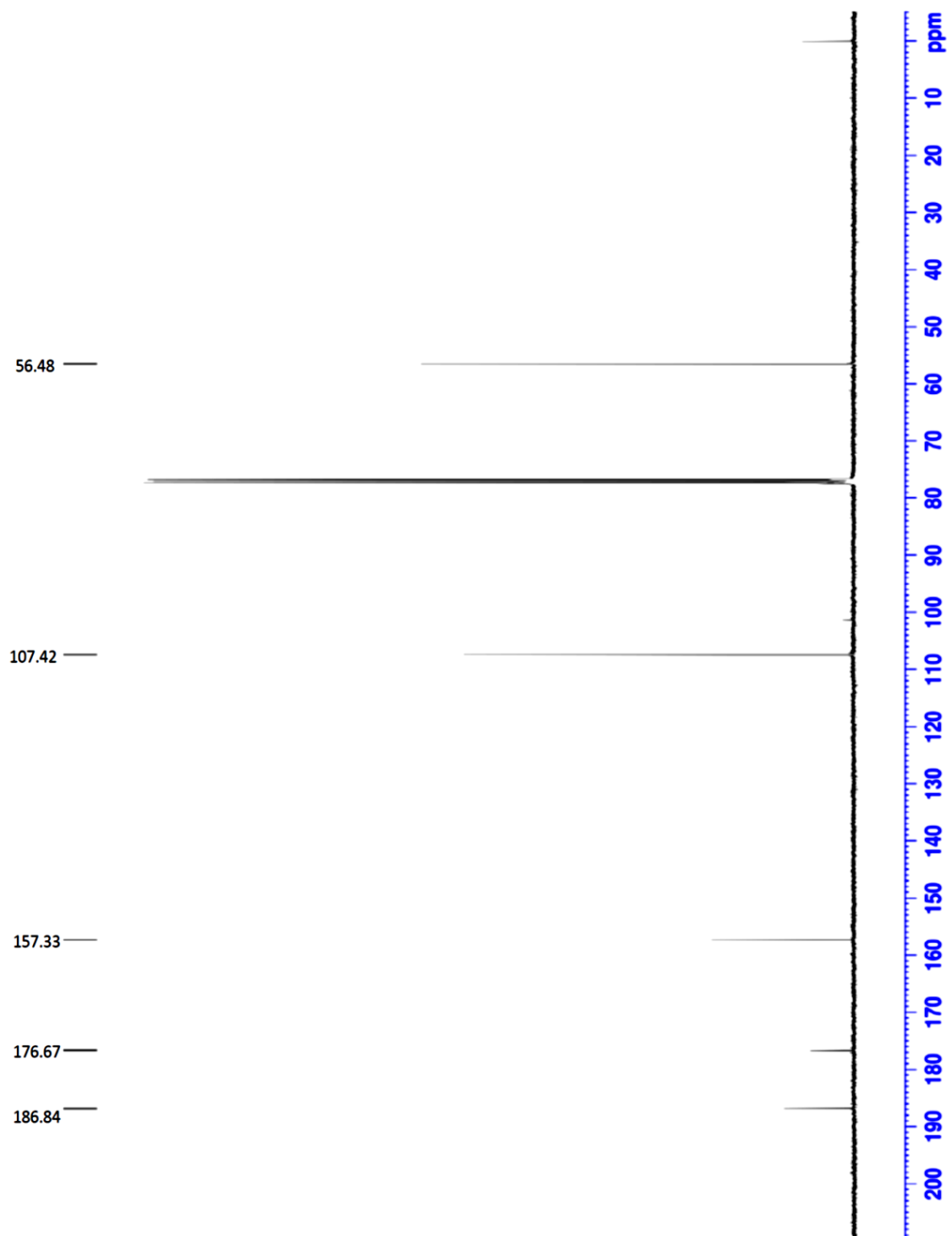


**Figure 35.**  $^{13}\text{C}$  NMR spectrum of compound (1) in  $\text{CDCl}_3$  (400 MHz).

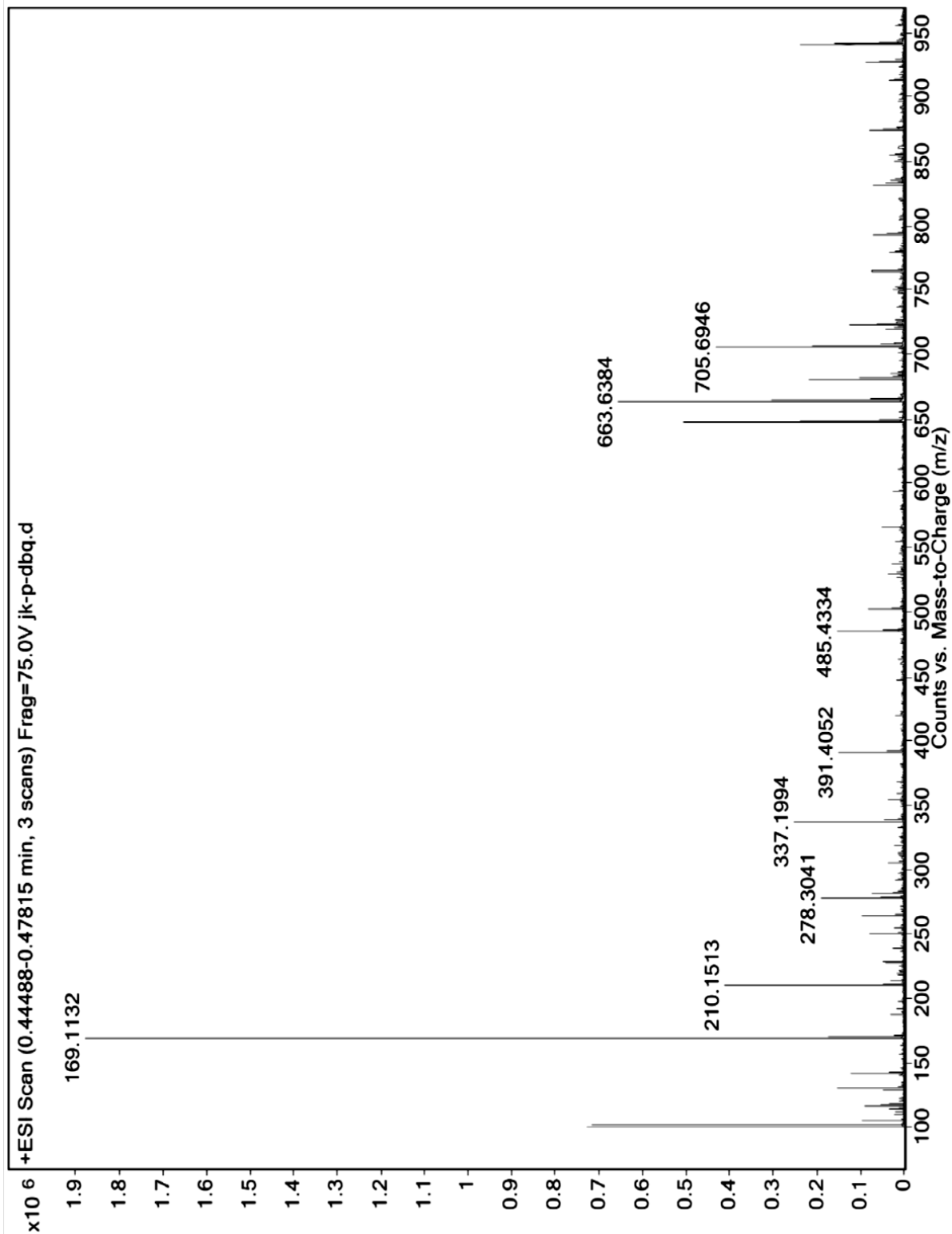
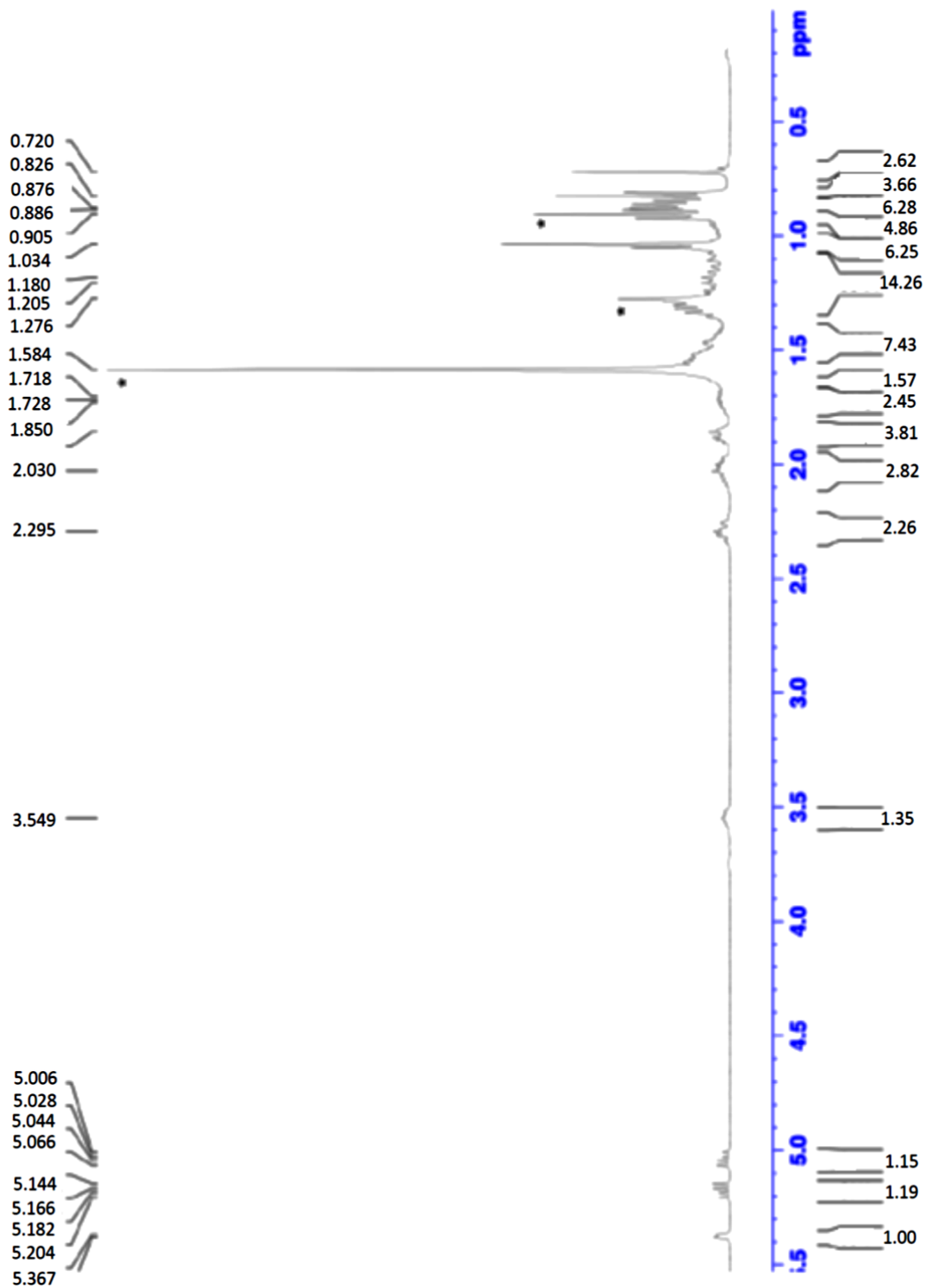


Figure 36. HRMS (ESI-TOF) data for compound 1.



**Figure 37.**  $^1\text{H}$  NMR spectrum of compound (2) in  $\text{CDCl}_3$  (400 MHz). Peaks noted with asterisks (\*) indicate the presence of some residual solvent in the regions indicated.

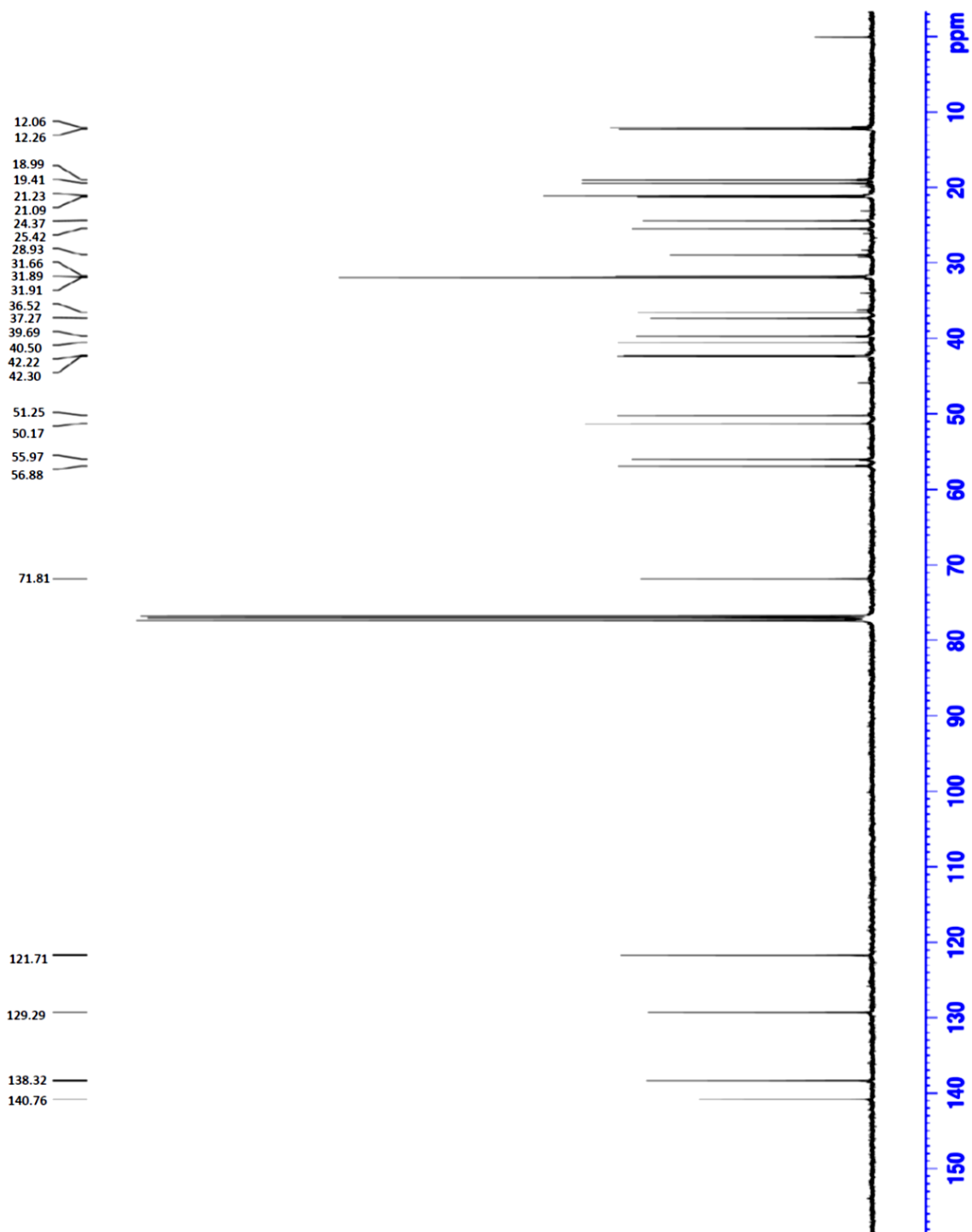


Figure 38.  $^{13}\text{C}$  Compound (2) in  $\text{CDCl}_3$  (400 MHz).

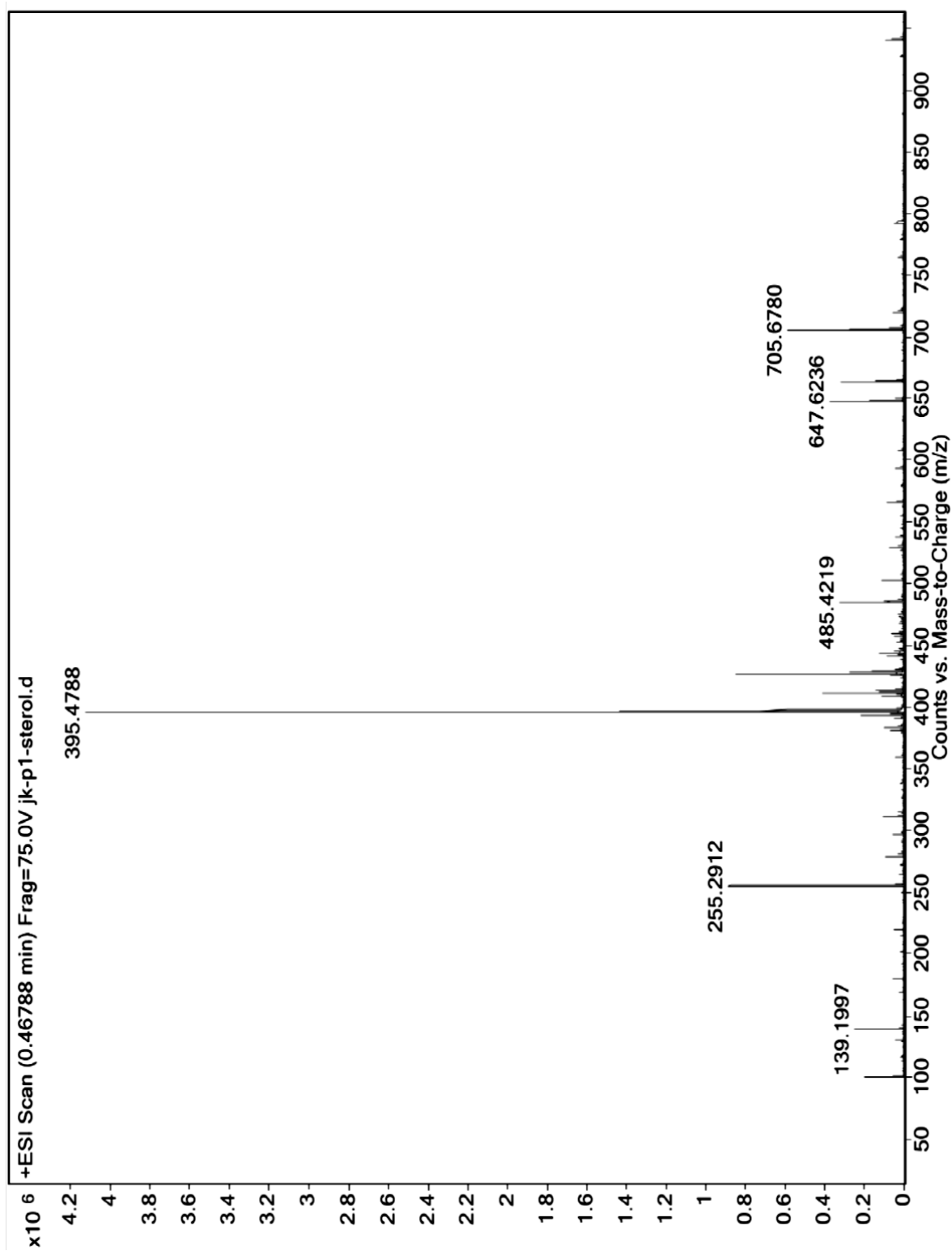


Figure 39. HRMS (ESI-TOF) data for compound 2.

### 3.3.4. Summary

We have shown here that a single plant (*Bambuseae arundinacea*), can yield bioactive components (antibacterial) as well as drug delivery carrier (pSi). *In vitro* studies on the sustained release of the antibacterial components from the pSi carrier matrix showed prolonged antibacterial activity for a period of > 2 weeks. Two antibacterial components from the *Bambuseae* leaf extract were isolated and identified as 2,6 dimethoxy benzoquinone along with stigmasterol. Leaf extracts of silicon accumulator plants (*Bambusae bambose L.*) have shown antibacterial activity against multi drug resistant bacteria (MDR),<sup>121</sup> and one of the compounds isolated from *Bambuseae* (stigmasterol) was reported previously to have synergistic antibacterial activities when used along with ampicillin against drug resistant clinical isolates.<sup>131</sup> Based on the literature evidence, our study on deriving pSi nanostructures from eco-friendly cost effective feedstocks (silicon accumulator plants) that also can yield a therapeutic agent opens up the possibility of using these plant based drug delivery carriers as a low-cost option for countries with extensive resources of silicon accumulator plants in future synergistic drug delivery applications. The following chapters will focus on use of plant-derived nanostructured porous carriers for incorporation and release of bioactive components (vitamins) along with other natural product-derived species.



## **Chapter IV**

### **Vitamin D3 (Cholecalciferol) Loading and Release from Tabasheer Derived Porous Silicon Powders**

#### 4.1. Introduction

Poor bioavailability and low stability of pharmaceuticals and nutraceuticals are two key challenges in pharmaceutical and food industries. Poor solubility is one of the main reasons for poor oral bioavailability of many pharmaceuticals and nutraceuticals.<sup>132</sup> It is reported that only 10% of the pharmaceuticals that are in the market are poorly soluble, but 40% of lead candidates (hydrophobic drugs) fail to reach market due to their poor solubility.<sup>133</sup>

The lipophilicity ( $\log P$ ), is a measure of solubility of hydrophobic drugs, where  $P$  is described as the ratio of the concentration of the unionized compound at equilibrium between organic and aqueous phases.<sup>134</sup> In 1997, Christopher A. Lipinski, a medicinal chemist from Pfizer developed a concept called “Lipinski’s rule of five”, according to this rule hydrophobic or lipophilic drugs with  $\log P$  value below 5 are the only candidates suitable for oral delivery.<sup>135</sup> Pharmaceutical and biotechnology companies use lipophilicity ( $\log P$ ) as a measure to understand pharmacokinetic properties (absorption, distribution in the body, penetration across vital membranes and biological barriers, metabolism and excretion) of the drug. Compounds with a higher  $\log P$  value will have a lower aqueous solubility and therefore compromises the oral bioavailability which in turn affects the effectiveness of a drug.<sup>136</sup>

Stability of pharmaceuticals and nutraceuticals is another area of challenge where the active ingredients long term stability is questionable due to light sensitive or heat sensitive chemical functionalities present within the molecule. Microencapsulation techniques have shown to be successful in food and pharmaceutical industries to protect and control the release of active ingredients over past few decades. Nanoencapsulation, on the other hand, along with protection and controlled release, enhances the bioavailability of the active ingredients.<sup>137</sup>

Mesoporous silicon powders with high surface areas and tunable surface chemistries offer loading of a variety of biologically-active agents (discussed in Chapter 1). Hydrophobic drugs and nutrients are entrapped into anodized and stain etched silicon powders to increase their bioavailability. Some of the examples studied to date include pharmaceuticals (ibuprofen, griseofulvin, indomethacin) and nutraceuticals (vitamin B9, vitamin E, lycopene, coenzyme Q10).<sup>138-141</sup>

One concern of using pSi particles derived from anodization and stain etching is usage of corrosive solvents and expensive solid silicon feedstocks (discussed in Chapter 2). pSi particles prepared by these methods are expensive to use for low value food, pharmaceutical, and nutraceutical delivery. With a primary focus on economy, and eco-friendly nature of the fabrication route, we present pSi particles derived from plant as a viable source without compromising the purity needed (> 99%) for these applications.

In this study, we used the photosensitive vitamin D3 (VD) as a model drug to load into tabasheer derived pSi particles with an aim to improve its bioavailability. VD is a highly crystalline, hydrophobic nutrient with a log *P* value of 7.5. It is loaded into pSi by two different loading methods, melt loading and incipient wetness impregnation to observe the effect of loading on dissolution of the VD. The total loading capacities and encapsulation efficiencies were estimated for these two methods by thermogravimetric analysis and UV-Vis absorbance spectroscopy. Melting point and crystallinity of VD after loading into pSi were evaluated by differential scanning calorimetry (DSC), powder X-ray diffraction (XRD), and correlated with dissolution behavior of the VD.

## 4.2. Experimental

### 4.2.1. Loading cholecalciferol (VD)

Loading of VD (Sigma Aldrich,  $\geq 98\%$ ) is achieved by infiltration into mesoporous Si powders using two methods, melt loading and incipient wetness impregnation.<sup>142,143</sup> In case of the solvent-free melt loading method, the vitamin is melted in the presence of the pSi powder at or above melting temperature (87 °C) of crystalline VD, whereas in case of incipient wetness impregnation, pSi powders were impregnated with a known concentration of VD solution. To minimize the degradation by light, loading capacity and encapsulation efficiencies (EE) were quantified as soon as possible after the loading. All the samples were stored in containers covered in aluminum foil.

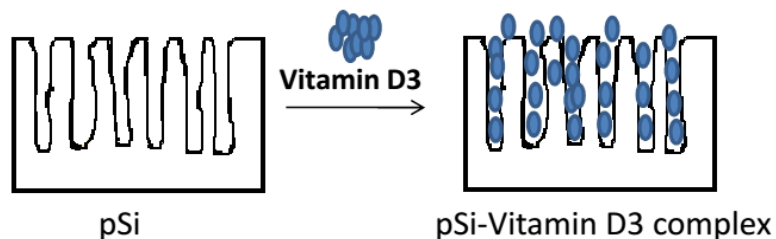


**Figure 40.** Loading pSi powders with VD.

#### 4.2.1.1. Melt loading

Tabasheer derived pSi particles (7.2 mg) of 25  $\mu\text{m}$  size were preblended with the VD powder (3.4 mg) and melted at 90°C for 5 min. The pSi-vitamin matrix was then cooled to room temperature. Loaded powders were dried under vacuum at room temperature for 4 h.

#### 4.2.1.2. Incipient wet impregnation

VD (1.98 mg) was dissolved in 50  $\mu\text{L}$  of ethanol and added to tabasheer derived pSi (10.6 mg) in 2X25  $\mu\text{L}$  aliquots. After addition of each aliquot pSi powders were air dried for 1 h. The loaded powders were dried in vacuum oven at room temperature for 12 h.

#### 4.2.2. Preparation of vitamin D3 standard curve

A stock solution of standard VD was prepared by dissolving 2.35 mg of VD in 1 ml of 65% ethanol in water containing 7 mM tween 80. Standard solutions of VD were prepared from stock solution in the concentration range of 1.175-23.5  $\mu\text{g/ml}$  in 65% ethanol (in water containing 7 mM tween 80) as a solvent. The absorbance of VD standard solutions was measured at 256 nm ( $\lambda_{\text{max}}$  for VD) against the solvent as blank. Calibration curve of absorbance as a function of concentration was generated (Figure 41). Best fit line has a y intercept of  $\sim 0.1$ , this could be due to the scattered light from insoluble VD fraction in the aqueous solvent system.

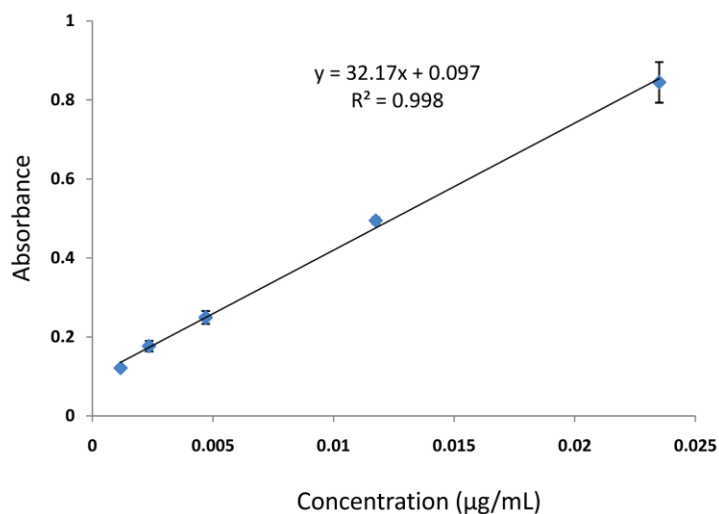


**Figure 41.** Calibration curve for VD prepared in 65% ethanol (in water containing 7 mM tween 80).

#### 4.2.3. Measuring encapsulation efficiencies (EE)

Encapsulation efficiencies of VD within the pSi powders by melt loading and incipient wet impregnation methods were determined by extracting VD from 1 mg of pSi-VD complex in 1.0 ml of ethanol for 24 h with continuous magnetic stirring. The extracted solution was then filtrated and analyzed by UV-absorbance spectroscopy. The mass of the vitamin released after 24

h was determined by comparing the absorbance to the standard curve developed in ethanol (95% v/v,  $\lambda_{\text{max}}$  264 nm).

$$EE\% = \frac{(\text{Mass of released vitamin after 24 h})}{\text{Mass of vitamin added to pSi}} \times 100$$

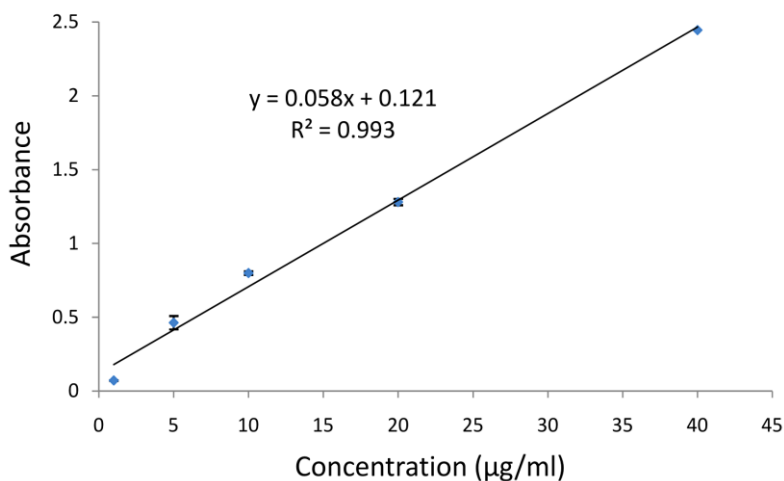


**Figure 42.** Calibration curve for VD prepared in 95% ethanol.

#### 4.2.4. *In vitro* release of VD

pSi particles loaded with VD by melt loading (4 mg) and incipient wetness impregnation loading (5 mg) method were placed in a vial with 1 mL release medium (7 mM tween 80 in water). Release experiments of VD from pSi-VD complex were performed at 37 °C, at a shaking speed of 140 rpm. At the end of given time point, release medium was centrifuged, supernatant was removed and replenished with 1 mL of fresh medium. The amount of VD released from pSi at a given time point was quantified in reference to a standard curve generated independently from solutions of known concentration.

#### 4.2.6. Instrumentation

Mass spectrometry (MS) was performed using an Agilent Technologies 6224 TOF MS/MS system. Thermogravimetric analysis (TGA) was performed using a Seiko S II

model SSC/5200 TGA at a heating rate of 10°C/min (up to 400°C) under nitrogen. Differential scanning calorimetry (DSC) analysis was done using DSC 2 system (Mettler Toledo). Sample was heated from 25 to 110 °C at the rate of 10 °C/min, under nitrogen flush. X-ray diffraction was carried out using a Phillips 3100 X-ray powder diffractometer with Cu K $\alpha$  radiation operating at 35 kV. A Beckman DU-64 spectrophotometer was used for measuring the absorbance of VD.

### 4.3. Results and Discussion

#### 4.3.1. Loading of VD into pSi particles

Tabasheer derived pSi microparticles ( $25 \pm 15 \mu\text{m}$ ) were loaded with VD by melt loading and incipient wetness impregnation. VD is sensitive to various environmental factors. For example, prolonged exposure to light and/or heat can induce isomerization or oxidation of VD.<sup>144</sup> To ensure complete melting of the VD into pSi and to minimize the heat induced degradation, VD is loaded into pSi by melt loading at a temperature of 95 °C slightly above the melting point of VD (87 °C). A mixture of pSi and VD in the mass ratio of 2:1 is melted for 4 min, then cooled to room temperature. Heat induced degradation of VD results in formation of hydroxy vitamin D3 (Fig. 43).<sup>145</sup>

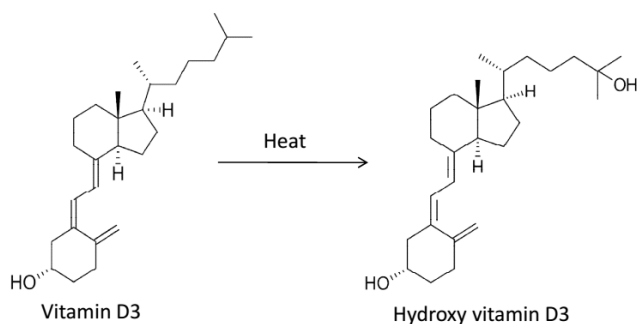


**Figure 43.** Heat induced oxidation of VD, adapted from ref 144.

To evaluate the stability of VD after melt loading, VD is extracted from the pSi-VD melt load complex (1 mg) by dissolving in ethanol (1 mL). The extracted VD was analyzed by mass

spectrometry. Mass spectroscopy data from forced heat induced degradation of VD at 95 °C for 20 min is compared with the mass spectrum of VD extracted from melt loaded pSi at 95 °C for 4 min to observe formation of any degradation products. Fig. 44 shows a mass spectrum observed from pure VD powder, while Fig. 45 shows a mass spectrum of heat induced degradation products of VD powder. From the mass spectrum (Fig. 46), no heat induced degradation was observed after loading the VD into pSi by melt load method

**Vitamin D3:** HRMS (ESI-TOF)  $m/z$  calcd. For  $C_{27}H_{44}O$ , 384.6377; found 385.3555 (M+H).

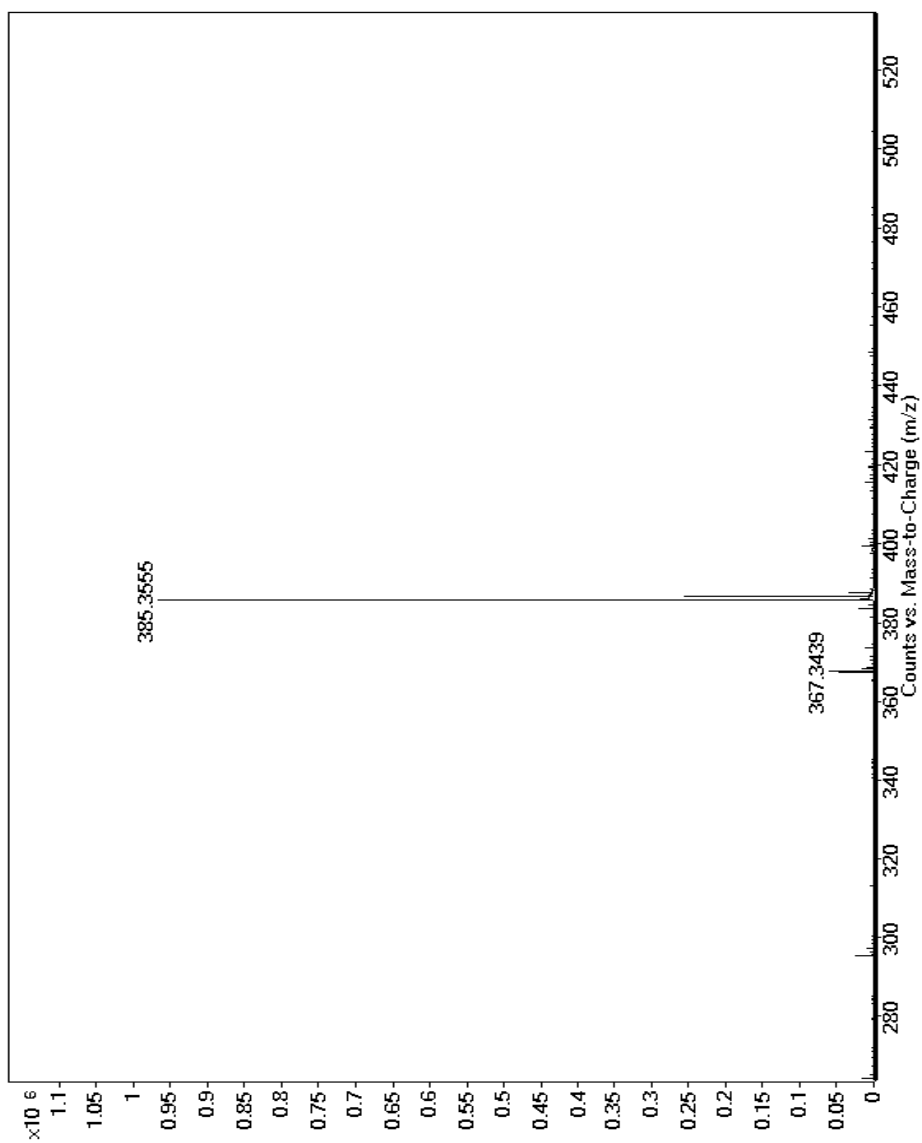


**Figure 44.** Mass spectrum of VD.



## Forced degradation of VD

Hydroxy Vitamin D3: HRMS (ESI-TOF) m/z calcd. For  $C_{27}H_{44}O$ , 400.3341; found 383.3380(M-17), corresponds to loss of hydroxyl group.

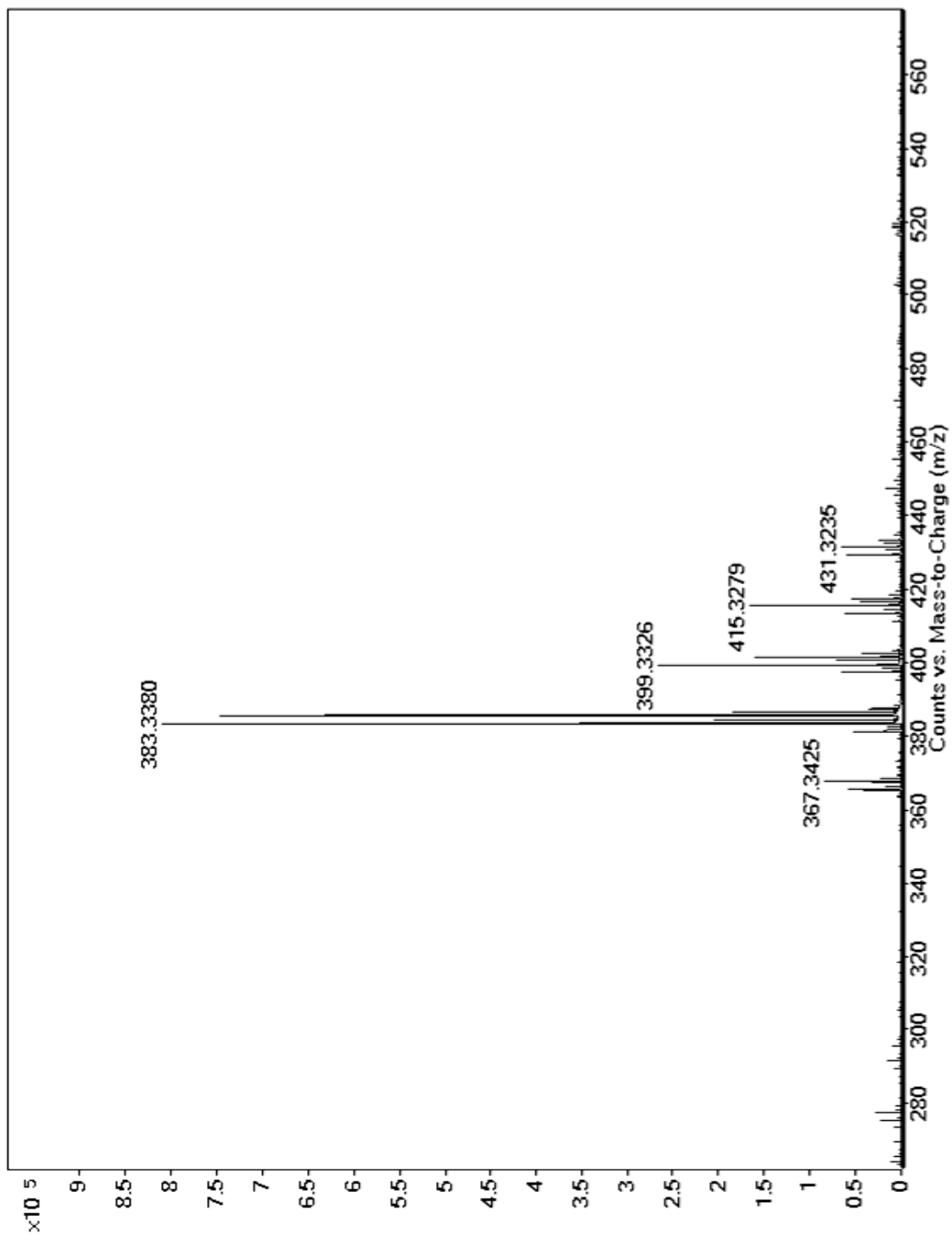


**Figure 45.** Mass spectrum of melted vitamin D3 at 95°C for 20 min.

**Vitamin D3 extracted from melt load:**

HRMS (ESI-TOF) m/z calcd. for C<sub>27</sub>H<sub>44</sub>O, 384.6377; found 385.3607 (M+H).

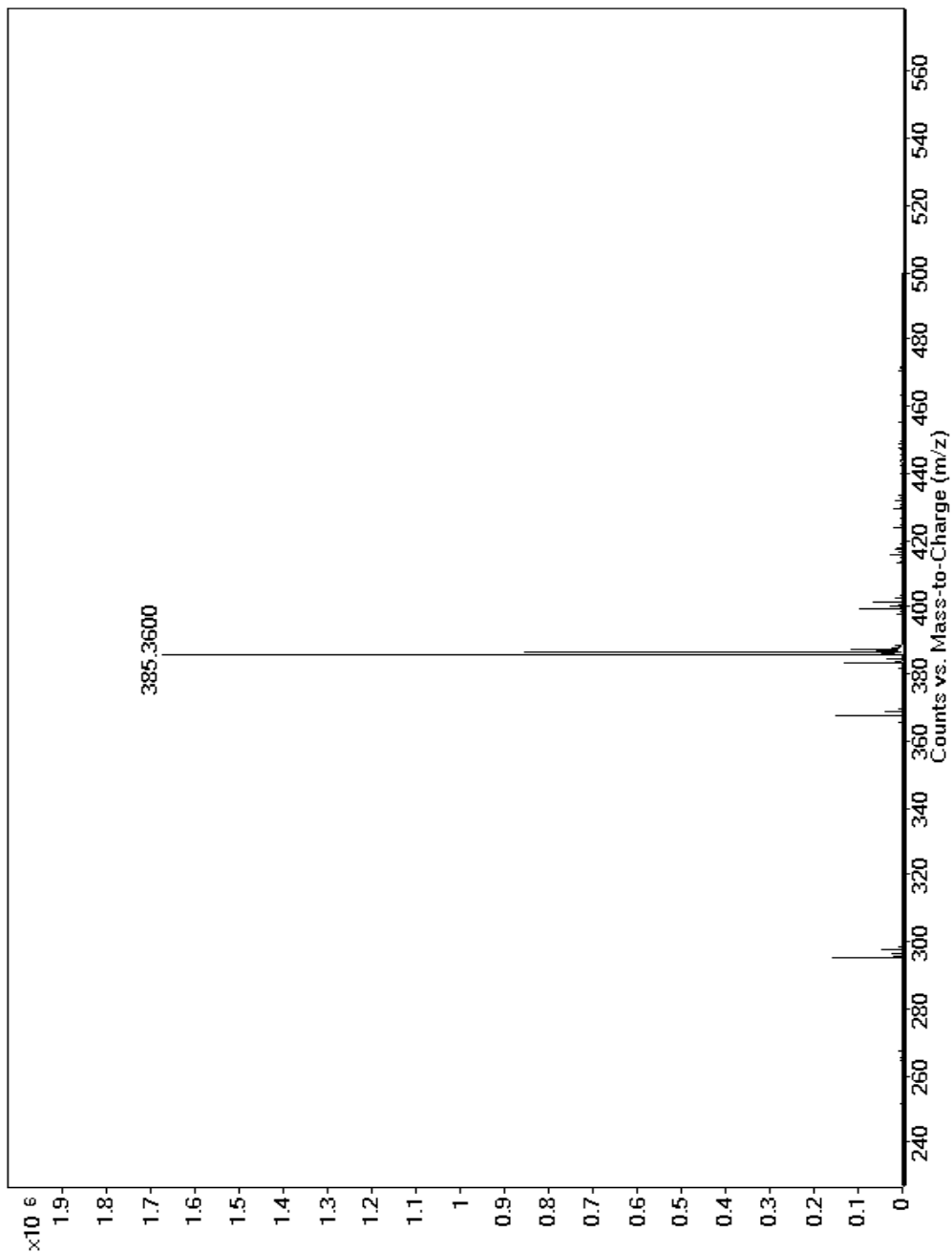


**Figure 46.** Mass spectrum of VD loaded into pSi by melt loading method.

### 4.3.2. Loading capacities of VD into pSi

The total payload (VD) adsorbed into pSi was determined by thermogravimetric analysis (TGA). Melt loaded VD into pSi with a theoretical maximum loading percentage of 50% demonstrates a loading capacity of 26% (wt) by TGA. Thermogram of melt loaded VD into pSi (Fig. 47a) shows significant mass loss (26 %) in the range of 150-450 °C, and a weight loss in the temperature range of 0-100 °C due to evaporation of moisture (< 2%). Thermal degradation of VD loaded into pSi has not reached a plateau, indicating that TGA analysis reflects a lower estimate of total loading capacity by weight. In case of incipient wetness impregnation, TGA trace (Fig. 47b) shows mass loss of 2% in the range of 0-100 °C due to evaporation of loading solvent ethanol and notable mass loss was observed in the range of 100-450 °C (6%), probably due to decomposition of the VD. From the TGA analysis total loading capacity of VD by melt load is estimated as 26% (wt), and from incipient load is 6% (wt) excluding the mass loss due to solvent or moisture.

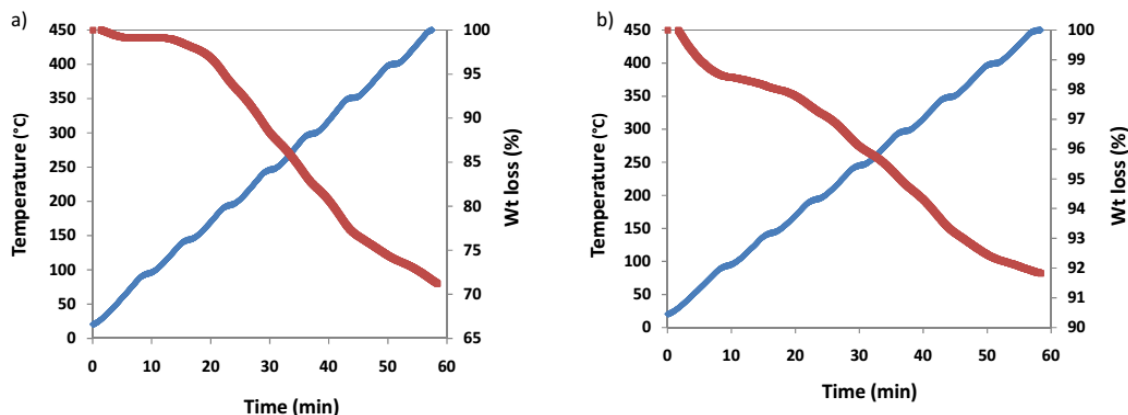


**Figure 47.** Thermogravimetric analysis of a) VD loaded into pSi by melt loading, b) VD loaded into pSi by incipient wetness impregnation

Total loading capacities of vitamin into pSi by TGA, and encapsulation efficiencies measured by UV-Vis absorbance spectroscopy for melt loading method and incipient wetness

impregnation method are listed in Table 5. Lower loading efficiency in case of incipient loading is observed compared to melt loading, this can be attributed to competition of hydrophobic vitamin and polar solvent with the surface silanol groups on the pores. Intermolecular interactions between the solvent EtOH and the silanol groups on the pore wall surface might have led to lower VD adsorption at lower concentrations into the pores for the latter loading method.

**Table 5.** Vitamin loading capacities into tabasheer derived pSi using different methods.

Loading Type	Theoretical Loading (wt %)	Thermogravimetric Analysis (wt %)	Encapsulation Efficiency (EE) (wt %)
Melt Loading	50	26	99
Incipient Loading	18	6	65

#### 4.3.4. DSC analysis

DSC measurements were carried out to characterize the physical state of the vitamin, whether it is confined within the pores or recrystallized onto the outer surfaces of the pSi particles. DSC thermograms for VD loaded into pSi by melt load and incipient wetness impregnation are presented in Fig. 48. A sharp endothermic melting peak at 87 °C was observed for the crystalline VD. In the case of melt loaded VD and incipient loaded VD, broad melting peaks were observed with a depression in melting point. The melting point (peak minimum) for VD shifted to a temperature of 60 ° C for the incipient load method vitamin into pSi, whereas in case of that of the melt loading method, the melting peak minimum was at 64 ° C. This phenomenon indicates change in the solid state features of crystalline VD due to pore confinement. More specifically, once confined into the pores, the crystallite size of VD is

restricted by the pore dimensions.<sup>146-148</sup> A lower melting point of the entrapped agent is an indication of reduced crystallite size. The broad nature of the melting endotherms after loading into pSi is likely due to the presence of different crystallite sizes present within the mesoporous walls of pSi particles.<sup>147</sup>

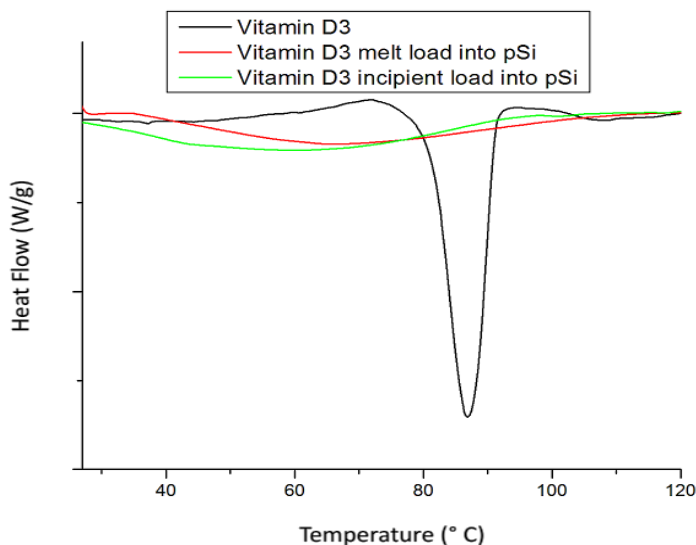


**Figure 48.** Differential scanning calorimetry of pSi loaded with vitamin D3.

#### 4.3.5. XRD analysis

An overlay of XRD diffractograms obtained for pSi microparticles, crystalline VD, melt loaded VD, and VD loaded by incipient loading are presented in Figure 49. The presence of crystalline silicon is evident from XRD analysis, with the cubic Si (111), (220), and (311) reflections observed at  $2\theta$  values of  $27^\circ$ ,  $46^\circ$ ,  $54^\circ$  respectively (Chapter 2). The diffractogram of cholecalciferol (VD) alone with the most intensive peak at  $18.2^\circ$  suggests its existence in a crystalline form. The diffractogram for VD melt load and incipient load samples with absence of this intensive crystalline peak infers a significant reduction in particle size (‘nanostructuring’) or an extreme line broadening below the detection limit of the instrument.<sup>146</sup>

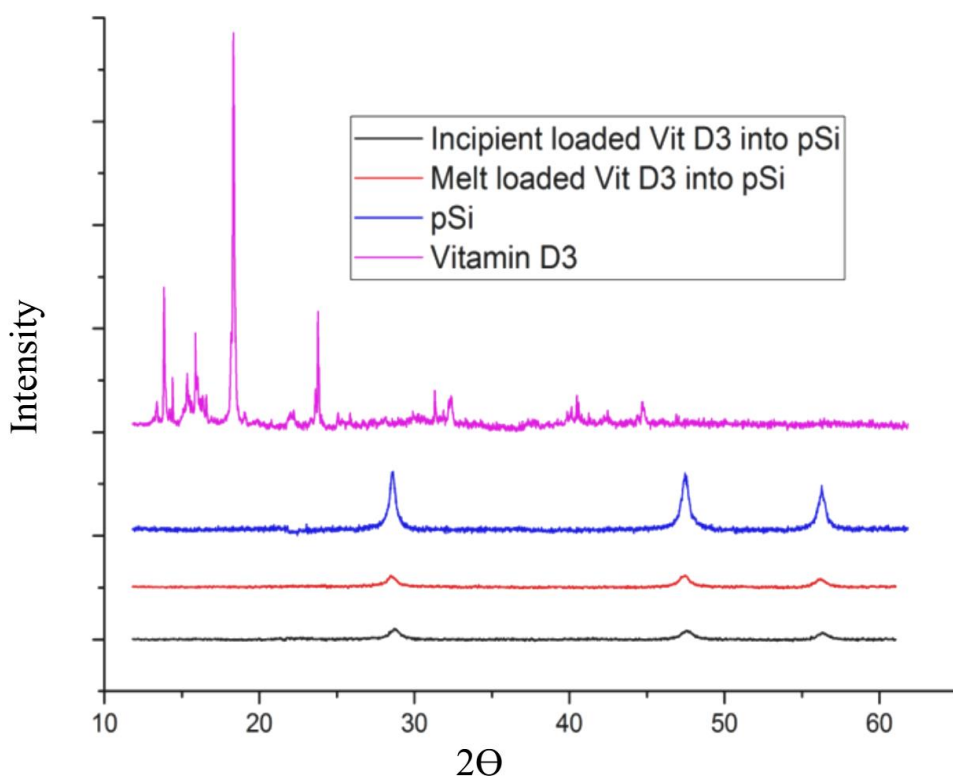


**Figure 49.** Over lay of XRD pattern of vitamin D3, pSi loaded with vitamin D3 by melt load and incipient load methods.

#### 4.3.6. *In vitro* release of the VD from pSi

*In vitro* release of the VD from pSi for melt load and incipient load was shown in Fig. 50. Cumulative release of vitamin shows gradual release of vitamin from pSi-VD complex. At the end of a 21 h time period (1260 min), the cumulative percentage of soluble vitamin released in case of melt loading is 79%, incipient loading 99% and VD itself is 8.5%. This suggests an enhanced solubility of the vitamin after loading into pSi. Even though the high encapsulation efficiencies achieved by melt loading methods are advantageous to carry high payloads, in presence of high concentration of the vitamin filled into the pores might recrystallize which leads to reduced dissolution of vitamin.<sup>147</sup> The following are the two important factors identified for enhanced solubility of VD: 1) nanocrystalline state of VD was achieved after loading into pSi

(evident from the XRD and DSC analysis) 2) increased surface area of the vitamin after loading into high surface area pSi powders.

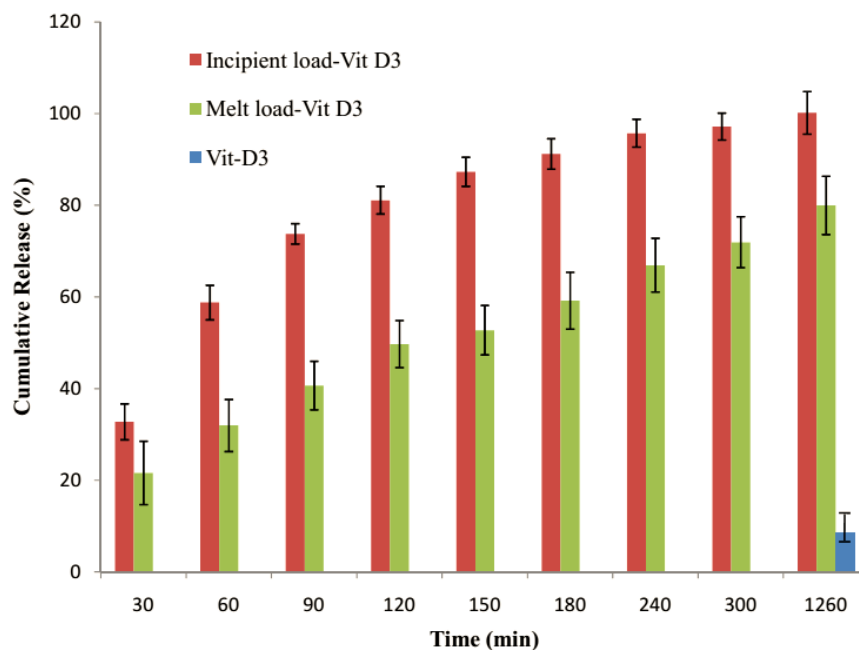


**Figure 50.** Release of soluble VD from VD-loaded pSi.

#### 4.4. Summary

This initial study provides proof-of-concept of the use of plant derived pSi powders as controlled release carriers for hydrophobic vitamins. Two loading methods were optimized to see the effect of drug loading on the dissolution profiles of the VD. With the combination of DSC and XRD methods, the physical state of VD after loading into pSi has been evaluated. A cumulative release profile shows at the end of 1260 min the total amount of soluble drug itself was 8.5%, but loading into pSi, enhanced the amount of soluble vitamin by ~ 11 times (99%) in case of incipient wetness impregnation, and ~ 9 times (79%) in case of melt loading method. Future studies will involve UV light induced degradation of vitamin D3 and evaluation of the ability of plant derived pSi to minimize the UV light induced degradation.

## **CHAPTER V**

### **Loading and Release of *Equisetum Arvense* Leaf Extract (Anti-inflammatory & Anti-Oxidant) from Porous Silicon Powders**



## 5.1. Introduction

Chronic inflammation is a condition involved with number of diseases including cancer, Alzheimer's disease, rheumatoid arthritis. Prolonged usage of anti-inflammatory drugs is necessary in these cases to reduce the inflammation associated with it. Nonsteroidal anti-inflammatory drugs (NSAIDs) and small biological molecules are very promising to treat this condition, but long term usage of NSAIDs are associated with serious side effects, thereby affecting quality of life. The use of small biological drug molecules (chimeric monoclonal antibodies) have shown decreased activity over time due to drug resistance.<sup>149, 150</sup>

A safe and effective alternative for treating chronic inflammation is the use of plant extracts rich in polyphenolic compounds.<sup>151</sup> Some of the well-known polyphenols that have shown anti-inflammatory activity are curcumin, epigallocatechin gallate, and quercetin.<sup>152-154</sup> Synergistic anticancer activity of polyphenolic compounds was observed in many cases; curcumin and catechin showed high growth inhibition of human colon adenocarcinoma cells and use of quercetin and doxorubicin showed greater inhibition of cancer cells that are resistant to doxorubicin.<sup>155,156</sup> However, one of the major problems associated with the use of such compounds is their low bioavailability and relatively short half-life.<sup>157-159</sup> Because of this poor bioavailability, high oral doses or repeated dosing is needed to reach an effective plasma concentration.

To overcome these challenges with polyphenolic-containing extracts, we have encapsulated ethanolic extracts of *Equisetum arvense* (Horsetail, itself a Si accumulator plant) into porous silicon (pSi) microparticles to increase their bioavailability. Such extracts were loaded into nanostructured pSi particles prepared by our previously optimized eco-friendly fabrication route from silicon accumulator plants (Chapter 2). In this study, the potential utility

of pSi microparticles loaded with *E. arvense* ethanolic leaf extracts as a therapeutic agent were evaluated for their anti-inflammatory and antioxidant properties. We have subsequently optimized encapsulation techniques to efficiently load these *Equisetum arvense* extracts into pSi particles to release antioxidant and anti-inflammatory components in a sustained fashion.

A variety of inflammatory mediators and cellular pathways are extensively studied to understand the anti-inflammatory activity of many biologically-active components. We have investigated the anti-inflammatory activity of ethanolic extracts of *E. arvense* released from pSi microparticles by studying their effect on tumor necrosis factor  $\alpha$  (TNF $\alpha$ ) mediated nuclear factor kappa-light-chain-enhancer of activated B cells (NF- $\kappa$ B) activation. Fig. 51 shows the NF- $\kappa$ B mediated cellular pathway to trigger the production of pro inflammatory cytokines.

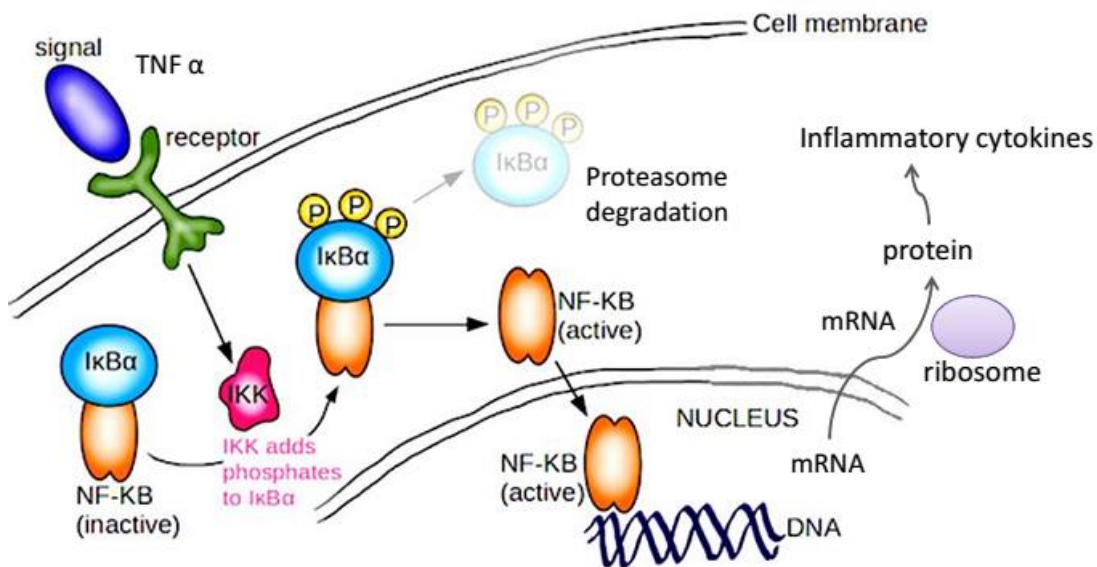


**Figure 51.** Mechanism of NF- $\kappa$ B activation through TNF $\alpha$ . Adapted from ref 161.

NF- $\kappa$ B is a transcription factor regulates various cellular responses that involve cell proliferation, apoptosis, immune responses to infection and inflammation.<sup>160</sup> NF- $\kappa$ B molecules

exist in most of the cells in an inactive form complexed with the inhibitory protein, IκB. In response to a stimulus (eg. Cytokines-IL2 and TNF, viral, bacterial endotoxins, UV radiation) IκB kinase (IKK) enzyme phosphorylates IκB unit that is conjugated to NF-κB. IκB detaches from the NF-κB through proteasomal degradation, and activates NF-κB nuclear translocation. NF-κB is then attaches to a specific sequence of the DNA and stimulates the production of specific proteins responsible to trigger inflammation.<sup>161</sup>

The anti-oxidant potential of these extracts was evaluated by an  $\alpha$ ,  $\alpha$ -diphenyl- $\beta$  picrylhydrazyl (DPPH) free radical scavenging method where stable DPPH (1,1-diphenyl-2-picrylhydrazyl) free radicals were reduced to DPPHH (1,1-diphenyl-2-picrylhydrazine) in the presence of the ethanolic extracts of *E. arvense*.<sup>162</sup>

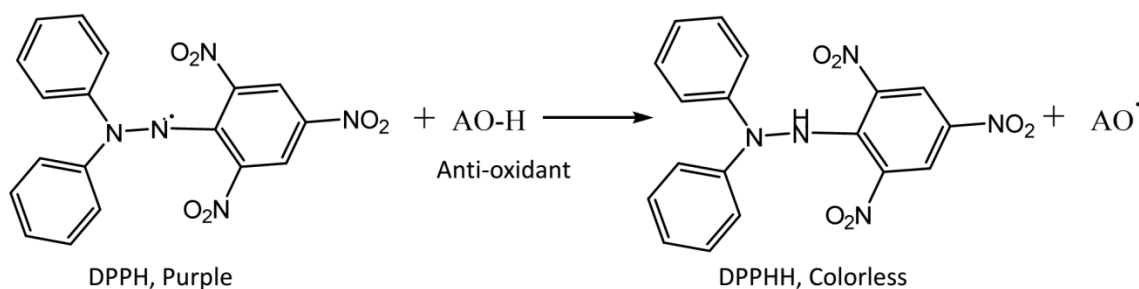


**Figure 52.** Schematic representation of the DPPH assay.

## 5.2. Experimental

### 5.2.1. Soxhlet extraction of *Equisetum arvense* leaves

*Equisetum arvense* leaves and stems were harvested from a natural source in Malvern, Worcestershire, UK in Fall 2016. Obtained leaves were shade dried for two days. Ground powder (6 g) was extracted with 50% ethanol (100 mL) at a temperature of 120 °C in a soxhlet extractor. After 6 h, the extract was concentrated through the use of rotary evaporator, and the dry extracts were stored at 4 °C for further analysis.

### **5.2.2. Loading of *Equisetum arvense* leaf extract into pSi**

Leaf extract was loaded into tabasheer derived pSi particles using a solution loading method. Dried extract powder (3.4 mg) was dissolved in a solvent mixture of ethanol, water and dimethyl sulfoxide (2:2:1 by volume). Extract solution (150  $\mu$ L) was added to the pSi particles (10.2 mg). The mixture was then dried under vacuum overnight.

### **5.2.3. Luciferase assay**

A luciferase assay was used to measure the luciferase gene expression triggered by TNF $\alpha$ -induced activation of NF- $\kappa$ B. HEK 293 cells were treated with the anti-inflammatory extract released from the pSi particles. HEK293 cells were plated in 24 well plates with a cell density of 50,000/well. After 24 h, cells were transfected (step 1) with two plasmids RLCMV-LUC (5 ng/mL *Renilla sp.*); PRDII-LUC (10 ng/mL firefly) using a commercial transfecting agent Lyovect (Invitrogen). PRDII-LUC plasmid has a NF- $\kappa$ B binding site and luciferase reporter (LUC) site. RLCMV-LUC (5 ng/mL; *Renilla sp.*) with a luciferase reporter site is used as an internal control, so that by normalizing the activity, experimental variability (eg. cell viability or transfection efficiency) will be minimized. After 48 h of transfection, cells were treated with different concentrations of anti-inflammatory extract (100  $\mu$ L) prepared in 1% DMSO (step 2); one hour later cells were stimulated with 10 ng/mL of TNF $\alpha$  and 5 h later, the cells were harvested and lysed with passive lysis buffer (PLB, 100  $\mu$ L/well). The luciferase assays were performed according to the Promega Dual-Luciferase Reporter assay protocol, and luminescence produced by luciferase gene expression was measured by a luminometer (step 3). Figure 53 shows the schematic representation of luciferase assay.

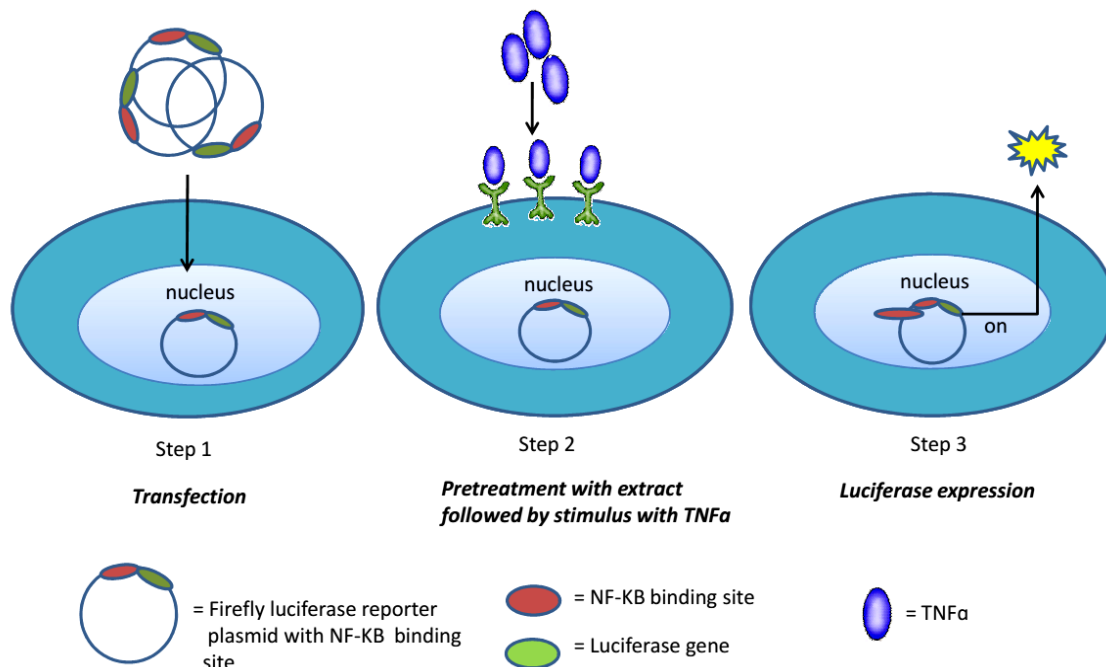


**Figure 53.** Schematic representation of luciferase assay.

#### 5.2.4. Preparing a standard curve for the *E. arvense* extract (anti-oxidant activity)

A DPPH radical stock solution was prepared by dissolving 25 mg of solid DPPH in 100 mL of absolute EtOH. A standard working solution was prepared by diluting the stock solution in absolute EtOH to give an absorbance of 1.3 at 519 nm. Standard test concentrations of *E. arvense* ethanol leaf extracts ranging from 5-25 µg/mL were prepared from a stock solution of the *E. arvense* extract (1 mg/mL) in 50% ethanol. For the analysis, 0.5 mL of the DPPH solution (absorbance 1.3) incubated with 0.5 mL of *E. arvense* extract standard test solution for 1 h. DPPH working solution 0.5 mL was mixed with 0.5 mL of 50% ethanol to serve as a blank. Decreases in the absorbance ( $\lambda$  519 nm) of DPPH radical solution in the presence of *E. arvense* extract was measured using UV-Vis spectroscopy.

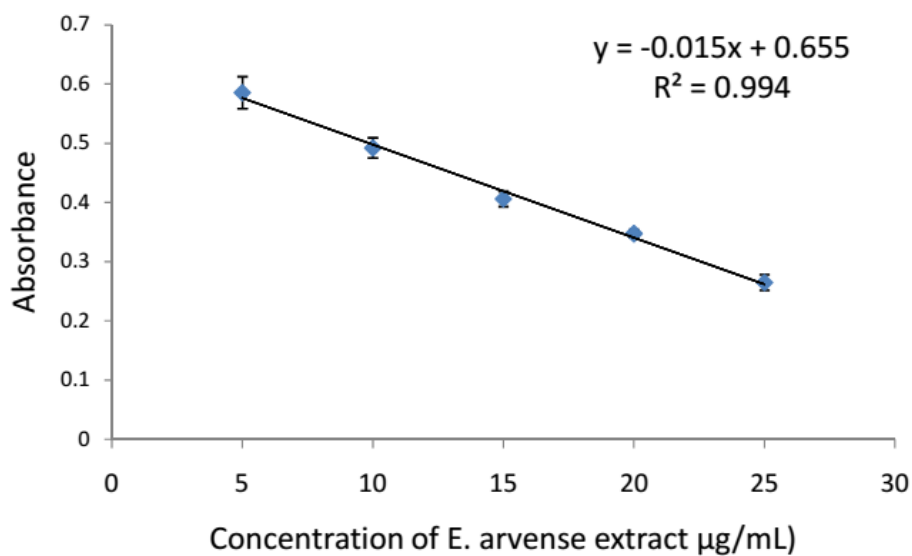


**Figure 54.** Standard curve developed by *E. arvense* ethanolic leaf extract by DPPH assay.

### 5.2.5. Preparing a standard curve for the *E. arvense* extract (anti-inflammatory activity)

Stock solution was prepared by dissolving 9 mg of *E. arvense* extract in 1 ml of 2% DMSO. Standard solutions of the extract were added to the wells to give final concentrations of extract per well ranging from 40-300 µg/ml. The luminescence observed from the expression of luciferase is recorded by a luminometer. Fig. 55 shows the standard curve with concentration of the extract plotted against the luciferase expression.

### 5.2.6. *In vitro* release of *E. arvense* extract from pSi microparticles

*In vitro* release of the *E. arvense* extract from the pSi particles was monitored by two assays: luciferase assay for release of anti-inflammatory compounds, and DPPH radical scavenging assay to measure the release of anti-oxidant compounds.

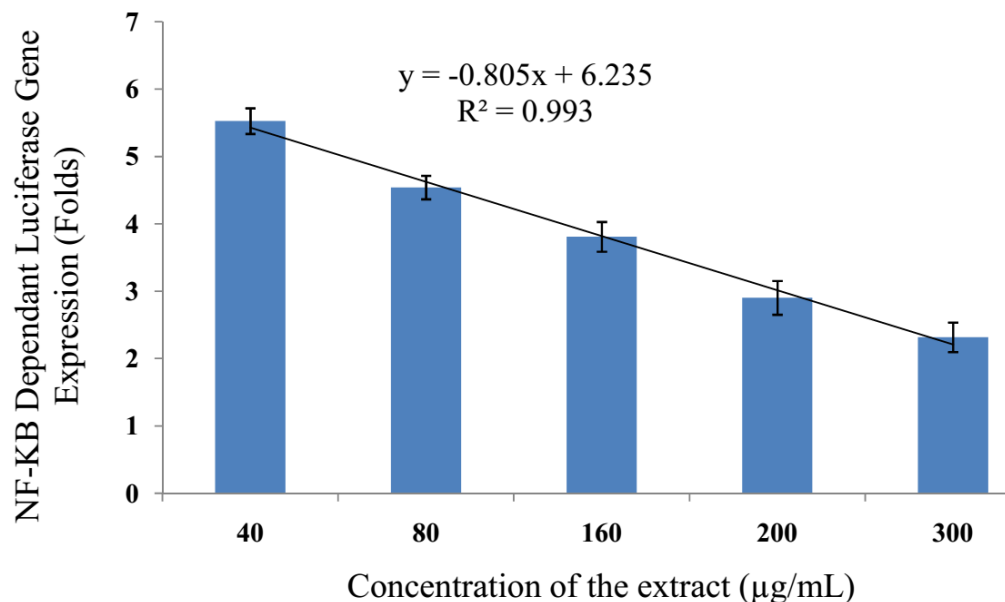


**Figure 55.** Standard curve developed by measuring the anti-inflammatory activity of known conc. of *E. arvensis* ethanol extract by luciferase assay.

#### 5.2.4.1. Release of anti-inflammatory compounds

pSi microparticles loaded with the *E. arvensis* extract (5 mg) and *E. arvensis* extract itself (1.5 mg) were placed in two different vials with 1 mL of sterilized water, and agitated at a speed of 30 rpm. At the end of a given time point, vials were centrifuged, supernatant was removed and replenished with 1 mL of fresh sterilized water. Supernatant containing the soluble extract (100 µL) was added to the 24 well plate seeded with a cell density of 10000 cells/well. The amount of anti-inflammatory compounds released from pSi and the extract itself at a chosen time period is below the detection limit of luciferase assay. So a standard addition method was used to bring the concentration levels within the range of standard curve. All the wells are treated with a known concentration of the extract (50 µg/mL). The actual amount of soluble extract released at a given time point was quantified in reference to a standard curve developed by luciferase assay.

#### **5.2.4.2. Release of anti-oxidant compounds**

pSi microparticles loaded with the *E. arvensis* extract (5 mg) was placed in a vial with 1 mL of water, and agitated at a speed of 140 rpm at 37 °C. At the end of given time point, pSi particles loaded with extract were centrifuged, supernatant was removed and replenished with 1 mL of fresh water. Amount of extract released at each time point is measured in reference to the standard curve developed by DPPH assay.

#### **4.2.6. Instrumentation**

Thermogravimetric analysis (TGA) was performed using a Seiko S II model SSC/5200TGA at a heating rate of 10°C/min (up to 400°C) under nitrogen. Differential scanning calorimetry (DSC) analysis was done using DSC 2 system (Mettler Toledo), sample was placed into Al pans with holes and heated from 25 to 400 °C at the rate of 10 °C/min, under nitrogen flush. X-ray diffraction was carried out using a Phillips 3100 X-ray powder diffractometer with Cu K $\alpha$  radiation operating at 35 kV. A Beckman DU-64 spectrophotometer was used for measuring the absorbance DPPH. Luciferase gene expression was measured by Berthold SIRUS II luminometer.

### **5.3. Results and Discussion**

#### **5.3.1. Loading of *E. arvensis* ethanol leaf extract into pSi**

pSi microparticles (1230±550 nm) derived from tabasheer powder were loaded with the *E. arvensis* ethanol leaf extract by solution load method. A mixture of solvents, ethanol, water, and DMSO, were used in the ratio of 2:2:1 by volume. DMSO was used as a co-solvent to enhance the concentration of extract in the solution. The extract was loaded into pSi with a theoretical loading of ~30% by weight. Thermogravimetric analysis (TGA) was used to analyze the loading



capacity of the extract into pSi microparticles. Single stage mass loss was observed between 25-350 °C, which includes evaporation of solvent mixture along with decomposition of the crude extract components (Fig. 56). It is assumed that TGA trace within this temperature range shows an underestimate of loading due to incomplete removal of decomposition products.

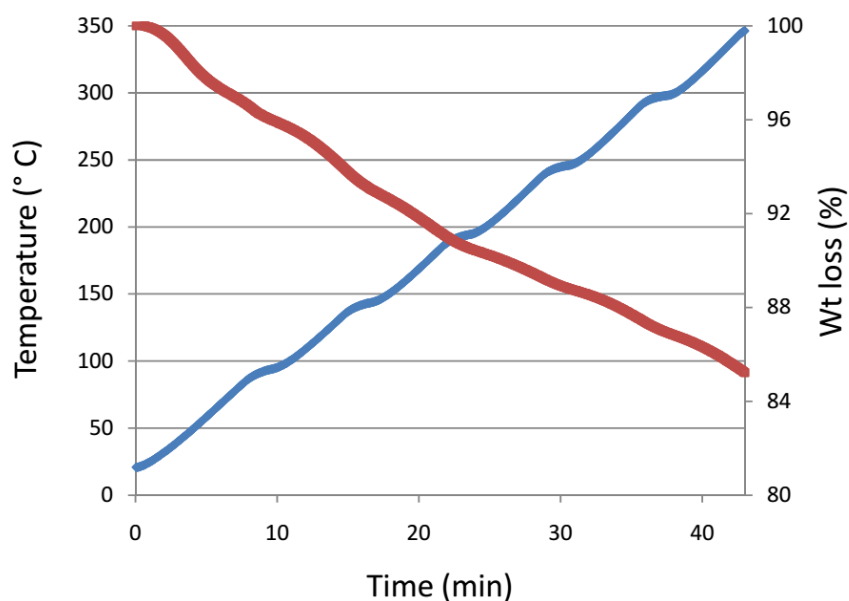


**Figure 56.** TGA analysis of *E. arvensis* extract loaded pSi particles by solution load method.

### 5.3.2. DSC analysis

Physical state of the extract after loading into pSi was evaluated by powder X-ray diffraction spectroscopy and differential scanning calorimetry (DSC). Major phenolic constituents of the *E. arvensis* are kaempferol and quercetin.<sup>163</sup> An overlay of DSC thermogram is shown in Fig. 57 for *E. arvensis* extract and extract loaded pSi. The DSC trace of *E. arvensis* extract shows two melting peaks in the range of 50-150 °C and 200-350°C. Melting within 50-150 °C can be attributed to evaporation of water or phytochemicals with low melting point. The second melting peak in the DSC trace within the range of 200-350 °C is likely a consequence of the melting of major phenolic constituents. Kaempferol and quercetin, with a melting point of

276 °C and 316 °C, respectively, falls within the melting range (200-350 °C) of this extract. From these observations, one can speculate that these two compounds are present in the *E. arvense* ethanol extract. After loading the extract into pSi, DSC thermogram shows a clear shift in the melting peak to a lower range. As discussed in Chapter 4, this phenomenon is attributed to the reduced crystallite size of the crystalline components in the extract as a consequence of pore confinement.

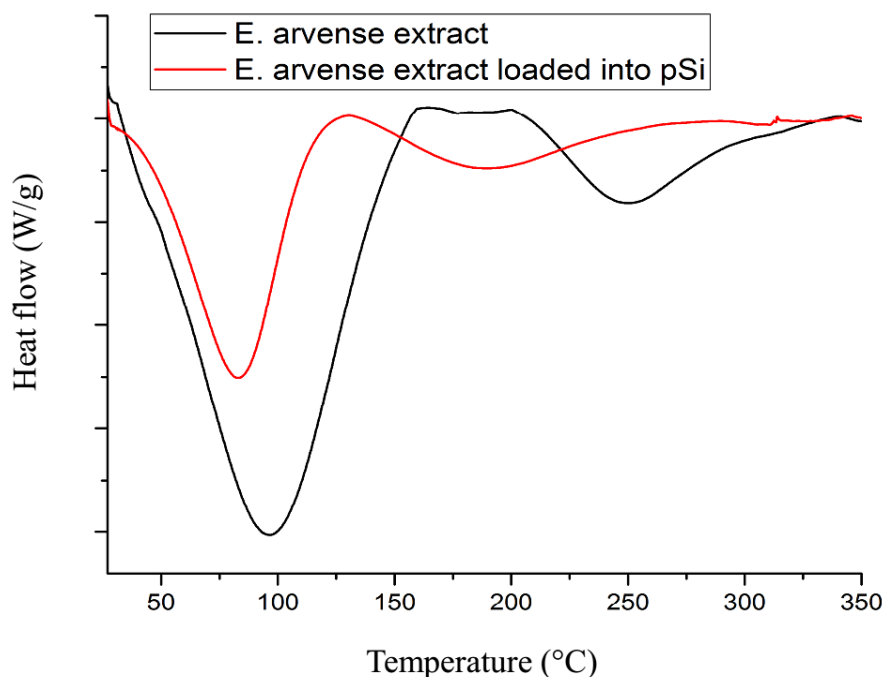


**Figure 57.** Overlay of DSC thermograms of *E. arvense* extract and this extract loaded into pSi.

### 5.3.3. XRD analysis

An overlay of XRD diffractograms (Fig. 58) obtained for pSi microparticles, crystalline *E. arvense* ethanol extract, and extract loaded into pSi (derived from tabasheer). The diffractogram of *E. arvense* extract alone with the most intensive peaks at 26°, 41°, 51°, 67° suggests its existence in a crystalline form. The absence of these peaks after loading into pSi microparticles suggests that some nanostructuring takes place upon its loading into the porous Si matrix.

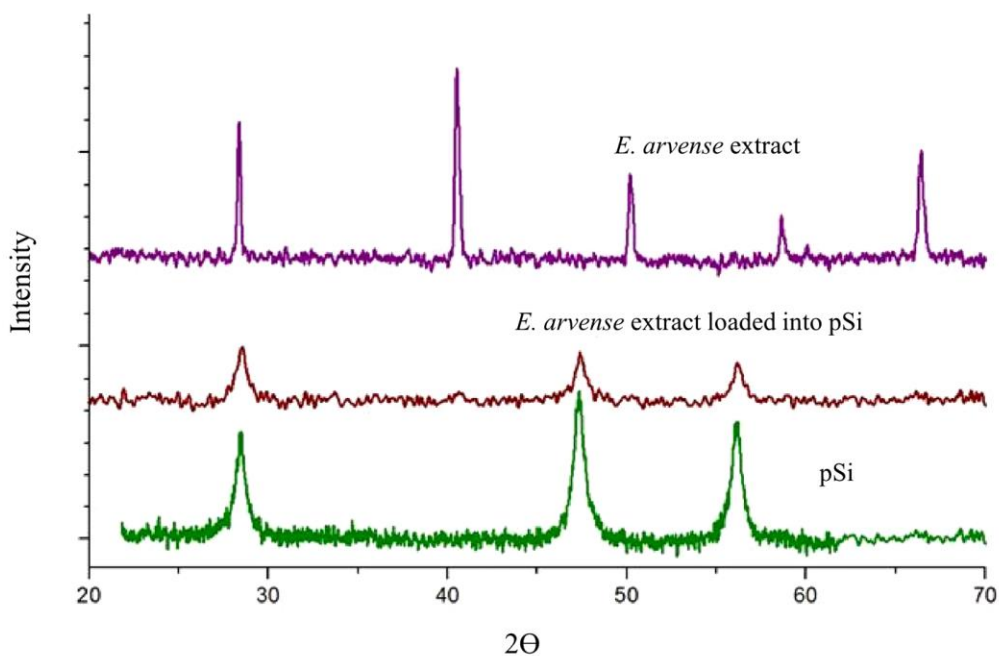


**Figure 58.** XRD analysis of *E.arvensis*, before and after loading into pSi microparticles.

#### 5.3.4. Release of anti-inflammatory compounds form pSi particles

*E. arvensis* is rich in polyphenolic compounds. In the literature it is reported that a variety of polyphenolic compounds has poor solubility in aqueous buffers.<sup>164</sup> Similar observations were noted while loading an *E. arvensis* extract into pSi particles. When the *E. arvensis* extract was first dispersed in water, the addition of organic solvents (ethanol and DMSO) greatly enhanced the solubility of the extract. *In vitro* release of the anti-inflammatory extract was monitored by luciferase assay. Fig. 59 shows the release profile of soluble extract and extract loaded into pSi. At a given time point the amount of the soluble extract released from pSi is higher than the extract itself. There is no notable difference (< 5%) between the amount of soluble extract released from pSi and just the extract itself at time points of 0.5 min and 1.5 min. This can be attributed to surface bound crystalline extract present outside of the pSi microparticles that has similar solubility profiles as that of the bulk crystalline extract. Any surface bound fraction present on pSi particles is either due to pore over filling or a recrystallized portion of the extract

that is present within the pores of Si microparticles. A notable difference (>10%) in the amount of soluble extract released from pSi and extract was observed at a later point of time from 3.5-143.5 min. This suggests that gradual release of the pore confined extract in its nanostructured form (from DSC, XRD) enhanced the solubility of the extract. At the end of 143.5 min, the cumulative release of the soluble extract from pSi is twofold higher than the just extract itself.

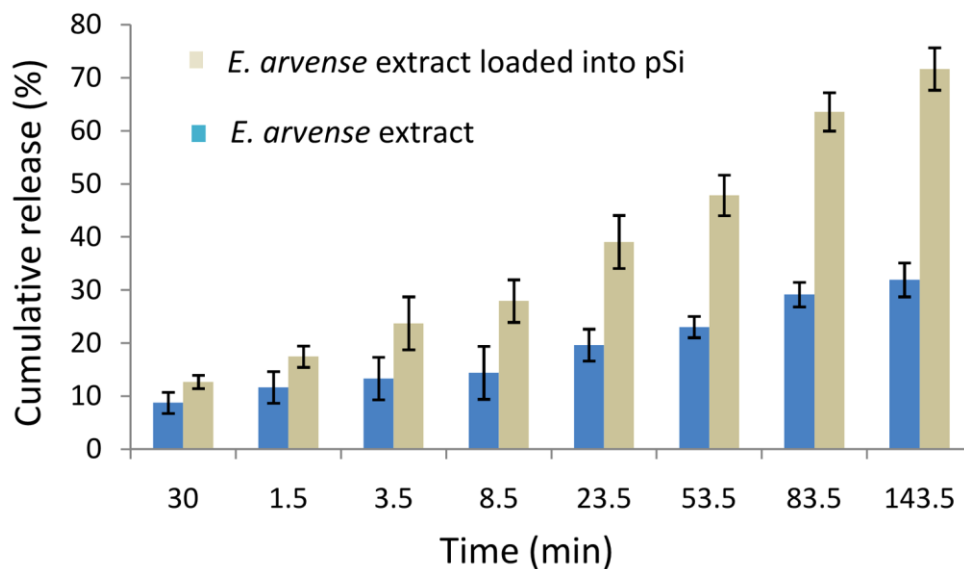


**Figure 59.** *In vitro* release of the anti-inflammatory components from pSi loaded with *E. arvensis* extract.

We also observed the anti-inflammatory activity of the released extract to explore the possible difference between the activity of the extract and extract loaded into pSi. As discussed in the experimental section, the amount of extract released at a given time point was treated with the HEK293 cells, and luciferase gene expression was measured using a luminometer. The limitation of the assay is that only 100  $\mu$ L of the extract released into the sterile water at a given time point is to be treated with the cells to minimize the dilution of growth medium for healthy cell growth. Minimum dose required (*E. arvensis*) to show anti-inflammatory activity by this assay is 40 $\mu$ g/mL. This means that every 100  $\mu$ L of the extract should contain at least 400  $\mu$ g of

the extract to show any observable anti-inflammatory activity. Due to the limitations of the assay protocol all the test samples collected at each time point are spiked with known concentration of the extract to clearly visualize the enhanced anti-inflammatory activity of the extract after loading into pSi.

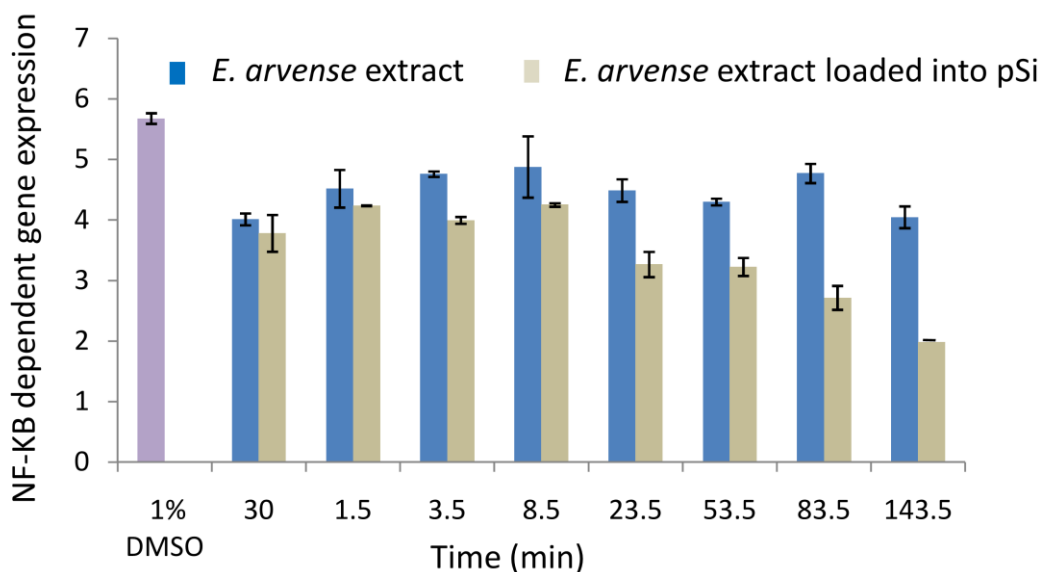


**Figure 60.** Anti-inflammatory activity of the *E. arvense* extract and extract loaded pSi powders. All the samples were spiked with (50  $\mu\text{g}/\text{mL}$ ) of *E. arvense* extract.

Fig. 60 shows the luciferase expression of released extract from pSi and extract itself. We used 1% DMSO treated HEK 293s as our control. Anti-inflammatory compounds should ideally decrease the luciferase expression by blocking NF-KB activation. We observed reduced luciferase gene expression compared to the control (1% DMSO), thereby showing the anti-inflammatory nature of the *E. arvense* extract. Enhanced anti-inflammatory activity was observed in case of extract loaded into pSi compared to just the extract itself at each time point. A notable difference (0.5 fold) in the anti-inflammatory activity was observed at time point (in the 3.5-143.5 min range), due to the likely enhanced solubility of the extract after loading into pSi.

### 5.3.5. Release of anti-oxidant compounds form pSi particles

We have evaluated the anti-oxidant properties of the *E. arvense* extract loaded pSi by its ability to scavenge the DPPH radicals. The amount of anti-oxidant compounds released from the extract at a given time point was determined in reference to the standard curve developed by DPPH assay. Fig. 61 shows the *in vitro* release of anti-oxidant components from pSi loaded with the *E. arvense* extract. Burst-type release profile within first few min (0.5-3.5 min), followed by gradual increase was observed. The burst release could be due to the presence of surface fraction of adsorbed extract on the pSi microparticles.

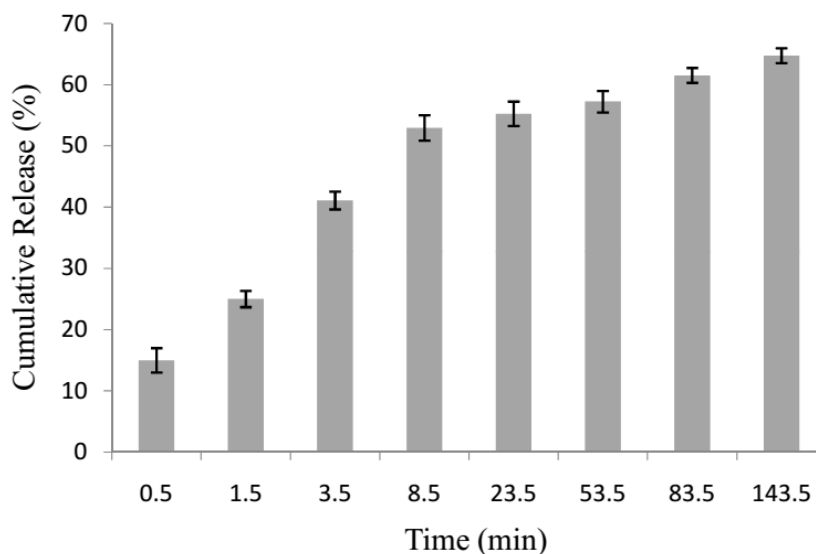


**Figure 61.** *In vitro* release of anti-oxidant components from *E. arvense* extract loaded pSi microparticles.

### 5.4. Summary

Overall in this study we have shown that pSi microparticles derived from tabasheer can serve as effective controlled release carriers to encapsulate and release polyphenolic components with poor aqueous solubility. The results from XRD and DSC measurements showed that *E. arvense* can be encapsulated into pSi in a more soluble form (presumably due to nanostructuring

of the extract components). This is a strikingly similar phenomenon to that observed in the case of pSi loaded with vitamin D3. These similarities indicate mesoporous morphologies of plant derived pSi microparticles are capable of loading either a single component or a complex multi component mixture (as in this case) in a more soluble form, thereby ideally enhancing their bio-availability.

## **Chapter VI**

### **Plant Derived Porous Silicon Nanoparticles for Gene Delivery**



## 6.1. Introduction

Current scientific advances in the bio-nanotechnology field facilitate engineering vectors that can deliver genomic material (a transferred gene, or transgene) to specific cells. These vectors can produce therapeutic effects by correcting an abnormality or transform a new function to the cells.<sup>165</sup> There are two major categories of vectors that can deliver genomic materials to targeted cells: viral and non-viral vectors. An ideal vector should be able to deliver gene of interest to the target cells without causing toxicity, and should successfully express genes sufficient enough to correct the pathological defects.<sup>166</sup>

Viral vectors have shown promising results, because of their efficiency of transfecting host cells is relatively high compared to non-viral vectors. Since 1989 over 2200 clinical trials were initiated for gene therapy, of which ~42% are based on viral vectors.<sup>167-169</sup> In 2017, the FDA has approved Kymriah (tisagenlecleucel), a viral vector based gene therapy for acute lymphoblastic leukemia making it the first gene therapy in the market for acquired disease.<sup>170</sup> The current price tag of Kymriah is ~\$475,000 (delivered as a one-time infusion). Although viral vectors have emerged as preferred vectors of choice, multiple issues are associated with this mode of delivery, including carcinogenesis, immunogenicity, broad tropism (lack of specificity to cells or tissue), limited DNA packaging capacity, high cost, and difficulty in vector production.<sup>171</sup> Recent advances in nanotechnology have led to the preparation of non-viral vectors to overcome these limitations with respect to safety, cost, ease of production, and potential to deliver larger genetic payloads.<sup>172</sup>

Non-viral vectors are categorized into synthetic and non-synthetic vectors. Among these non-viral systems, delivery of DNA in combination of physical methods (gene gun, electroporation, hydrodynamic delivery, sonoporation and magnetofection) comes under the non-

synthetic category.<sup>173</sup> The main challenge to deliver just the DNA itself is potential degradation of the therapeutic gene by endonucleases in the cytoplasm therefore low transfection efficiency. For this reason, entrapment of the DNA in a carrier is necessary in order to provide protection from endonuclease degradation, to improve blood circulation time, and transfection efficiencies.

Synthetic vectors are typically composed of inorganic nanoparticles, lipid-based, polymer-based and peptide-based materials. DNA can be incorporated into these vectors by three main strategies: electrostatic interaction, encapsulation, and adsorption.<sup>174</sup> The ultimate fate of these synthetic vector-DNA complexes depends on three biological factors: cellular internalization, endosomal escape and nuclear transport.<sup>173</sup> Once a given vector-DNA complex is internalized into the cytoplasm by endocytosis, it is directed to the late endosomal compartment where it will be degraded. Cationic lipids and cationic polymers have shown the ability to escape from the endosomal compartment, which helps in the unpacking of genomic material from the vector-DNA complex.<sup>175</sup>

Typical vector unpacking mechanisms shown by cationic lipids and cationic polymers were “flip-flop” mechanism, and “proton sponge effect” respectively (Figure 62(a) & 62(b)).<sup>176</sup> <sup>177</sup> Zelphati and Szoka proposed a “flip-flop” mechanism whereby the positively-charged lipoplexes (lipid-DNA complexes), once inside the endosomes, fuse to the negatively charged lipids found in the endosomal membrane due to electrostatic interactions. The anionic lipids of the endosomal membrane side diffuse along its length into the lipoplexes and form charge-neutralized ion pairs with the cationic lipids of the lipoplexes, thus displacing the DNA from the lipoplexes into the cytoplasm.<sup>176</sup>

Behr *et al.* initially observed the proton sponge effect of polyethylenimines (PEI) in PEI/DNA particles for its gene-delivery potential.<sup>177</sup> During the maturation of endosomes

(transformation to lysosomes), the membrane-bound ATPase proton pumps actively pumps protons from the cytosol into the endosomes, leading to the acidification of endosomal compartments.<sup>178</sup> Protonation of amine groups resist the acidification of endosomes which causes the ATPase proton pump to bring in more protons followed by passive entry of chloride ions, increasing ionic concentration and leading to water influx. Eventually the osmotic pressure causes swelling and rupture of endosomes, releasing their contents to the cytosol.<sup>177</sup>

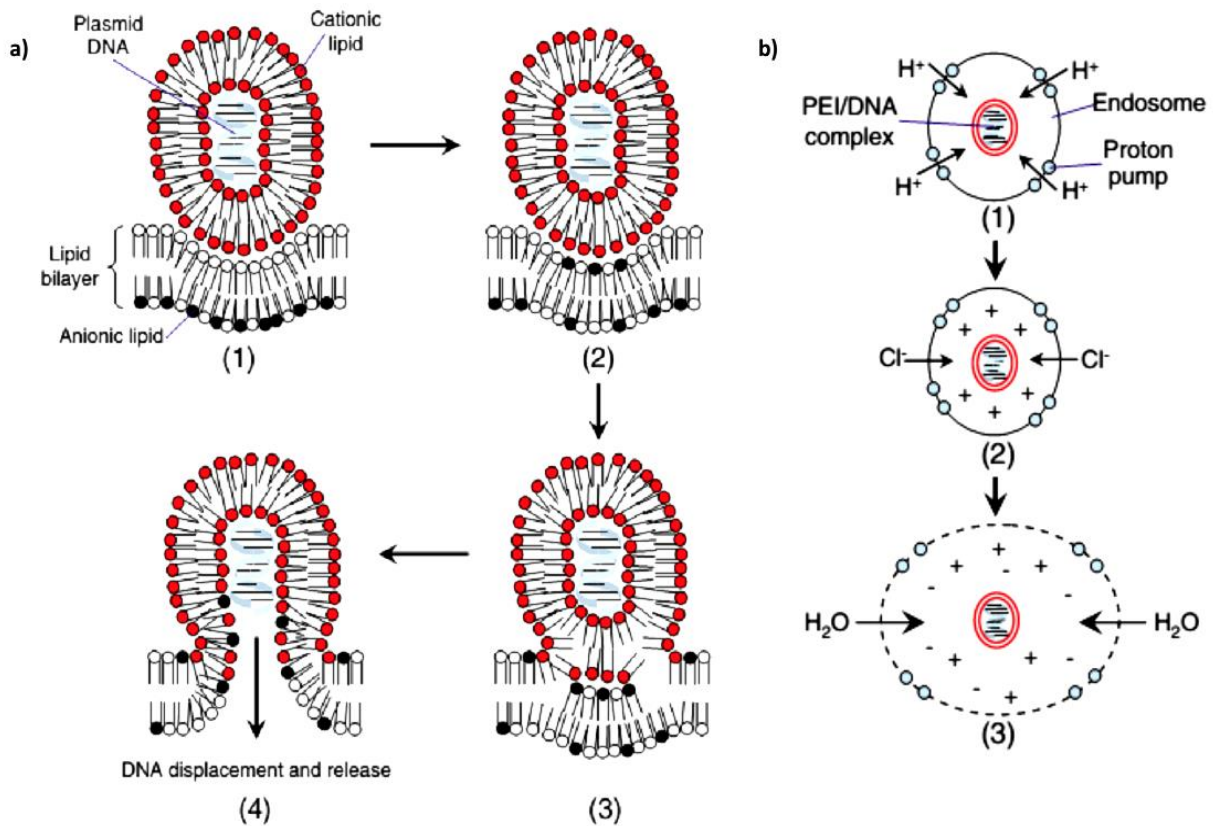


**Figure 62.** Mechanisms of endosomal escape. (a) Flip-flop. (b) Proton sponge. (Adapted from Refs. 176, 177).

Whether the escaped vector unpacks to release DNA or the total vector DNA complex enters the nucleus is still a question of debate. In the case of liposome vector based gene delivery, Zabner *et al.* demonstrated that DNA has to be freed from a liposome-DNA complex (lipoplex) before nuclear entry for optimal gene expression.<sup>179</sup> But in contrast, few cationic polymer based vector complexes (polyplexes) for example a PEI-DNA complex, remain complexed with the DNA after transport into the nucleus.<sup>180</sup>

In the absence of mitotic cell division, once the genomic material unpacks from the vector it will not remain free for long in the cytoplasm. The released genomic material can move along the cytoplasm and is transported to nucleus by association with a large number of cellular proteins that helps to interact with the microtubule network for movement toward the nuclear envelope where genomic material enters into the nucleus via nuclear pore complexes using a different set of proteins (importins).<sup>181</sup>

Many non-viral vectors are currently based on cationic polymers, cationic lipids or inorganic nanoparticle-cationic polymer hybrids. These systems have shown toxicity because of the strong association of their positive charge with the negatively charged cell membranes that leads to substantial damage of the cell membrane and even lead to destruction.<sup>182</sup>

Nanostructured silicon-based gene delivery systems are potential gene delivery systems because of their high surface to volume ratios, established surface chemistry, and low cytotoxicity. Kim *et al.* demonstrated the use of silicon nanowires in minimal invasive gene delivery directly to the nucleus.<sup>183</sup> Shen *et al.* developed nanoporous silicon microparticles functionalized with arginine-polyethyleneimine inside the nanopores for effective delivery of gene silencing agents (siRNA).<sup>184</sup> Tian *et al.* investigated the use of silicon nanotubes as a gene

(plasmid DNA) delivery vector.<sup>185</sup> Wearing *et al.* demonstrated the cell membrane binding ability of metal assisted stain etched porous silicon for *in vitro* delivery of plasmid DNA.<sup>186</sup>

As an alternative to conventional methods of porous silicon fabrication,(metal-assisted etching, and anodization of silicon wafers), we focused on deriving porous silicon nanoparticles (pSiNPs) using an eco-friendly magnesiothermic reduction of plant-derived silica. In our previous work we have shown that fabrication of pSi powders by magnesiothermic reduction yields high surface area materials with no trace metal impurities (Chapter 2).

In this chapter the ability of plant derived pSiNPs as gene delivery vehicles is evaluated. EF1-eGFP plasmid DNA (endothelial factor 1 enhanced green fluorescent protein, 6429 bp) is used as a reporter plasmid. To load plasmid DNA through electrostatic interactions, primary amine groups were introduced onto pSiNPs using 3-aminopropyltriethoxysilane (APTES) as a functionalized linker. Different mass ratios of pSiNP/DNA were initially evaluated to evaluate the binding capability of the pSiNPs to DNA in order to determine optimal transfection efficiencies. It is hypothesized that once the pSiNP-APTES-DNA complex internalizes into the cytoplasm; the released DNA from the complex should enter into the nucleus, undergoing transcription and translation to express eGFP.

## **6.2. Experimental**

### **6.2.1. Size reduction of porous silicon nanoparticles (pSiNPs)**

In a typical experiment ~0.8 g of Tabasheer powder (Bristol Botanicals Ltd.) milled for 2 days, at a speed of 80 rpm. The milled powder was calcinated and reduced using the protocol explained in Chapter 2 to obtain porous silicon. Sub-micron size porous silicon particles were obtained by fractional centrifugation (Fig. 63) of porous silicon powder at different time periods

( $t_1 = 30\text{s}$ ,  $t_2 = 30\text{s}$ ,  $t_3 = 30\text{s}$ ,  $t_4 = 300\text{s}$ ) to separate and obtain desired size of particles. Supernatant collected at each time point was further centrifuged until submicron size particles were obtained.

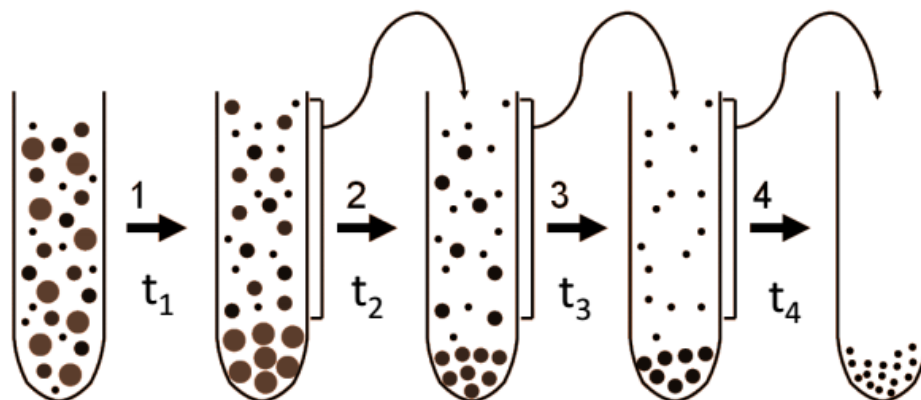


**Figure 63.** Size separation of porous silicon particles by fractional centrifugation.

### 6.2.2. Aminosilanization of porous silicon particles

pSiNPs (2 mg) were added to a 4% (v/v) solution of APTES in acetone (4 mL) and stirred for 6 h at a temperature of 40 °C (Fig. 64, Scheme a). The product (pSiNP-APTES) was collected by centrifugation, rinsed with acetone and allowed to dry in vacuum oven.

### 6.2.4. PEG functionalization of pSiNPs

pSiNPs (2 mg) functionalized with (3-aminopropyl)triethoxysilane (APTES) were dispersed in D.I water (2 mL). Next, a solution of poly(ethylene glycol) diacid 600 (3.3 mmol), EDC (1 mmol) and NHS (1 mmol) were prepared in 2 mL of water. The mixture was stirred for 15 min. Then 300 $\mu\text{g}$  of APTES functionalized pSiNPs was added to the mixture and stirred for 3 h at room temperature. Particles were washed with D.I water several times and dried in vacuum. The reaction scheme is shown in Figure 64b.

### 6.2.5. Complexation of DNA with pSiNPs and LyoVec

EF1-eGFP plasmid was used as a transgene to transfect cells with the enhanced green fluorescent protein gene. pSiNP-APTES and pSiNP-PEG were added to DNA at different mass

ratios to give pSiNP-DNA complexes (Fig.63c). In a typical experiment to 100  $\mu\text{g}$  of pSiNP-APTES dispersed in water, 1  $\mu\text{g}$  of DNA was added and incubated for 30 minutes. LyoVec (purchased from InvivoGen) is a commercially available cationic lipid-based transfection reagent, used as a positive control. It is composed of phosphonolipid DTCPTA (di-tetradecylphosphoryl-N,N,N-trimethyl methanaminium chloride) coupled with the neutral lipid DiPPE (1,2-diphytanoyl-sn-glycero-3-phosphoethanolamine). EF1-eGFP plasmid (1  $\mu\text{g}$ ) was added to 100  $\mu\text{l}$  of LyoVec and incubated for 30 min. EF1-eGFP, was made by Giri, Akkaraju, portion of the plasmid was derived from a plasmid made by Kim *et al.*<sup>187</sup>

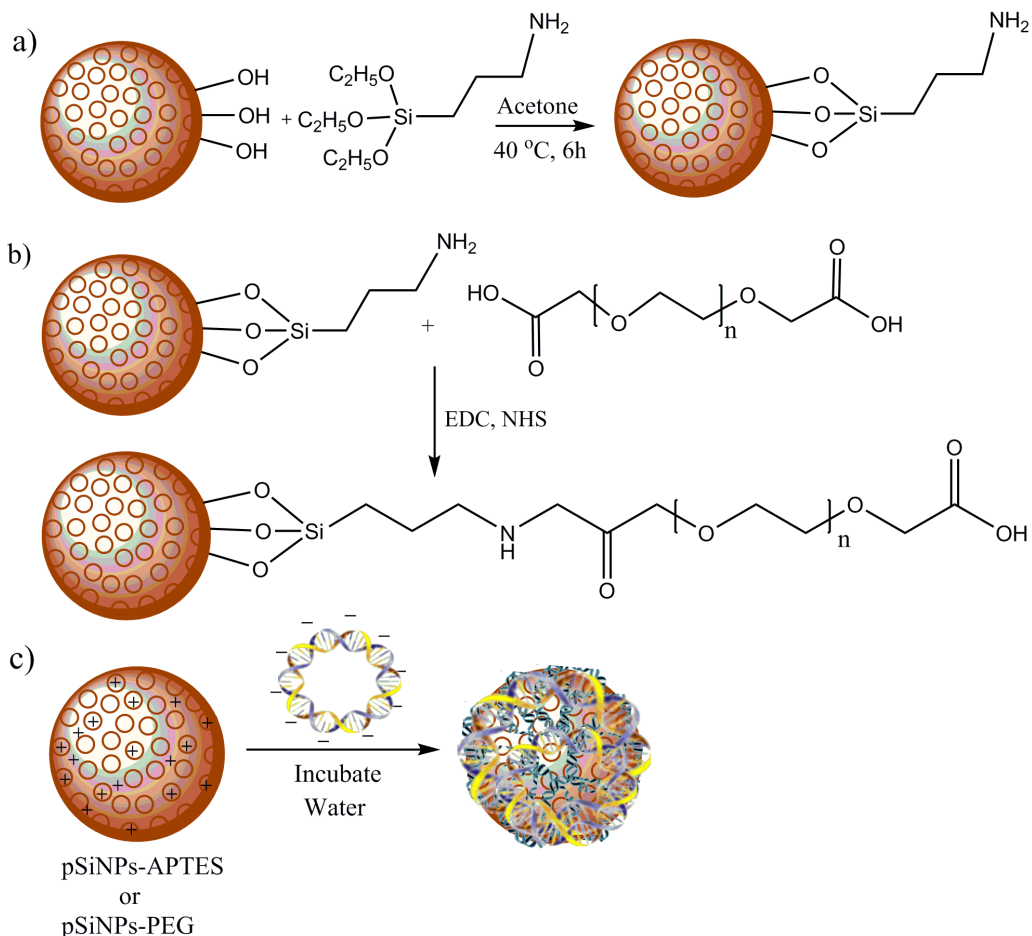


**Figure 64.** a) APTES functionalization of pSiNPs, b) PEG functionalization of pSiNPs c) DNA complexation of pSiNPs (pSiNP-APTES and pSiNP-PEG).

### 6.2.3. Quantifying number of amine groups

Ninhydrin reagent (0.35 % w/v) was prepared in ethanol. A glycine stock solution (1.1 mM) was used to generate a standard curve. A given amount of pSiNP was mixed with 500  $\mu$ L water and 1 mL ninhydrin reagent. The above solution was made upto 5 ml with ethanol. The mixture was heated at 60  $^{\circ}$ C for 20 minutes. Upon reaction of ninhydrin reagent with pSiNPs functionalized with APTES, purple color was observed. The particles were centrifuged for 15 minutes and the supernatant was analyzed with a UV-Vis spectrophotometer ( $\lambda=565$  nm).<sup>23</sup> The number of moles of amino groups on the surface of pSiNPs was calculated based on the standard curve of glycine (Fig. 65).

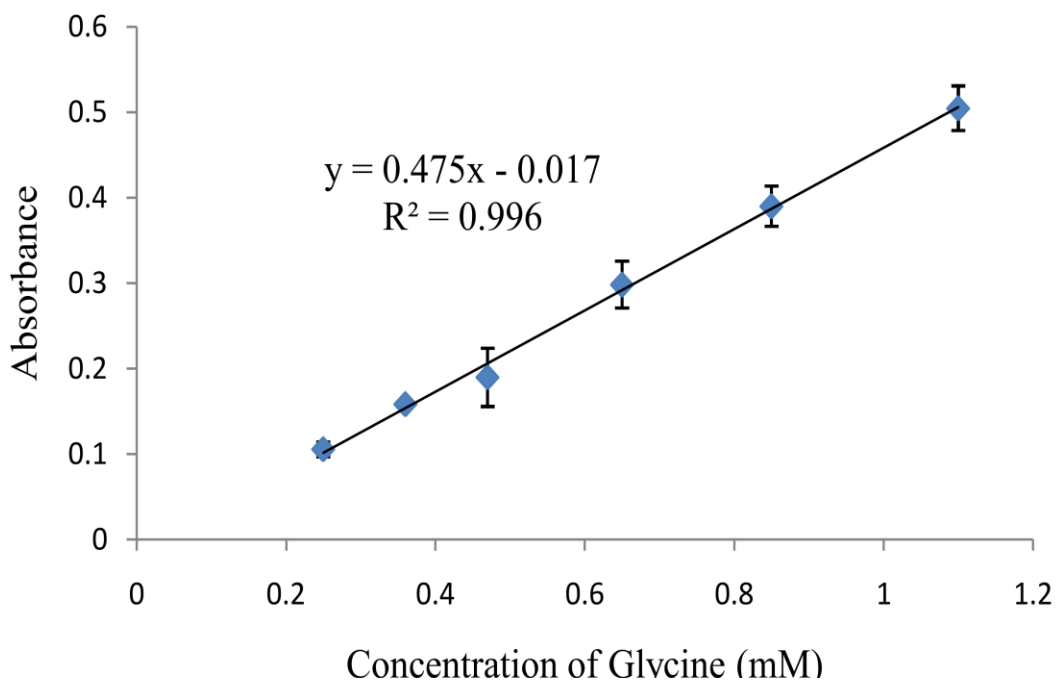


**Figure 65.** Standard curve obtained from ninhydrin-glycine colored complex at 565 nm.



### Calculation of number of NH<sub>2</sub> groups

Number of moles of amino groups on pSiNPs =  $0.3 \times 10^{-6} \text{ mol}$

Total number of amino groups =  $0.3 \times 10^{-6} \times 6.023 \times 10^{23}$

### Calculation of number of amino groups/ nm<sup>2</sup>

Surface area of pSiNPs =  $176 \times 10^{18} \text{ nm}^2/\text{g}$  (From BET analysis)

Surface area of 0.5 mg of pSiNPs =  $0.088 \times 10^{18} \text{ nm}^2$

Number of amino groups/nm<sup>2</sup> =  $\frac{0.3 \times 10^{-6} \times 6.023 \times 10^{23}}{0.088 \times 10^{18}}$

### 6.2.6. DNA encapsulation studies

The binding ability of pSiNP-APTES to plasmid DNA (EF1-eGFP) was studied using UV-vis spectrophotometry. After incubation of DNA with given amount of pSiNPs, the mixture was centrifuged for 3 min at 5000 rpm. The concentration of DNA ( $\lambda=260 \text{ nm}$ ) in the supernatant was measured using a spectrophotometer (NanoDrop 2000) by placing 1  $\mu\text{L}$  of supernatant on sample drop chamber. An extinction coefficient of ds DNA at the above wavelength =  $0.020 (\mu\text{g/ml})^{-1} \text{ cm}^{-1}$  was used to calculate concentration.

### 6.2.7. Transfection of HEK 293 cells

HEK 293 cells (0.5 mL) were placed at a seeding density of 10,000 cells per well on the sterilized glass slide and placed into incubator to allow the cells to settle for 30 minutes. After that 3.5 mL complete medium was added into each well. Cells were allowed to incubate at 37 °C with 5% CO<sub>2</sub> in air, in a humidified incubator for 24 h. Then cells were treated with just the DNA itself, pSiNPs, pSiNP-APTES-DNA complex, and LyoVeC-DNA complex. After a desired period of transfection, eGFP expression was monitored by fluorescence microscopy.

### **6.2.9. Instrumentation**

The morphologies of pSiNPs were characterized by transmission electron microscopy (TEM) JEOL TEM-2100 operating at 200 kV. A Beckman DU-64 spectrophotometer was used for measuring the absorbance of a given ninhydrin complex. Cells were counted manually using a Bright-Line Hemacytometer, and viewed under a Nikon Eclipse TS-100 inverted microscope and optical images were recorded using a Nikon CCD camera. Unbound DNA concentrations were analyzed using a NanoDrop spectrophotometer (ND2000). Zeta potentials were measured by Zetasizer Nano ZS. eGFP expression was imaged using a fluorescence microscope (Zeiss Axiovert 200).

## **6.3. Results and Discussion**

### **6.3.1. TEM analysis of pSiNPs**

Tabasheer powder with a particle size of  $25\pm 15\ \mu\text{m}$  was used as precursors to make submicron size particles. After an optimized milling process the size of tabasheer powder has reduced down to  $1230\pm 550\ \text{nm}$  (Fig. 66a) [as discussed in the Experimental Section]. The milled tabasheer powder was calcinated and reduced to pSi using magnesiothermic reduction. The reduced pSi powder was centrifuged several times to get a particle size of  $620\pm 270\ \text{nm}$  (t<sub>4</sub>, Fig. 66b). From EDX analysis of the pSiNPs ( $620\pm 270\ \text{nm}$ ) shown in Fig. 67 a), it is evident that the final product obtained from magnesiothermic reduction reaction is ~99% pure with no measurable traces of magnesium. High resolution HRTEM images reveal the presence of small nanocrystals embedded in an amorphous matrix as shown in Fig.66 b), lattice spacing distance of 0.310 nm associated with the Si (111), FFT (Fast Fourier Transform, Fig. 66b inset) diffraction pattern is consistent with a polycrystalline orientation (as discussed in Chapter 2).

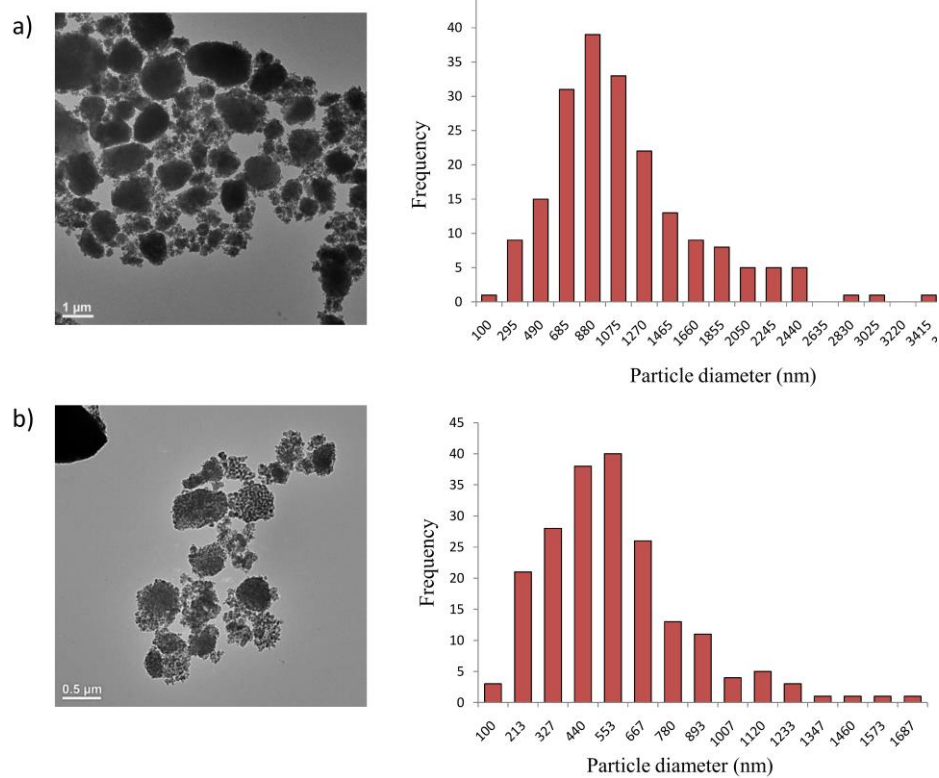


**Figure 66.** a) TEM image and corresponding size distribution of tabasheer powder after milling ( $1230 \pm 550$  nm). b) TEM image and corresponding size distribution of pSiNPs derived from the milled tabasheer ( $620 \pm 270$  nm).

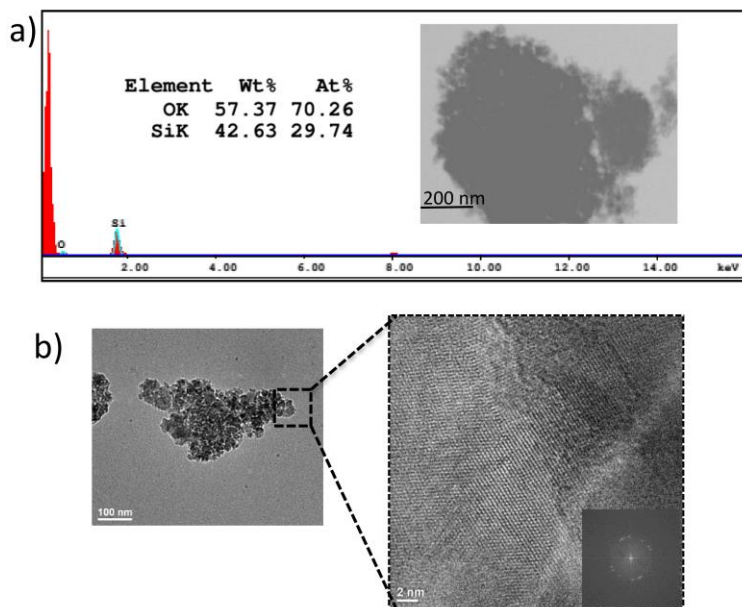


**Figure 67.** a) EDX analysis of pSiNPs derived from milled tabasheer. b) HRTEM images of pSiNPs showing lattice spacing of crystalline Si corresponding to Si (111) lattice planes.

### 6.3.2. Surface modification and DNA binding studies

pSiNPs were functionalized with 3-aminopropyl-triethoxysilane (APTES) in order to immobilize or conjugate plasmid DNA. The alkoxy silanes form covalent Si-O-Si bonds with hydroxyl groups on native oxide rich pSiNPs leaving (protonated) primary amine moieties ready to bind with DNA. Due to electrostatic interactions the positively charged reactive primary-amine moieties (dispersed in D.I water) can bind with negatively charged plasmid DNA. Quantified amine groups based on positive ninhydrin test is 2 amine groups/nm<sup>2</sup> (Experimental section). Number of amino groups calculated Zeta potential measurements further confirmed the presence of amine groups on pSiNPs. As shown in Figure 68, the typical zeta potential of (as-prepared) pSiNPs was  $-15.43 \pm 0.53$  mV consistent with negatively charged surface silanol groups while APTES modified pSiNPs was  $+11.57 \pm 0.42$  mV due to the positively charged amino groups on pSiNPs.

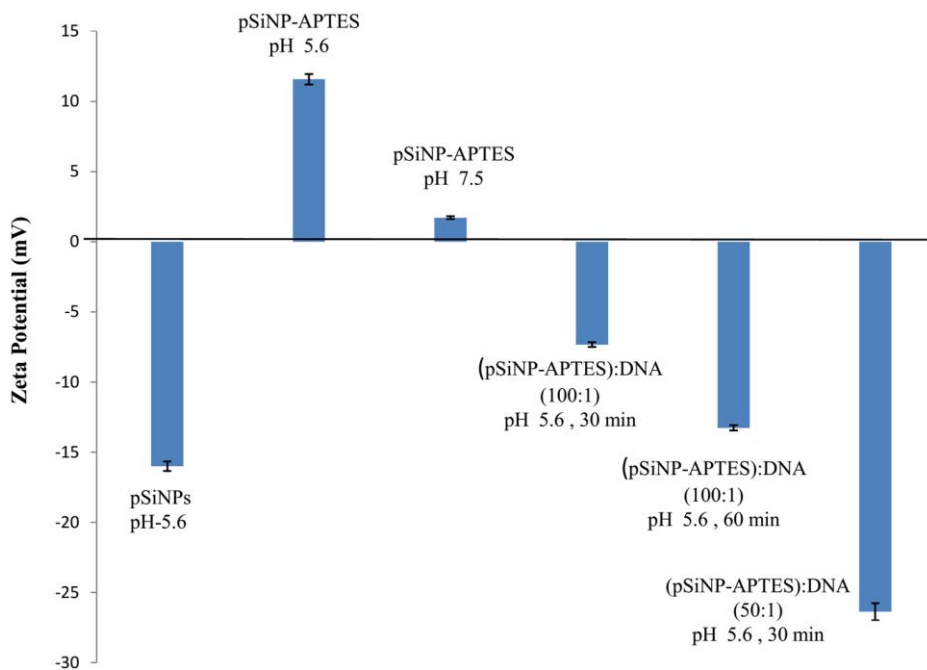


**Figure 68.** Zeta potentials of the pSiNPs, pSiNP-APTES, and pSiNP-APTES-DNA complexes.

At a weight ratio (pSiNP-APTES: DNA) of 100:1, with 30 min incubation, the zeta potential of the pSiNP-APTES-DNA complex decreased to -7.34 mV, presumably due to the binding of DNA with pSiNPs (Fig. 68). The zeta potential of the solution further decreased to -13.37 mV with an increased incubation time of 60 min. Using a weight ratio (pSiNP-APTES: DNA) of 50:1, with 30 min incubation, results in a more negative zeta potential of -26.37 mV. Increased efficiency of bound DNA could be the reason for decreased surface potential.

**Table 6.** Plasmid DNA loading capacities at various weight ratios of pSiNP-APTES/DNA, and incubation times.

Test sample	Incubation time	Added amount of DNA	Conc. Of DNA in supernatant	Encapsulation efficiency
(pSiNP-APTES):DNA (100:1)	30 min	10 ng/ $\mu$ L	2.7 ng/ $\mu$ L	61 $\pm$ 2%
(pSiNP-APTES):DNA (100:1)	60 min	10 ng/ $\mu$ L	2.9 ng/ $\mu$ L	58 $\pm$ 1%
(pSiNP-APTES):DNA (50:1)	30 min	10 ng/ $\mu$ L	4.1 ng/ $\mu$ L	70 $\pm$ 4%
LyoVec	30 min	10 ng/ $\mu$ L	0	100%

This behavior was investigated in further detail by studying the encapsulation ability of pSiNP-APTES to plasmid DNA by UV-Visible spectrophotometric analysis. As shown in Table 6, the plasmid DNA concentration in the supernatant (excess DNA) can be observed at different weight ratios of pSiNP-APTES/DNA, which suggests that DNA was able to bind to pSiNP-APTES nanoparticles. There is no big change in encapsulation efficiency with longer incubation time with same pSiNP-APTES/DNA ratios. This suggests that with pSiNP-APTES: DNA with a 100:1 weight ratio has reached a saturation (loading by electrostatic interaction). Whereas in case of pSiNPs-APTES: DNA ratio of 50:1 (increased DNA amount), showed higher loading

efficiency of 70%. This suggests along with electrostatic interaction, excess plasmid DNA has bound to pSiNPs by non-specific adsorption (bound inside pores).

### 6.3.3. Transfection experiments

The gene transfection experiments were done in a 6 well plate, cells (HEK 293) were seeded with a density of 10000 cells/ well. Wells were treated with naked DNA, pSiNPs, pSiNPs-APTES (negative control), pSiNP-APTES-DNA (test sample), and LyoVec-DNA (positive control). eGFP expression was observed for for 24 h, 48 h and 72 h. The transfection efficiencies were measured using Image J software based on taking the ratio of pixels associated with the area of fluorescent cells to the total area associated with fluorescent and non-fluorescent cells

Figure 69(a) shows internalization of individual pSiNPs into the cells with less aggregation after 48 h, with some particles bound to cell membrane and some were internalized. Figure 69(b) shows internalization of pSiNP-APTES particle aggregates. Figure 69(c) shows pSiNP-APTES-DNA complexes internalized into the cells with expression of eGFP after 48 h of transfection. Considerable particle aggregation is observed in case of pSi-DNA complexes as well.

Aggregation of the particles can be attributed to the lowered surface charge (zeta potential -7.4 mV) on the particles (pSiNP-APTES) after addition of plasmid DNA. Even though the pSiNP-APTES particles have a positive potential of +11.47 (measured in water), aggregation of pSiNP-APTES particles is likely a consequence of the spontaneous adsorption of serum proteins on to the surface after suspended in DMEM complete medium with 10% fetal bovine serum.

pSiNP-APTES-DNA complex (dispersed in 250  $\mu$ L) with a ratio of 100:1 showed a broad range of transfection efficiencies ( $23\pm 11\%$ ) after 48 h transfection (Fig. 70). In contrast the positive control LyoVec showed a transfection efficiency of  $65\pm 30\%$  after 48 h (Fig. 71).

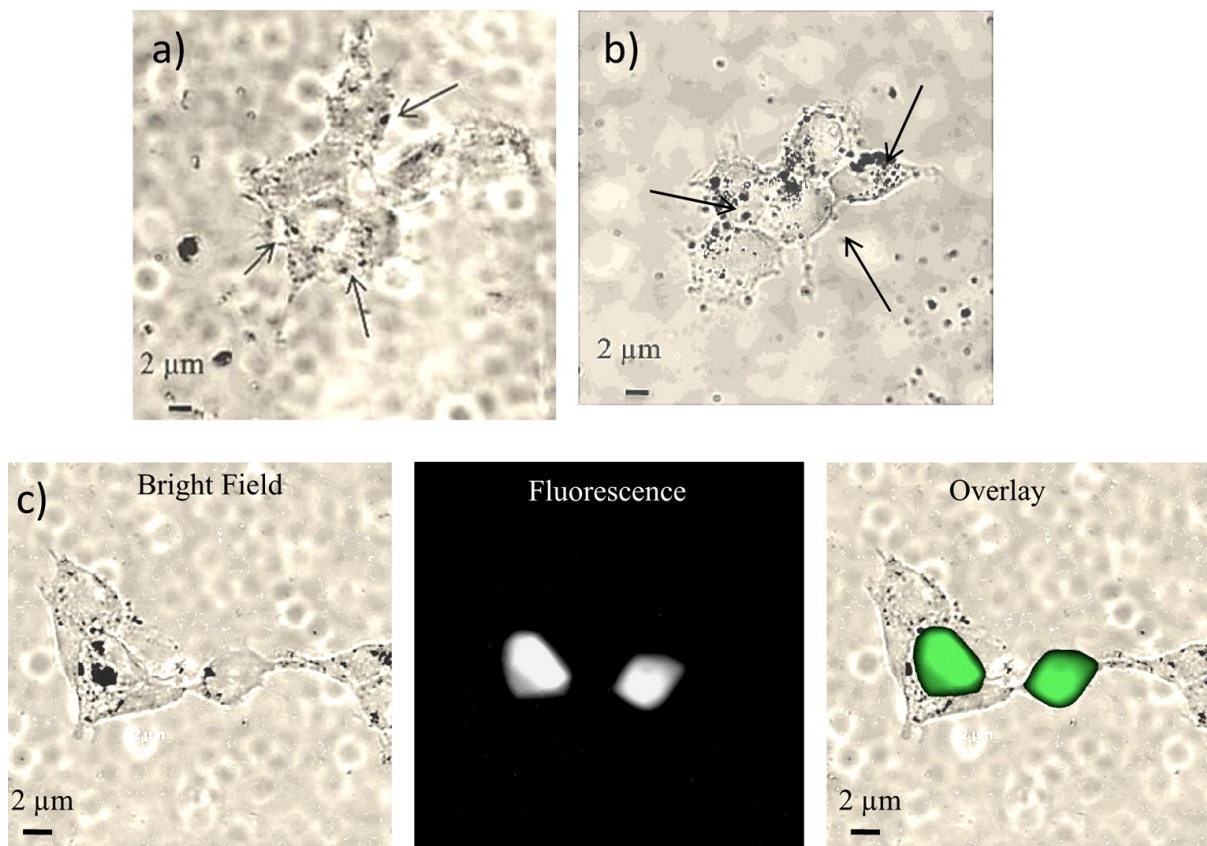


**Figure 69.** Internalization of a) pSiNPs (arrows indicate internalized pSiNPs), b) pSiNP-APTES (arrows indicate aggregates of pSiNPs) c) pSiNP-APTES-DNA complexes into HEK 293 cells after 48 h transfection.

Low expression of fluorescence ( $< 1\%$ ) was observed in case of PEG functionalized pSiNPs with a terminal carboxylate moiety. This is expected because of the PEG diacid with negatively charged surface carboxylate groups has low binding efficiency towards negatively charged plasmid, which further explains the low gene expression levels.



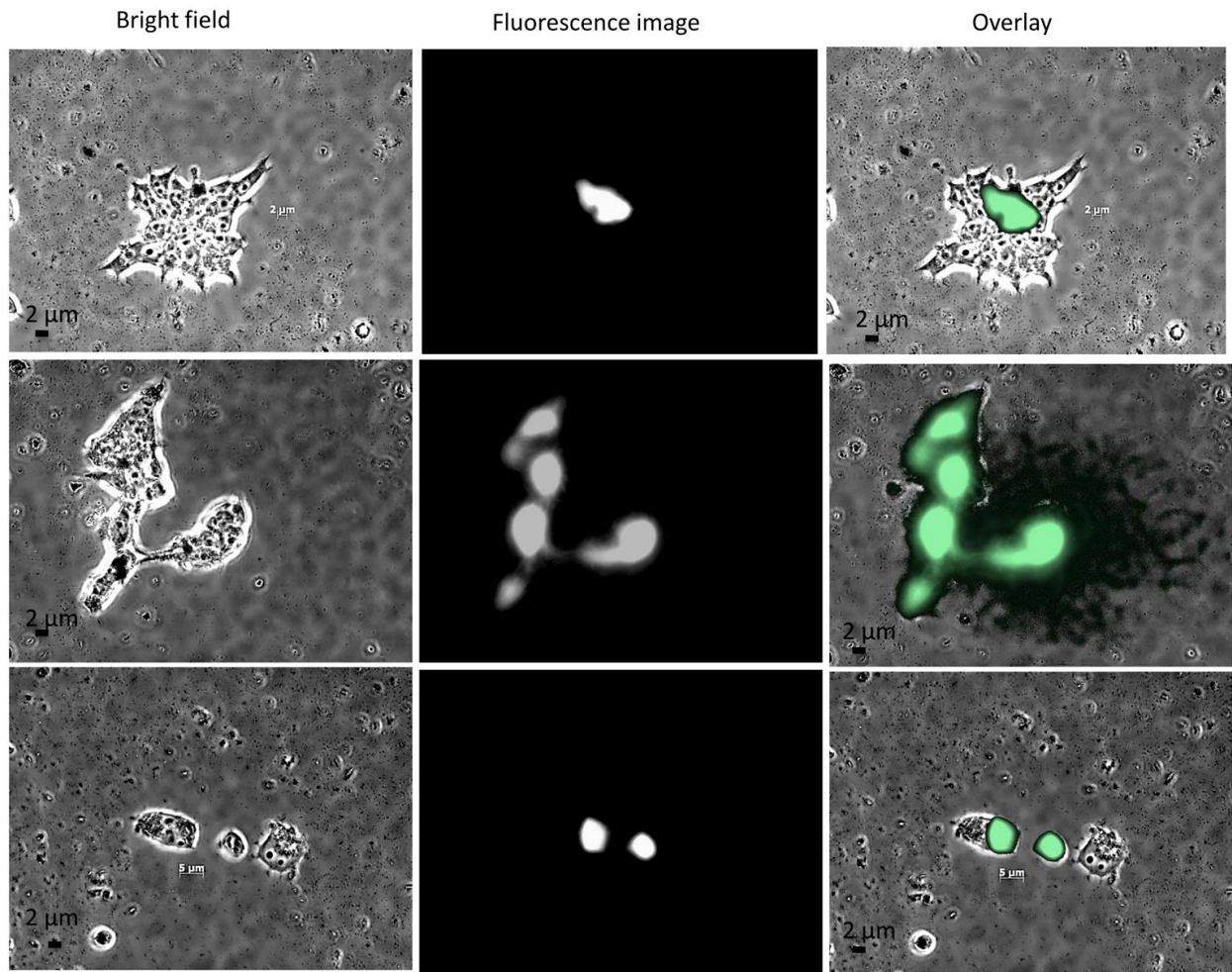


**Figure 70.** HEK 293 cells treated with pSiNP-APTES-DNA complex with a ratio of 100:1, expressed eGFP after 48 h transfection.

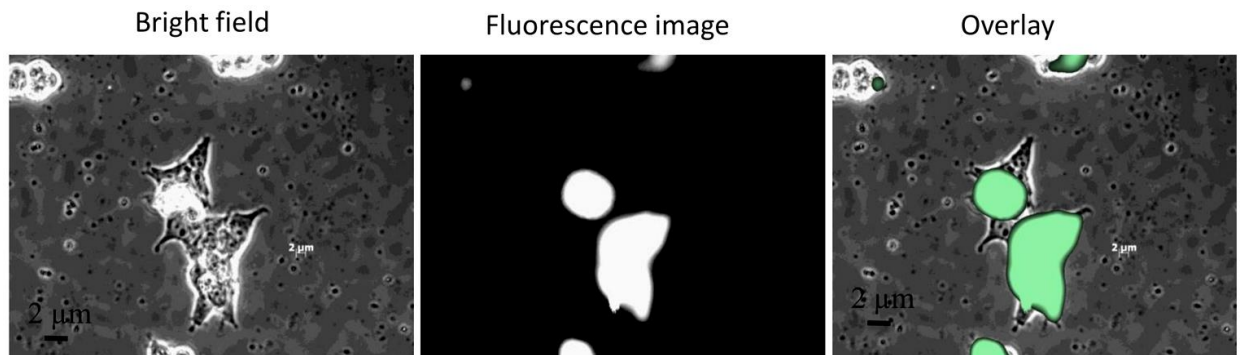


**Figure 71.** HEK 293 cells treated with LyoVec-DNA complex, expressed eGFP after 48 h transfection.



According to the previous studies it has been reported that amine derivatized pSi particles up to 600-1000 nm were endocytosed by non-phagocyte cells.<sup>184,188</sup> Our results suggested that pSiNPs were successfully functionalized with APTES. According to the literature suggestions, pSiNP-APTES particles of  $\sim 620 \pm 270$  nm size were able to internalize into the cells by endocytosis because of their size and surface charge.

Cationic polymers and lipid based systems such as LyoVec show higher transfection efficiencies, but it should be emphasized that the net positive charge after complexation with DNA will lead to adsorption of LyoVec-DNA complexes to non-targeted cells of interest and this causes toxicity due to cell membrane disruption.<sup>182</sup> In our case pSiNPs after complexation with DNA showed a net negative charge, and this could potentially reduce the positive charge based cytotoxicity to the cells. Internalized pSiNP-APTES-DNA complexes successfully expressed eGFP after 48 h.

So far, no studies have been carried out on detailed mechanisms of plasmid DNA release from silicon/silica based non-viral vectors. Degradation kinetics of the pSi carrier is slow in case of plant derived porous silicon (discussed in Chapter 2) and surface functionalization with APTES further reduces it.<sup>58</sup> So pSi degradation based release of DNA is presumably not the major release mechanism of DNA from the complex. It has been showed that DNA can be released from the vector-DNA complex because of its competitive interaction with other serum and cytoplasm proteins.<sup>181</sup> Based on these literature reports, we infer that DNA release from the pSiNP-APTES-DNA complexis due to slow diffusion of DNA from the pores as well as competitive interaction of pSiNP-APTES with cytoplasmic proteins. From the transfection results it is clear that plant derived porous silicon nanoparticles were able to express eGFP within 48 h, suggesting that these are promising candidates as non-viral gene delivery vectors.

#### 6.4. Summary

In this chapter, a detailed study of the plant derived porous silicon particle fabrication, size reduction, surface modification, and gene transfection was carried out. We have successfully modified the surface of these pSiNPs with APTES. We have shown that these alkoxy-silane modified pSiNPs have high encapsulation efficiencies for plasmid DNA due to electrostatic interactions. Cytotoxicity studies of the pSiNPs are under progress. *In vitro* transfection experiments suggest that pSiNPs could efficiently transfect plasmid DNA into HEK 293 cells and express eGFP within 48 hours. Further investigations are necessary, likely involving additional surface functionalization and further experiments to determine the proper ratio of DNA to pSiNPs with the long-term goal of achieving even higher transfection efficiencies.

## **Chapter VII**

### **Concluding Remarks**

With a primary focus on the economy and simplicity in fabrication, we have presented an eco-friendly fabrication route as an alternative to conventional etching methods for preparing pSi particles of high purity in competitive yields, possessing high surface areas as well. We have evaluated the ability of these nanostructured pSi particles for drug and gene delivery applications.

In Chapter I, different fabrication methods to create pSi particles were discussed. Key aspects of fabrication methods including experimental setup, porous silicon formation mechanisms, tuning the porosities were highlighted. Initial studies on biocompatibility and biodegradability nature of pSi particles along with some of the commonly used surface functionalities to tune the biodegradability were briefly discussed. Some of the key studies on use of pSi as a drug delivery carrier, biosensor, and in tissue engineering applications were presented.

In Chapter II, we have shown that silicon accumulator plants *Bambuseae* (tabasheer) and *E. telmateia* as cost effective feedstocks to create high surface area pSi microparticles. Our eco-friendly fabrication route involving magnesiothermic reduction resulted in competitive yields, 70% conversion of silica to silicon in case of tabasheer, and 60% in case of horsetail with a purity of ~99% (no measurable magnesium silicate phases). BET analysis showed formation of high surface area (180 m<sup>2</sup>/g) pSi powders from tabasheer derived pSi with an average pore diameter of 11 nm. Nanostructured features of pSi evaluated by TEM analysis showed presence of small Si crystallites (4-8 nm) embedded within the amorphous matrix. XRD, and Raman analysis further supported the crystalline nature of Si present within these highly oxidized pSi skeletons. Our preliminary studies on *in vitro* degradation of tabasheer derived pSi showed 50% degradation within 8 weeks. Our studies shows that, use of silicon accumulator plants or

agriculture waste as cost effective feedstocks to create high surface area pSi particles with high purity in competitive yields makes it an economical eco-friendly alternative for electrochemically etched pSi powders. However more studies involving tuning of wide range of degradation kinetics of plant derived pSi powders is needed to use them for variety of *in vitro/in vivo* applications.

In Chapter III, we have shown that a single plant (*Bambuseae arundinacea*), can yield bioactive components (antibacterial) as well as drug delivery carrier (pSi). pSi particles loaded with *Bambuseae arundinacea* ethanolic leaf extract showed a loading capacity of 25% by weight. Subsequent chromatographic separation of this extract revealed that the active antimicrobial species present include stigmasterol and 2,6-dimethoxy-p-benzoquinone. *In vitro* studies on the sustained release of the antibacterial components from the pSi carrier matrix showed prolonged antibacterial activity for a period of > 2 weeks, measured by disc diffusion assay. From our studies, it is clear that the dual advantage of the single plant source for creating this type of drug delivery carrier matrix would be an ideal low-cost option for countries with extensive resources of silicon accumulator plants in future synergistic drug delivery applications.

In Chapter IV, and V with a goal to increase the bioavailability of poorly dissolvable vitamins and plant based polyphenolic compounds we have loaded them into plant derived pSi microparticles. In both cases DSC and XRD measurements showed that these components are encapsulated into pSi in a more soluble form (due to nanostructuring of crystalline compounds). This in turn resulted in resulted in enhanced solubility of entrapped compounds. *In vitro* cumulative release profile of vitamin D3 showed enhanced solubility of the vitamin by ~9 times in case of melt loaded vitamin D3, ~11 times in case of incipient loaded vitamin D3 compared to just the vitamin itself. In case of polyphenolic compounds extracted from *E. arvense*, after

loading these compounds into pSi, enhanced their solubility which resulted in enhanced anti-inflammatory activity measured by luciferase assay.

In Chapter VI, optimization of size reduction process of plant derived pSiNPs, surface modification pSiNPs by APTES and PEG, and gene transfection experiments using pSiNP-DNA complexes were detailed. For effective loading of negatively charged DNA, we have modified the surface of pSiNPs with APTES. DNA loaded with pSiNP-APTES complex with a ratio of 100:1 (by mass) with a 30 min incubation time showed a high encapsulation efficiency of 60%. *In vitro* transfection experiments suggest that pSiNPs efficiently transfected plasmid DNA into HEK 293 cells and expressed eGFP within 48 h with a transfection efficiency of 23±11%. More studies involving the optimization of proper ratio of DNA to pSiNPs are needed to increase the transfection efficiencies.

Overall, the data obtained from these experiments sets the stage for further investigations of this material *in vitro* and ultimately of possible therapeutic value *in vivo*.

## VIII. References

1. Uhlir, A. *Bell Syst. Tech. J.* **1956**, *35*, 333–347.
2. Imai, K. *Solid-State Electron.* **1981**, *24*, 159–164
3. Watanabe, Y.; Sakai, T. *Rev. Electron. Commun. Lab.* **1971**, *19*, 899.
4. Lehmann, V.; Gosele, U. *Appl. Phys. Lett.* **1991**, *58*, 856–858.
5. Canham, L.T. *Appl. Phys. Lett.* **1990**, *57*, 1046–1048.
6. Canham, L.; Cox, T.; Loni, A.; Simons, A. *Appl. Surf. Sci.* **1996**, *102*, 436–441.
7. Kolasinski, K.W. *Porous Silicon for Biomedical Applications*; **2014**, Woodhead Publishing, London, 52–80.
8. Jane, A.; Dronov, R.; Hodges, A.; Voelcker, N. H. *Trends Biotechnol.* **2009**, *27*, 230–239.
9. Canham, L. T. *Handbook of Porous Silicon*; **2014**, Springer International Publishing, Switzerland, 255-262.
10. Canham, L. T. *Nanotechnol.* **2007**, *18*, 185704-185708.
11. Canham, L. T. *Handbook of Porous Silicon*, **2014**, Springer International Publishing, Switzerland, 3-8.
12. Rouquerol, J.; Avnir, D.; Everett, D. H.; Fairbridge, C.; Haynes, M.; Pernicone, N.; Unger, K. K. *Stud. Surf. Sci. Catal.* **1994**, *87*, 1–9.
13. Rouquerol, J.; Rouquerol, F.; Llewellyn, P.; Maurin, G.; Sing, K. S. *Adsorption by Powders and Porous Solids: Principles, Methodology and Applications*; **2013**, Academic Press, 1–25.
14. Rouquerol, J.; Avnir, D.; Fairbridge, C. W.; F.; Everett, D. H.; Haynes, J. H.; Pernicone, N.; Ramsay, J. D.; Sing, K. S.; Unger, K. K. *Pure Appl. Chem.*, **1994**, *66*, 1739–1758.
15. Loni, A. *Handbook of Porous Silicon*, **2014**, Springer International Publishing, Switzerland, 11-20.
16. Pace, S.; Vasani, R. B.; Cunin, F.; Voelcker, N. H. *New J. Chem.* **2013**, *37*, 228–235.
17. Lehmann, V. *J. Electrochem. Soc.* **1993**, *140*, 2836–2843.
18. Herino, R.; Bomchil, G.; Barla, K.; Bertrand, C.; Ginoux, J. *J. Electrochem. Soc.* **1987**, *134*, 1994-2000.
19. Smith, R. L.; S. D. Collins. *J Appl. Physics*, **1992**, *71*, R1-R22.
20. Kolasinski, K. W.; *Surf. Sci.* **2009**, *603*, 1904-1911.

21. Santos, A.; Kumeria, T. *Electrochemically Engineered Nanoporous Materials*, **2015**, Springer, 1–36.
22. Yamamura, K.; Mitani, T. *Surf. Interface Anal.* **2008**, *40*, 1011–1013.
23. Melnichenko, M. M.; Svezhentsova, K. V.; Shmyryeva, A. N. *J. Mater. Sci.* **2005**, *40*, 1409–1412.
24. Chattopadhyay, S.; Li, X.; Bohn, P. W. *J. Appl. Phys.* **2002**, *91*, 6134–6140.
25. Lévy-Clément, C. *Handbook of Porous Silicon*, **2014**, Springer International Publishing, Switzerland, 49–66.
26. Huang, Z.; Geyer, N.; Werner, P.; De Boor, J.; Gösele, U. *Adv. Mater.*, **2011**, *23*, 285–308.
27. Geyer, N.; Fuhrmann, B.; Leipner, H. S.; Werner, P. *Appl. Mater Inter.* **2013**, *5*, 4302–4308.
28. Lee, C.L.; Tsujino, K.; Kanda, Y.; Ikeda, S.; Matsumura, M. *J. Mater. Chem.* **2008**, *18*, 1015–1020.
29. Sujino, K.; Matsumura, M. *Electrochem. Solid-State Lett.* **2005**, *8*, C193–C195.
30. Lee, C.L.; Tsujino, K.; Kanda, Y.; Ikeda, S.; Matsumura, M. *J. Mater. Chem.* **2008**, *18*, 1015–1020.
31. Gribov, B. G.; Zinov'ev, K. V. *Inorg. Mater.* **2003**, *39*, 653–662.
32. Favors, Z.; Wang, W.; Bay, H. H.; Mutlu, Z.; Ahmed, K.; Liu, C.; Ozkan, C. S. *Sci. Rep.* **2014**, *4*, 5623–5630.
33. Bao, Z.; Weatherspoon, M. R.; Shian, S.; Cai, Y.; Graham, P. D.; Allan, S. M.; Abernathy, H. W. *Nature*, **2007**, *446*, 172–175.
34. Canham, L. T. *Handbook of Porous Silicon*, **2014**, Springer International Publishing, Switzerland, 85–89.
35. Nohira, T.; Yasuda, K.; Ito, Y. *Nat. Mater.* **2003**, *2*, 397–401.
36. Yasuda, K.; Nohira, T.; Ogata, Y. H.; Ito, Y. *J. Electrochem. Soc.*, **2005**, *152*, D208–D212.
37. Banerjee, H. D.; Sen, S.; Acharya, H. N. *Mater. Sci. Eng.* **1982**, *52*, 173–179.
38. Bose, D. N.; Govindacharyulu, P. A.; Banerjee, H. D. *Sol. Energy Mater Sol. Cells*, **1982**, *7*, 319–321.



39. Wong, D. P.; Suriyaprabha, R.; Yuvakumar, R.; Rajendran, V.; Chen, Y. T.; Hwang, B. J.; Chen, K. H. *J. Mater. Chem., A*, **2014**, *2*, 13437–13441.
40. Yoo, J. K.; Kim, J.; Choi, M. J.; Park, Y. U.; Hong, J.; Baek, K. M.; Jung, Y. S. *Adv. Energy mater.* **2014**, *4*, 1-9.
41. Xie, J.; Wang, G.; Huo, Y.; Zhang, S.; Cao, G.; Zhao, X. *Electrochim. Acta.* **2014**, *135*, 94–100.
42. Bao, Z.; Ernst, E. M.; Yoo, S.; Sandhage, K. H. *Adv. Mater.* **2009**, *21*, 474–478.
43. Mojarad, B. S.; Nourbakhsh, A.; Kahrizsangi, R. E.; Masoud, M.; MacKenzie, K. *J. Ceram. Int.* **2015**, *41*, 5287–5293.
44. Khripin, C. Y.; Pristinski, D.; Dunphy, D. R.; Brinker, C. J.; Kaehr, B. *ACS Nano*, **2011**, *5*, 1401–1409.
45. Richman, E. K.; Kang, C. B.; Brezesinski, T.; Tolbert, S. H. *Nano Lett.* **2008**, *8*, 3075–3079.
46. Luo, W.; Wang, X.; Meyers, C.; Wannemacher, N.; Sirisaksoontorn, W.; Lerner, M. M.; Ji, X. *Sci. Rep.* **2013**, *3*, 2222.
47. Kim, K. H.; Lee, D. J.; Cho, K. M.; Kim, S. J.; Park, J. K.; Jung, H. T. *Sci. Rep.* **2015**, *5*, 9014.
48. Zalba, B.; Mariñ, J. M.; Cabeza, L. F.; Mehling, H. *Appl. Therm. Eng.* **2003**, *23*, 251–283.
49. Batchelor, L.; Loni, A.; Canham, L. T.; Hasan, M.; Coffey, J. L. *Silicon*, **2012**, *4*, 259–266.
50. Bok, T.; Choi, S.; Lee, J.; Park, S. *J. Mater. Chem.* **2014**, *2*, 14195-14200.
51. Guo, M.; Zou, X.; Ren, H.; Muhammad, F.; Huang, C.; Qiu, S.; Zhu, G. *Microporous Mesoporous Mater.* **2011**, *142*, 194–201.
52. Rossi, A. M.; Wang, L.; Reipa, V.; Murphy, T. E. *Biosens. Bioelectron.* **2007**, *23*, 741-745.
53. Coffey, J. L.; Whitehead, M. A.; Nagesha, D. K.; Mukherjee, P.; Akkaraju, G.; Totolici, M.; Saffie, R. S.; Canham, L. T. *Phys. Status Solidi A*, **2005**, *202*, 1451–1455.
54. Salonen, J.; Kaukonen, AM.; Hirvonen, J.; Lehto, V. P. *J. Pharm. Sci.* **2008**, *97*, 632–652.
55. Canham, L. T. *Adv. Mater.* **1995**, *7*, 1033–1037.

56. Anderson, S. H. C.; Elliot, H.; Wallis, D. J.; Canham, L. T.; Powell, J. J. *Phys. Status Solidi A*, **2003**, *197*, 331–335.
57. Reffitt, D. M.; Jugdaohsingh, R.; Thompson, R. P.; Powell, J. J. *J. Inorg. Biochem.* **1999**, *76*, 141–147.
58. Godin, B.; Gu, J.; Serda, R. E.; Bhavane, R.; Tasciotti, E.; Chiappini, C.; Liu, X.; Tanaka, T.; Decuzzi, P.; Ferrari, M. *J. Biomed. Mater. Res.* **2010**, *94*, 1236–1243.
59. Bowditch, A. P.; Waters, K.; Gale, H.; Rice, D.; Scott, E. A. M.; Canham, L. T.; Reeves, C. L.; Loni, A.; Cox, T. I. *Mater. Res. Soc. Symp. Proc.* **1999**, *536*, 149–154.
60. Park, J. H.; Gu, L.; Maltzahn, G. V.; Ruoslahti, E.; Bhatia, S. N.; Sailor, M. J. *Nat. Mater.* **2009**, *8*, 331–336.
61. Tasciotti, E.; Liu, X.; Bhavane, R.; Plant, D.; Leonard, A. D.; Price, B. K.; Cheng, M. M.; Decuzzi, P.; Tour, J. M.; Robertson, F.; Ferrari, M. *Nat. Nanotech.* **2008**, *3*, 151–157.
62. Liu, D.; Bimbo, L. M.; Makila, E.; Villanova, F.; Kaasalainen, M.; Blanco, B. H.; Caramella, C. M.; Lehto, V. P.; Salonen, J.; Herzig, K. H.; Hirvonen, J.; Santos, H. A. *J. Control. Release.* **2013**, *170*, 268–278.
63. Nieto, A.; Hou, H.; Moon, S. W.; Sailor, M. J.; Freeman, W. R.; Cheng, L. *Invest. Ophthalmol. Vis.* **2015**, *56*, 1070–1080.
64. Chan, S.; Horner, S. R.; Fauchet, P. M.; Miller, B. L. *J. Am. Chem. Soc.* **2001**, *123*, 11797–11798.
65. Tzur-Balter, A.; Gilert, A.; Massad-Ivanir, N.; Segal, E. *Acta biomaterialia*, **2013**, *9*(4), 6208–6217.
66. Shrestha, N.; Shahbazi, M. A.; Araujo, F.; Makila, E.; Raula, J.; Kauppinen, E. I.; Salonen, J.; Sarmiento, B.; Hirvonen, J.; Santos, H. A. *Biomaterials*, **2015**, *68*, 9–20.
67. Prestidge, C. A.; Barnes, T. J.; Mierczynska-Vasilev, A.; Kempson, I.; Peddie, F.; Barnett, C. *Physica status solidi A*, **2008**, *205*, 311–315.
68. Wu, E. C.; Andrew, J. S.; Buyanin, A.; Kinsella, J. M.; Sailor, M. *J. Chem. Commun.* **2011**, *47*, 5699–5701.
69. Laaksonen, T.; Santos, H.; Vihola, H.; Salonen, J.; Riikonen, J.; Heikkila, T.; Peltonen, L.; Kumar, N.; Murzin, D. Y.; Lehto, V.P.; Hirvonen, J. *Chem. Res. Toxicol.* **2007**, *20*, 1913–1918.

70. Sailor, M. J. Handbook of Porous silicon. **2014**. Springer International Publishing, 355–380.
71. Dancil, K. P. S.; Greiner, D. P.; Sailor, M. J. *J. Am. Chem. Soc.* **1999**, *121*, 7925–7930.
72. Lehto, V. P.; Riikonen, J. *Porous Silicon for Biomedical Applications*. **2014**, *14*, 337–355.
73. Sailor, M. J. Porous Silicon in Practice: Preparation, Characterization and Applications, **2012**, Wiley-VCH Verlag GmbH & Co. K A, 1–42.
74. Karlsson, L. M.; Schubert, M.; Ashkenov, N.; Arwin, H. *Thin Solid Films*, **2004**, *455*, 726–730.
75. Hou, H.; Nieto, A.; Ma, F.; Freeman, W. R.; Sailor, M. J.; Cheng, L. *J. Control. Release*, **2014**, *178*, 46–54.
76. Fry, N. L.; Boss, G. R.; Sailor, M. J. *Chem. Mater.* **2014**, *26*, 2758–2764.
77. Linnell, T.; Riikonen, J.; Salonen, J.; Kaukonen, A. M.; Laitinen, L.; Hirvonen, J. *Int. J. Pharm.* **2007**, *343*, 141–147.
78. Canham, L. T. Handbook of Porous Silicon, **2014**, Springer International Publishing, Switzerland, 908–918.
79. Salonen, J.; Laitinen, L.; Lailpmem. A. M.; Tuura, J.; Bjorkqvist, M.; Heikkila, K.; Heikkila, K. V.; Hirvonen, J.; Lehto, V. P. *J. Control. Release*, **2005**, *108*, 362-374.
80. Canham, L. Handbook of Porous Silicon, **2014**, Springer International Publishing, Switzerland, 163–170.
81. Xin, L.; John, J.; Coffey, J. L.; Chen, Y.; Pinizzatto, R. F.; Newey, J.; Reeves, C.; Canham, L. T. *Biomed. Microdev.* **2000**, *2*, 265-272.
82. Vaccari, L.; Canton, D.; Zaffaroni, N.; Villa, R.; Tormen, M.; Fabrizio, E. D. *Microelectron. Eng.* **2006**, *83*, 1598–1601.
83. Gu, L.; Park, J. H.; Dong, K. H.; Ruoslahti, E.; Sailor, M. J. *Small*, **2010**, *6*, 2546–2552.
84. Secret, E.; Smith, K.; Dubljevic, V.; Moore, E.; Macardle, P.; Delalat, B.; Voelcker, N. H. *Adv. Healthc. Mater.* **2013**, *2*, 718-727.
85. Perelman, L. A.; Pacholski, C.; Li, Y. Y.; VanNieuwenhze, M. S.; Sailor, M. J. *Nanomed.* **2008**, *3*, 31–43.
86. Pal, S.; Ramu, V.; Taye, N.; Mogare, D. G.; Yeware, A. M.; Sarkar, D.; Das, A. *Bioconj. Chem.* **2016**, *27*, 2062-2070.

87. Wang, M.; Coffey, J. L.; Dorraj, K.; Hartman, P.S.; Loni, A.; Canham, L. T. *Mol. Pharm.* **2010**, *7*, 2232–2239.
88. Tang, L.; Saharay, A.; Fleischer, W.; Hartman, P. S.; Loni, A.; Canham, L. T.; Coffey, J. L. *Silicon*. **2013**, *5*, 213–217.
89. Skalak, M.; Bertucci, A.; Braun, G.; Ricci, F.; Ruoslahti, E.; Sailor, M. J.; Bhatia, S. N. *Adv. Mater.* **2017**, *29*, 1701527.
90. Dancil, K. S.; Greiner, D. P.; Sailor, M. J. *J. Am. Chem. Soc.* **1999**, *121*, 7925–7930.
91. Lin, V.; Motesharei, K.; Dancil, K. S.; Sailor, M. J.; Ghadiri, M. R. *Science*, **1997**, *278*, 840–843.
92. Lugo, J. E.; Ocampo, M.; Kirk, A. G.; Plant, D. V.; & Fauchet, P. M. *J. New Mater. Electrocheml Sys.* **2007**, *10*, 113.
93. Ivanir, N. M.; Shtenberg, G.; Raj, N.; Gazenbeek, C.; Budding, D.; Bos, M. P.; Segal, E. *Sci. Rep.* **2016**, *6*, 38099.
94. Nan, K.; Ma, F.; Hou, H.; Freeman, W. R.; Sailor, M. J.; Cheng, L. *Acta Biomater.* **2014**, *10*, 3505–3512.
95. Hajj-Hassan, M.; Khayyat-Kholghi, M.; Wang, H.; Chodavarapu, V.; Henderson, J. E. *J. Biomed. Mater. Res. A*, **2011**, *99*, 269–274.
96. Marra, K. G.; Szem, J. W.; Kumta, P. N.; DiMilla, P. A.; Weiss, L. E.; *J. Biomed. Mater. Res. B*, **1999**, *47*, 324–335.
97. Whitehead, M. A.; Fan, D.; Mukherjee, P.; Akkaraju, G. R.; Canham, L. T.; Coffey, J. L. *Tissue Eng. Part A*, **2008**, *14*, 195–206.
98. Reffitt, D. M.; Ogston, N.; Jugdaohsingh, R.; Cheung, H. F.; Evans, B. A.; Thompson, R. P.; Powell, J. J.; Hampson, G. N. *Bone*, **2003**, *32*, 127–135.
99. Sun, W.; Puzas, J. E.; Sheu, T. J.; Fauchet, P. M. *Physica Status Solidi A*, **2007**, *204*, 1429–1433.
100. Coffey, J. L.; Whitehead, M. A.; Nagesha, D. K.; Mukherjee, P.; Akkaraju, G.; Totolici, M.; Saffie, R. S.; Canham, L. T. *Phys. Status Solidi A*, **2005**, *202*, 1451–1455.
101. Datnoff, L. E.; Synder, C. H.; Korndorfer, G. H.; *Silicon in agriculture*, **2001**, Elsevier Science, 1–20.
102. Epstein, E. *Ann Appl. Biol.* **2009**, *155*, 155–160.

103. Janek, K.; Chi-Feng, C.; Jesus, S.; Jose, M. R.; Alan, L. M. *Philos. Mag A*. **1998**, *77*, 201–216.
104. Yamanaka *et al.* *J. Appl. Phys.* **2012**, *111*, 044703–044706.
105. Coradin, T.; Eglin, D.; Livage. *J. Spectroscopy*, **2004**, *18*, 567–576.
106. Law, C.; Exley, C. *BMC Plant Biol.* **2011**, *11*, 1–9.
107. Zhang, X. Y.; Zhang, L. D.; Meng, G. W.; Li, G. H.; Jin-Phillipp, N. Y.; Phillipp, F. *Adv. Mater.* **2001**, *13*, 1238–1241.
108. Yang, M.; Huang, D.; Hao, P.; Zhang, F.; Hou, X.; Wang, X. *J. Appl. Phys.* **1994**, *75*, 651–653.
109. Shabir, Q. *Handbook of Porous Silicon*, **2014**, Springer International Publishing, 395–401.
110. Shabir, Q.; Pokale, A.; Loni, A.; Johnson, D. R.; Canham, L. T.; Fenollosa, R.; Tymczenco, M.; Rodriguez, I.; Meseguer, F.; Cros, A.; Cantarero, A. *Silicon* **2011**, *3*, 173–176.
111. Hon, N. K.; Shaposhnik, Z.; Diebold, E. D.; Tamanoi, F.; Jalali, B. *J. Biomed. Mater. Res. A*. **2012**, *100*, 3416–3421.
112. Cheng, L.; Anglin, E.; Cunin, F.; Kim, D.; Sailor, M. J.; Falkenstein, I.; Tammewar, A.; Freeman, W. R. *J. Ophthalmol.* **2008**, *92*, 705–711.
113. McInnes, S. J.; Irani, Y.; Williams, K. A.; Voelcker, N. H. *Nanomedicine*, **2012**, *7*, 995–1016.
114. Lehmann, V. *Phys. Status Solidi A*, **2007**, *204*, 1318–1320.
115. Riikonen, J.; Salomäki, M.; Wonderen, J.; Kemell, M.; Xu, W.; Korhonen, O.; Ritala, M.; MacMillan, F.; Salonen, J.; Lehto, V.P. *Langmuir*, **2012**, *28*, 10573–10583.
116. Jaimik, R. D.; Nimish, P. L.; Patel R.; Jivani. N.P.; Bhatt, N. M. *J. App. Pharm. Sci.* **2011**, *01*, 27–31.
117. Zubair, M.; Bibi, Z.; Rizwan, K.; Rasool, N.; Zahoor, F. A.; Riaz, M. *J. app. Pharm. Sci.* **2013**, *01*, 50–58.
118. Radulovic, N.; Stojanovic, G.; Palic, R. *Phytother. Res.* **2006**, *20*, 85–88.
119. Radojevic, I D.; Stankovic, M. S.; Stefanovic, O. D.; Topuzovic, M. D.; Comic, L. R.; Ostojic, A. M. *EXCLI J.* **2012**, *11*, 59–67.
120. Sandhu, N. S.; Kaur, S.; Chopra, D. *Asian J.Pharm. Clin. Res.* **2010**, *3*, 146-150.

121. Wasnik, D. D.; Tumane, P. M. *Int. J. Pharm. Sci. Rev. Res.* **2014**, *25*, 215–218.
122. Ma, J. K.; Chikwamba, R.; Sparrow, P.; Fischer, R.; Mahoney, R.; Twyman, R. *M. Trends in Plant Sci.* **2005**, *10*, 1360–1385.
123. Stermitz, F. R.; Lorenz, P.; Tawara, J. N.; Zenewicz, L. A.; Lewis, K. *Proc. Natl. Acad. Sci.* **2000**, *97*, 1433–1437.
124. Ragasa, C. Y.; Philip, Chua, A. P. U.; Shen, C. *J. Chem. Pharm. Res.* **2014**, *6*, 738–742.
125. Kamboj, A.; Saluja, A. K.; *Int. J. Pharm. Pharm. Sci.* **2011**, *3*, 94–96.
126. Nishina, A.; Hasegawa, K.; Uchibori, T.; Seino, H.; Osawa, T. *J. Agric. Food Chem.* **1991**, *39*, 266–269.
127. Yinusa, I.; George, N. I.; Shuaibu, U. O. A.; Ayo, R. G. *Int. J. Curr. Microbiol. Appl. Sci.* **2014**, *3*, 475–479.
128. Kim, M. H.; Jo, S. H.; Ha, K. S.; Song, J. H.; Jang, H. D.; Kwon, Y. I. *J. Microbiol. Biotechnol.* **2010**, *20*, 1204–1209.
129. Choi, E. J.; Ka, E. H.; Jo, C. Y.; Jo, S. H.; Apostolidis, E.; Lee, M. S.; Jang, H. D.; Kwon, Y. I. *Food Sci. Biotechnol.* **2014**, *23*, 791–797.
130. Moshi, M.; Joseph, C.; Innocent, E.; Nkunya, M. *Pharm. Biol.* **2004**, *42*, 269–273.
131. Adnan, S. A.; Ibrahim, N.; Wan, Yaacob, W. A. *J. Glob. Antimicrob. Resist.* **2017**, *8*, 48–54.
132. Horspool, H. R.; Lipinski, C. A. *Drug Deliv. Technol.* **2003**, *3*, 34–46.
133. Gardner, C. R.; Walsh, C. T.; Almarsson, O. *Nat. Rev. Drug Discov.* **2004**, *3*, 926–934.
134. Lipinski, C. A.; *Am. Pharm. Rev.* **2002**, *5*, 82–85.
135. Lipinski, C. A.; Lombardo, F.; Dominy, B. W.; Feeney, P. J. *Adv. Drug Deliv. Rev.* **1997**, *23*, 3–25.
136. Veber, D. F.; Johnson, S. R.; Cheng, H. Y.; Smith, B. R.; Ward, K. W.; Kopple, K. *D. J. Med. Chem.* **2002**, *45*, 2615–2623.
137. Ezhilarasi, P. N.; P. Karthik, P. N.; Chhanwal, C.; Anandharama, C. *Food and Bioprocess Technol.* **2013**, *6*, 628–647.
138. Salonen, J.; Paski, J.; Vähä-Heikkilä, K.; Heikkilä, T.; Björkqvist, M.; Lehto, V. *P. Physica Status Solidi A*, **2005**, *202*, 1629–1633.

139. Makila, E.; Ferreira, M. P.; Kivela, H.; Niemi, S. M.; Correia, A.; Shahbazi, M. A.; Salonen, J. *Langmuir*, **2014**, *30*, 2196–2205.
140. Haidary, S. M.; Corcoles, E. P.; Ali, N. K. *Int. J. Electrochem. Sci.* **2013**, *8*, 9956–66.
141. Canham, L. *Handbook of Porous Silicon*, **2014**, Springer International Publishing, 985–997.
142. Lehto, V. P.; Riikonen, J. *Porous Silicon for Biomedical Applications*, **2014**, 337–355.
143. Loni, A. *Handbook of Porous Silicon*, **2014**, Springer International Publishing, 623–628.
144. Ballard, J. M.; Zhu, L.; Nelson, E. D.; Seburg, R. A. *J. Pharm. Biomed. Anal.*, **2007**, *43*, 142–150.
145. Temova, Ž.; Roškar, R. *J. Chrom. Sci.* **2016**, *54*, 1180–1186.
146. Makila, E.; Ferreira, M. P.; Kivela, H.; Niemi, S. M.; Correia, A.; Shahbazi, M. A.; Salonen, J. *Langmuir*, **2014**, *30*, 2196–2205.
147. Riikonen, J.; Mäkilä, E.; Salonen, J.; Lehto, V. P. *Langmuir*, **2009**, *25*, 6137–6142.
148. Lehto, V. P.; Vähä-Heikkilä, K.; Paski, J.; Salonen, J. *J. Thermal Anal. Calor.* **2005**, *80*, 393–397.
149. Scott, D. L.; Berry, H.; Capell, H.; Coppock, J.; Daymond, T.; Doyle, D. V.; Jawad, A. *Rheumatology*, **2000**, *39*, 1095–1101.
150. Emami-Shahri, N.; Hagemann, T. *Rheumatology*, **2011**, *51*, 413–422.
151. Karunaweera, N.; Raju, R.; Gyengesi, E.; Münch, G. *Front. Mol. Neurosci.* **2015**, *8*, 24.
152. Endale, M.; Park, S. C.; Kim, S.; Kim, S. H.; Yang, Y.; Cho, J. Y.; Rhee, M. H. *Immunobiology*, **2013**, *218*, 1452–1467.
153. Jobin, C.; Bradham, C. A.; Russo, M. P.; Juma, B.; Narula, A. S.; Brenner, D. A.; Sartor, R. *B. J. Immunol.* **1999**, *163*, 3474–3483.
154. Kim, J.; Lee, H. J.; Lee, K. W. *J. Neurochem.* **2010**, *112*, 1415–1430.
155. Shehzad, A.; Lee, J.; Huh, T. L.; Lee, Y. S. *Mol. Cell*, **2013**, *35*, 526–532.
156. Lv, L.; Liu, C.; Chen, C.; Yu, X.; Chen, G.; Shi, Y.; Li, G. *Oncotarget*, **2016**, *7*, 32184.
157. Anand, P.; Kunnumakkara, A. B.; Newman, R. A.; Agarwal, B. B. *Mol. Pharm.* **2007**, *4*, 807–818.
158. Shen, L.; Liu, C. C.; Anne, C. Y.; Ji, H. F. *Sci. Rep.* **2016**, *6*, 20872.
159. Shutava, T. G.; Balkundi, S. S.; Vangala, P.; Steffan, J. J.; Bigelow, R. L.; Cardelli, J. A.; Lvov, Y. M. *ACS Nano*, **2009**, *3*, 1877–1885.
160. Baker, S. J.; Reddy, E. P. *Oncogene*, **1998**, *17*, 3261.

161. Buddhini, S. *Scientific American*, **2014**, The hallmarks cancer 8: Tumor promoting inflammation, Apr 18.
162. Kedare, S. B.; Singh, R. P. *J. Food Sci. Technol.* **2011**, *48*, 412–422.
163. Gründemann, C.; Lengen, K.; Sauer, B.; Garcia-Käufer, M.; Zehl, M.; Huber, R. *BMC Complement. Altern. Med.* **2014**, *14*, 283.
164. Kaur, H.; Kaur, G. *J. Pharm.* **2014**, *2014*, 180845.
165. Stone, D. *Viruses*, **2010**, *2*, 1002–1007.
166. Hardee, C. L.; Arévalo-Soliz, L. M.; Hornstein, B. D.; Zechiedrich, L. *Genes*, **2017**, *8*, 1–22.
167. Loo, J. C. V. D.; Wright, J. F. *Hum. Mol. Genet.* **2016**, *25*, R42–R52.
168. Thomas, C. E.; Ehrhardt, A.; Kay, M. A. *Nat. Rev. Genet.* **2003**, *4*, 346–358.
169. Ramamoorth, M.; Narvekar, A. *J. Cardiovasc. Dis. Res.* **2015**, *9*, GE01–GE06.
170. FDA. (2017, April 30). *FDA approval brings first gene therapy to the United States* (Press release). Retrieved April 03, 2018.
171. Thomas, C. E.; Ehrhardt, A.; Kay, M. A. *Nat. Rev. Genet.*, **2003**, *4*, 346.
172. Ramamoorth, M.; Narvekar, A. *J. Clin. Diagn. Res.* **2015**, *9*, GE01.
173. Yin, H.; Kanasty, R. L.; Eltoukhy, A. A.; Vegas, A. J.; Dorkin, J. R.; Anderson, D. G. *Nat. Rev. Genet.*, **2014**, *15*, 541.
174. Medina-Kauwe, L. K.; Xie, J.; Hamm-Alvarez, S. *Gene Therapy*, **2005**, *12*, 1734–1751.
175. Wong, S. Y.; Pelet, J. M.; Putnam, D. *Prog. Polym. Sci.* **2007**, *32*, 799–837.
176. Zelphati, O.; Szoka, F. C. *Proc. Natl. Acad. Sci.* **1996**, *93*, 11493–11498.
177. Behr, J. P. *Chimia*. **1997**, *51*, 34–36.
178. Liang, W.; Lam, J. K. *Molecular Regulation of Endocytosis*. **2012**, InTech.
179. Zabner, J.; Fasbender, A. J.; Moninger, T.; Poellinger, K. A.; Welsh, M. J. *J. Bio. Chem.* **1995**, *270*, 18997–19007.
180. Pollard, H. C. A. C. A.; Remy, J.-S.; Loussouarn, G.; Demolombe, S.; Behr, J.-P.; Escande, D. *J. Bio. Chem.* **1998**, *273*, 7507–7511.
181. Bai, H.; Lester, G. M. S.; Petishnok, L. C.; Dean, D. A. *Sci. Rep.* **2017**, *37*,
182. Lv, H.; Zhang, S.; Wang, B.; Cui, S.; Yan, J. *J. Control. Release*, **2006**, *114*, 100–109.
183. Kim, W.; Ng, J. K.; Kunitake, M. E.; Conklin, B. R.; Yang, P. *J. Am. Chem. Soc.* **2007**, *129*, 7228–7229.



184. Shen, J.; Xu, R.; Mai, J.; Kim, H.-C.; Guo, X.; Qin, G.; Yang, Y.; Wolfram, J.; Mu, C.; Xia, X.; Gu, J.; Liu, X.; Mao, Z.-W.; Ferrari, M.; Shen, H. *ACS Nano*, **2013**, *7*, 9867–9880.
185. Wareing, N.; Szymanski, K.; Akkaraju, G. R.; Loni, A.; Canham, L. T. Gonzalez-Rodriguez, R.; Coffey, J. L. *Small*, **2017**, *13*, 1-5.
186. Y. Tian. Ph.D. Dissertation. Texas Christian University, **2006**.
187. Kim, D.S.; Matsuda, T.; Cepko, C.L. *J. Neurosci.* **2008**, *28*, 7748-7764.
188. Zhang, M.; Xu, R.; Xia, X.; Yang, Y.; Gu, J.; Qin, G.; Liu, X.; Ferrari, M.; Shen, H. *Biomaterials*, **2014**, *35*, 423–431.

# Vita

## PERSONAL INFORMATION

Jhansi Rani Kalluri

Garbham, Andhra Pradesh, India

Daughter of Satyanarayana Kalluri and Vijayalaxmi Sappa

Wife of Manikyala Rao Chintapalli

## EDUCATION

Ph.D. Chemistry, 2018

Texas Christian University

Dissertation title: “*Sustainable routes to porous silicon nanostructures as drug and gene delivery vehicles.*”

M.S. Chemistry, 2009

Jackson State University

Thesis title: “*Dynamic light scattering assay for selective detection of Arsenic from ground water using gold nanoparticles.*”

B. Pharmacy, 2006

Andhra University, Visakhapatnam, India

## EXPERIENCE

Junior Analytical Chemist, Vivi Med. labs, Hyderabad, India, 2006-2007

Teaching Assistant, Jackson State University, Jackson, MS, 2007-2009

Graduate Research Assistant, Texas Christian University, Fort Worth, TX, 2012-2018

## Abstract

### Sustainable Routes to Porous Silicon Nanostructures as Drug and Gene Delivery Vehicles

Jhansi Rani Kalluri

Department of Chemistry & Biochemistry

Advisor: Dr. Jeffery L. Coffey

Porous silicon (pSi), with its nanoscale architecture, acts as a promising resorbable biomaterial for a broad variety of applications: biosensors, orthopedic tissue engineering, and controlled drug delivery. The most conventional methods for preparing porous silicon particles are anodization of silicon wafers and metal-assisted chemical etching (MACE). These established techniques require elemental crystalline silicon feedstocks, and the use of corrosive hydrofluoric acid (HF) and organic solvents.

Rather than employing these methods, we have developed an eco-friendly alternative of producing pSi from silicon accumulator plants/agriculture waste. Two different silicon accumulator plants *Bambuseae* (tabasheer) and *Equisetum telmateia* (great horsetail) have been investigated for this purpose, and high surface area porous silicon nanostructures prepared using a magnesiothermic reduction of silica isolated from these plants. This fabrication process of pSi includes extraction of biogenic silica from the ground plant by calcination, followed by reduction with magnesium, and purification of reduced Si product. Details of fabrication process and characterization of pSi powders by a combination of scanning electron microscopy (SEM), energy dispersive X-ray analysis (EDX), X-ray diffraction (XRD), transmission electron microscopy (TEM), and low temperature nitrogen gas adsorption measurements will be outlined in this presentation.

As pointed out above, *Bambuseae* serves as a viable eco-friendly starting materials for fabricating porous silicon (pSi). At the same time, if the selected plant leaf components contain medicinally-active species (antibacterial) as well, then the single substance can provide not only the nanoscale high surface area drug delivery carrier, but the drug itself. With this idea in mind using a single plant source (*Bambuseae*) we have developed porous silicon based drug delivery carrier matrix for the sustained release of antibacterials.

Nanoentrapment of vitamins, nutrients, and plant based therapeutics is another attractive area in food and pharmaceutical industries to address the challenges of stability and bioavailability of entrapped agents. One way to increase the bioavailability of the drugs is by enhancing their solubility. We have evaluated the ability of nanostructured plant-derived porous silicon particles (pSi) as potential candidates to increase the solubility of plant extracts rich in therapeutic polyphenolic compounds (*Equisetum arvense*) and a poorly water soluble vitamin (vitamin d3).

We have also evaluated the ability of plant derived porous silicon nanoparticles (pSiNPs) as gene delivery vehicles. Following necessary reduction of pSiNP particle size and functionalization with primary amine moieties at the nanoparticle surface, the binding of a reporter plasmid DNA, pEF1-eGFP (endothelial factor 1 enhanced green fluorescent protein, 6429 bp) to the pSiNPs was investigated, followed by attempted transfection of HEK293 cells.